

Modeling and Active Damping of Structural Vibrations in Machine Tools

by

Amir Hossein Hadi Hosseinabadi

B.Sc., Sharif University of Technology, Iran, 2011

A THESIS SUBMITTED IN PARTIAL FULFILLMENT OF
THE REQUIREMENTS FOR THE DEGREE OF
MASTER OF SCIENCE

in

The Faculty of Graduate and Postdoctoral Studies

(Mechanical Engineering)

THE UNIVERSITY OF BRITISH COLUMBIA

(Vancouver)

November 2013

© Amir Hossein Hadi Hosseinabadi 2013

Abstract

Feed drives of High Speed Machine (HSM) tools deliver fast motions for rapid positioning of tool or workpiece. The inertial forces generated by acceleration and deceleration of large machine tool components excite structural modes of the machine tools and cause residual vibrations. Unless avoided, the vibrations lead to poor surface finish and instability of the drive's control loop. In this thesis, structural flexibilities are represented by linear and torsional springs and dampers to develop a mathematical model of the feed drive dynamics. The model includes the contribution of structural vibrations in measuring table position by a linear encoder. An identification algorithm is introduced to facilitate the estimation of rigid body and structural dynamics in frequency domain. The identified mathematical model is used to mimic the real machine in simulations with the purpose of analyzing the interaction between structural dynamics and a high bandwidth adaptive sliding mode controller.

Meanwhile, efficiency of finite element modeling approaches in predicting this interaction prior to the physical production is investigated by replacing the machine dynamics by a FEM based model. The mathematical model is used to design a Kalman Filter which estimates the table's acceleration by taking double digital derivative of the encoder signal. The table's acceleration is used to modify the control loop to minimize the effect of undesired structural vibrations. It is shown that the vibrations can be actively damped, and the bandwidth of the drive can be increased. The increase in the servo loop bandwidth provides smoother motion and improves the tracking performance significantly.

Preface

This dissertation is original intellectual property of the author, Amir Hossein Hadi Hosseini, under supervision of professor Yusuf Altintas. This work has been completed in the Manufacturing Automation Laboratory at the University of British Columbia. The results presented in Chapters 3 to 5 are going to be submitted for publications. All figures and tables found in this thesis are used with permission from applicable sources.

Table of Contents

Abstract	ii
Preface	iii
Table of Contents	iv
List of Tables	vii
List of Figures	viii
Acknowledgments	xix
Dedication	xx
1 Introduction	1
2 Literature Review	5
2.1 Overview	5
2.2 Modeling the Dynamics of Flexible Machine Tools	5
2.3 Identification of Machine Tool Dynamics	9
2.4 Vibration Reduction in Production Machines	11
2.5 Summary	16
3 Mathematical Modeling of Structural Dynamics	17

Table of Contents

3.1	Overview	17
3.2	Machine Tool Feed Drives	17
3.3	Mathematical Modeling of Feed Drives	19
3.3.1	Rigid Body Model of the Ball-Screw Drive	20
3.3.2	Flexible Ball-Screw Model	22
3.3.3	Feed Drive In a Flexible Machine Tool	25
3.4	Summary	33
4	Experimental Identification of Feed Drive Dynamics	34
4.1	Overview	34
4.2	Identification of Rigid Body Dynamics ($G_r(s)$)	34
4.3	Identification of Structural Flexibilities	40
4.4	Modal Parameters (ζ, ω_n) Estimation	42
4.4.1	The Peak Picking Method	43
4.4.2	The Rational Fraction Polynomial (RFP) Method	45
4.5	Experimental Identification Results	49
4.5.1	Ball-Screw Test Bed	49
4.5.2	Flexible Machine Tool - FADAL VMC2216	59
4.6	Validation of the Identified Model for the Flexible Machine Tool	66
4.7	Structural Dynamics in Finite Element Models	69
4.8	Summary	72
5	Drive-Based Vibration Reduction	74
5.1	Overview	74
5.2	Structural Dynamics in Control Loop	74
5.3	Vibration Reduction with Acceleration Feedback	77
5.3.1	Cascade Control Structure	78

Table of Contents

5.3.2 Adaptive Sliding Mode Controller	81
5.4 Kalman Filter Design	85
5.5 Experimental Implementation	88
5.6 Summary	91
6 Conclusion and Future Work	92
Bibliography	95
 Appendices	
A ZOH Equivalent of The T.F in Equation 4.6	103
B Orthogonal Polynomials	106
B.1 Construction of Orthogonal Polynomials	106
B.2 Proof of Equation 4.51	107

List of Tables

4.1	Identified parameters of the flexible ball-screw drive	55
4.2	Identified parameters of structural transfer function of the feed drive ($G_f(s)$ [m/m], see Equation (4.69)).	64
4.3	Identified parameters of $G'_f(s)$ [$m/N.m$](see Equation (4.75)).	72
5.1	Comparison of damping ratios before and after active damping	84

List of Figures

1.1	Frequency content of trajectory generation algorithms with infinite, constant and continuous jerk profiles.	3
2.1	Hybrid model of machine tool [1].	8
2.2	Comparison of modeling strategies	9
2.3	Electromagnetic active damper	13
2.4	Vibration reduction approaches in production machines	16
3.1	Ball-screw feed drive	18
3.2	Linear drive	18
3.3	Schematic diagram of a C-frame milling machine	20
3.4	Rigid ball-screw mounted on a rigid bed	20
3.5	Ball-screw feed drive - UBC Mechatronics Laboratory	22
3.6	Flexible ball-screw mounted on a rigid bed	23
3.7	FADAL VMC2216 three axis machining center	26
3.8	Flexible ball-screw model	27
3.9	Bending mode of flexible machine tool structure	28
3.10	Bending mode of flexible machine tool structure	29
4.1	Least square identification reference command	39
4.2	Identification of G_f Flowchart	43

List of Figures

4.3	Single degree of freedom oscillator (Mass, Spring, and Damper System)	43
4.4	Transfer function of a SDOF system represented by its real and imaginary parts	44
4.5	Magnitude plot of frequency response function for a system with two closely spaced modes	46
4.6	Estimated inertia (J_e) and viscous damping coefficient (B_e) by unbiased least squares technique	50
4.7	The experimental FRF between motor torque and table displacement measured by linear and rotary encoders	51
4.8	Contribution of the ball-screw torsional flexibility in the experimental FRFs measured by linear and rotary encoders	52
4.9	Real and imaginary plots of the experimental FRF for G_{ft} and G_{fm}	53
4.10	Magnitude and phase plot of experimental and reconstructed $\frac{G_{ft}(j\omega)}{G_{fm}(j\omega)}$	54
4.11	Experimental and reconstructed FRF of the transfer function between motor torque (T_m) and table position capture by linear encoder (x_t) (see Equation (4.63))	55
4.12	Experimental and reconstructed FRF of the transfer function between motor torque (T_m) and table position capture by rotary encoder ($r_g \theta_m$) (see Equation (4.64))	56
4.13	Direct FRFs measured at ball-screw table	57
4.14	The hammers used for direct FRF measurements at ball-screw table	58
4.15	Experimental FRFs of the feed drive in x direction for FADAL VMC2216 . . .	60
4.16	Comparison of the experimental FRF between table acceleration and input voltage to the amplifier measured by linear encoder (red line) and accelerometer (blue line)	61
4.17	Experimental acceleration FRF - Comparison of using two accelerometers (blue line) and linear encoder (red line)	62

List of Figures

4.18	Estimation of modal parameter with RFP method for the closely spaced column bending and torsion modes.	63
4.19	Experimental FRF of the feed drive structure ($G_f(s)$, see Equation (4.69)). . . .	65
4.20	Experimental and reconstructed FRF of the open loop transfer function ($G_e(s)$, see Equation (4.69)).	65
4.21	The control loop block diagram	67
4.22	Reference trajectory with trapezoidal velocity profile	68
4.23	Comparison of simulated and experimental machine acceleration	68
4.24	Finite Element model of the column bending mode for the machine tool with structural flexibility	70
4.25	Comparison of Fitted and Simulated FRF of structural dynamics obtained from FEM ($G'_f(s)$, see Equation 4.75)	71
5.1	Reference trajectory with cubic acceleration profile	75
5.2	Comparison of simulation and experimental results for the ball screw drive controlled by a high bandwidth sliding mode controller without active damping.	76
5.3	The simulated table acceleration based on the FE model - high bandwidth sliding mode controller without active damping.	77
5.4	A single degree of freedom oscillator mounted on the ball-screw table.	78
5.5	Cascade control structure for the ball-screw drive	79
5.6	Velocity loop of ball screw drives with single degree of freedom oscillator and active damping	79
5.7	Velocity loop of ball screw drives with single degree of freedom oscillator and active damping - The indirect velocity loop is replaced by its DC gain (K_v)	80
5.8	Control loop for the linearized adaptive sliding mode controller	82

List of Figures

5.9	Velocity loop of the linearized adaptive sliding mode controller with active damping network included in the direct velocity loop	82
5.10	Bode plots of different velocity loops	83
5.11	Bode plots of the position loop with and without active damping	83
5.12	Block diagram of sliding mode controller with and without active damping of vibration mode with a natural frequency ω_n	89
5.13	Comparison of experimental results for the machine tool feed drive with and without active damping (AD)	90
5.14	Comparison of the control command (u) with and without active damping (AD)	90

Nomenclature

Roman Symbols

\dot{x}_T	Machine table velocity measured by the tachogenerator coupled to the motor shaft [mm/s]
\hat{d}	Disturbance compensator in the adaptive sliding mode controller [V]
\hat{y}	Output vector estimated by the Kalman Filter
\hat{z}	State vector observed by the Kalman Filter
\tilde{u}	Quantization error in the commanded voltage to the servo amplifier
\tilde{x}	Quantization error in the table position measured by the linear encoder
A_d	State (or system) matrix of the discrete time state space representation of the plant
B_d	Input matrix of the discrete time state space representation of the plant
B_e	Equivalent viscous damping coefficient reflected on motor shaft [kg.m ² /s]
B_t	Viscous damping coefficient between machine table and guide [kg/s]
C_d	Output matrix of the discrete time state space representation of the plant
c_t	Viscous damping coefficient of nut, bearing and coupling [kg.m ² /s]

Nomenclature

c_{cb}	Bending viscous damping coefficient of the machine column and bed clamping joint to the ground [kg.m ² /s]
c_{ct}	Torsional viscous damping coefficient of the machine column and bed clamping joint to the ground [kg.m ² /s]
c_{ls}	Axial viscous damping coefficient of the ball-screw [kg/s]
c_{ts}	Axial viscous damping coefficient of the ball-screw [kg.m ² /s]
D_d	Feed-through (or feed-forward) matrix of the discrete time state space representation of the plant
F_{cb}	The reaction force between machine column and the ground [N]
F_{mc}	The axial force between column and motor [N]
F_{tn}	The linear force between nut and machine table [N]
G_e	Transfer function between table displacement measured with linear encoder and applied torque at the ball-screw
G_f	Contribution of structural flexibilities in the transfer function between motor torque and table displacement measured by linear encoder
G_r	The Transfer function associated with the rigid body dynamics
G_t	Transfer function between motor torque and displacement of machine table
G_{be}	Transfer function between motor torque and vibration of the guidway on the bed at the point where encoder optical head is mounted.
h_p	Pitch length of the ball-screw [m]

Nomenclature

J_e	Equivalent inertia reflected on motor shaft [kg.m ²]
J_f	Jacobian matrix in Gauss-Newton curve fitting algorithm
J_m	Inertia of the nut, ball-screw coupling and motor shaft observed at the position [kg.m ²]
J_n	Inertia of the nut, ball-screw coupling and motor shaft observed at nut position [kg.m ²]
J_{cb}	Column, spindle and bed inertia in bending [Kg.m ²]
J_{ct}	Column, spindle and bed inertia in torsion [Kg.m ²]
k_a	Amplifier gain [A/V]
k_I	Gain of the integrator in the position controller loop of the linearized adaptive sliding mode controller [1/s ²]
k_p	Gain of the position feedback loop in the linearized adaptive sliding mode controller [1/s]
k_t	Motor torque constant [N.m/A]
k_u	Input voltage gain in rigid body identification [V/V]
K_v	DC gain of the indirect velocity loop [(mm/s)/(mm/s)]
k_v	Gain of the velocity controller in the linearized adaptive sliding mode controller [V/(mm/s)]
k_{cb}	Bending stiffness of the machine column and bed clamping joint to the ground [kg.m ² /s ²]

Nomenclature

k_{ct}	Torsional stiffness of the machine column and bed clamping joint to the ground [kg.m ² /s ²]
k_{ff}	Gain of the feed-forward inertia compensator in the linearized adaptive sliding mode controller [s]
k_{ls}	The axial stiffness of ball-screw [kg/s ²]
k_{ts}	Torsional stiffness of the ball-screw [kg.m ² /s ²]
L	Gain matrix in the Kalman Filter state estimator
M	Innovation gain matrix in the Kalman Filter output observer
m_c	Column, spindle and bed mass [kg]
m_m	Motor mass [Kg]
m_t	Table mass [Kg]
Q	Process noise matrix in Kalman filter design
R	Measurement noise matrix in Kalman filter design
r_g	Nut transformation ratio [m/rad]
s	Laplace variable
T_m	Motor torque applied to the ball-screw at motor shaft [N.m]
T_n	Load torque applied to the ball-screw at nut position [N.m]
T_s	Sampling period [sec]
T_{cb}	The reaction moment between machine column and the ground [N.m]

Nomenclature

T_{ct}	The reaction moment between machine column and the ground in column torsion [N.m]
x	Table position captured by linear encoder [m]
x_b	Displacement of the middle point of the guide on the bed [m]
x_c	Displacement of machine column COG [m]
x_m	Displacement of the motor [m]
x_n	Displacement of machine table due to axial deformation of ball-screw [m]
x_r	The reference position command for the machine table [mm]
x_t	Total Displacement of machine table where encoder scale is mounted [m]
x_{be}	Total displacement of bed at the point where encoder optical head is mounted [m]
Y	Measured velocity vector in identification of rigid body dynamics based on ULS technique
y	Output vector of the discrete time state space representation of the plant
z	State vector of the discrete time state space representation of the plant

Greek Symbols

β	Vector of unknowns in Gauss-Newton curve fitting algorithm
μ	Modal overlap factor
ν	Poisson's ratio
ω_{ni}	Natural Frequency of mode number i [rad/s]

Nomenclature

$\Phi(s)$	Transfer function matrix between motor torque and displacements at nut, motor, and the column
σ	Sliding surface of the adaptive sliding mode controller [mm/s]
θ_m	Angular displacement of ball-screw at motor shaft [rad]
θ_n	Angular displacement of ball-screw at nut [rad]
θ_{cb}	Column bending vibration [rad]
θ_{ct}	Column Torsion vibration [rad]
ζ_i	Damping ratio of mode number i

Acronyms

ADD	Active Damping Device
ARMAX	Auto-Regressive Moving Average with eXogenous input
ARX	Auto-Regressive models with eXogenous inputs
ASMC	Adaptive Sliding Mode Controller
CNC	Computer Numerical Control
FE	Finite Element
FEM	Finite Element Method
FFT	Fast Fourier Transform
FRF	Frequency Response Function
HiLS	Hardware in Loop Simulation

Nomenclature

HSM	High Speed Machining
LQG	Linear Quadratic Gaussian
OE	Output Error
PCE	Partial Continuous Estimation
PID	Proportional - Integrator - Derivative controller
RFP	Rational Fraction Polynomial
SDOF	Single Degree of Freedom
SUT	System Under Test
TDE	Total Discrete Estimation
ULS	Unbiased Least Squares
ZPETC	Zero Phase Error Tracking Controller

Acknowledgments

In the battle for success, everybody faces hard times, and no one can prosper without the help of an experienced and knowledgeable leader. In my way towards masters degree, professor Yusuf Altintas was not only a research supervisor but a passionate mentor whose personality has been a source of inspiration for the rest of my life.

I would like to present my sincere gratitude to my colleagues in Manufacturing Automation Laboratory who provided a friendly and constructive environment during the last two years and made this period unforgettable for me.

It was not possible to bear the hardships of living thousands of miles away from my family without the help of my supportive friends, especially my dear roommates Moein and Sina of whom I am deeply thankful.

Last but not least, I would like to express my sincere appreciation to my beloved parents and siblings for being a great source of support and encouragement to me and for their patience regarding my absence.

This research was sponsored by NSERC and Pratt & Whitney Canada as part of Industrial Research Chair in Virtual High Performance Machining

AMIR HOSSEIN HADI H.

The University of British Columbia

November 2013

THIS THESIS IS DEDICATED TO:

MY BELOVED PARENTS MOHAMMADREZA AND FATEMEH

AND MY DEAR SIBLINGS ALIREZA, AHMADREZA AND NEGIN

Chapter 1

Introduction

The growing demand for increased productivity has directed aerospace, automotive and die and mold industries towards machining technologies which provide the capability of manufacturing products in a rapid pace with high accuracy and good surface finish. Therefore, High Speed Machining (HSM) has received lots of attention from industrial sectors and provoked researchers to develop new techniques to reduce the cycle time while enhancing the quality of the final product.

Three or five axis computer numerical controlled (CNC) machines equipped with fast feed drives and powerful spindles are used to perform operations at cutting speeds up to 1000 [m/min]. Tangential feedrate along the desired trajectory is a function of spindle speed, number of cutting tool's flutes and feed per tooth; therefore, increase in the cutting speed requires higher feedrate to maintain an acceptable chip load. To achieve this, feed drives which can reach up to 1 [g] acceleration with feed speeds up to 40 [m/min] are utilized.

Accurate manufacturing of the parts with complex geometries, such as turbine blades, requires the cutting tool to travel along complicated paths in 3-D space. For this purpose, path planning algorithms must be implemented to decouple the desired tool-path into the position commands for each axis. Moreover, motion control strategies must be implemented to reduce tracking error between the instantaneous commanded and actual axis position. The discrepancy in tracking the reference command occurs because of the disturbance loads and limited bandwidth of servo drives. In multi-axis machining operations, tracking errors in different axis cause a geometrical deviation between the desired and the traversed tool-path, which is called

contouring error. If the contour error is large, the product tolerance will be violated. Moreover, machine tools exhibit structural flexibilities which cause tracking and contouring error profiles to possess low and high frequency components.

The low eigen-frequencies correspond to large components (i.e. column, tool changer and spindle housing), and are excited by the inertial forces generated through large accelerations and decelerations in high speed machine tools. The higher frequency modes originate from lighter components (i.e. tool and spindle) and are excited because of the metal cutting loads. As Figure 1.1 shows, discontinuities in the position, velocity, acceleration and jerk profiles commanded at discrete time intervals, introduce high frequency content to the inertial force and cause transient vibrations. These vibrations not only degrade the quality of final product but also damage the machine itself and reduce the productivity. If the inertial vibrations are felt by the control loop through encoder readings, the servo drive can become unstable and vibrate at the same frequency of structural modes. In general, there are three approaches to avoid the inertial vibrations.

The vibrations are notch filtered to prevent their transmission to control loop; therefore, the bandwidth of the drive servo is reduced. This classical approach reduces the high speed contouring ability of the machine, because the lowering of the bandwidth leads to increased axis tracking errors that are proportional to contouring feed speeds.

Alternatively, the position commands can be pre-shaped to avoid the excitation of natural modes of the machine. However, input shaping brings phase delay to axis commands which lead to severe distortion of the tool paths in multi-axis operations. Because this approach is an offline feed-forward technique, it cannot reduce the disturbance induced vibrations. Moreover, large variations of machine dynamics can degrade its performance.

It is more common to damp the natural vibrations through active damping network within the servo control loop. If the frequency of the vibration is beyond the bandwidth of the drive, external actuators dedicated to damping are added to the system. However, such measures

increase the complexity and the cost of the machine tool. It is more ideal to use the existing servo motor and sensors of the drive to actively damp the vibrations.

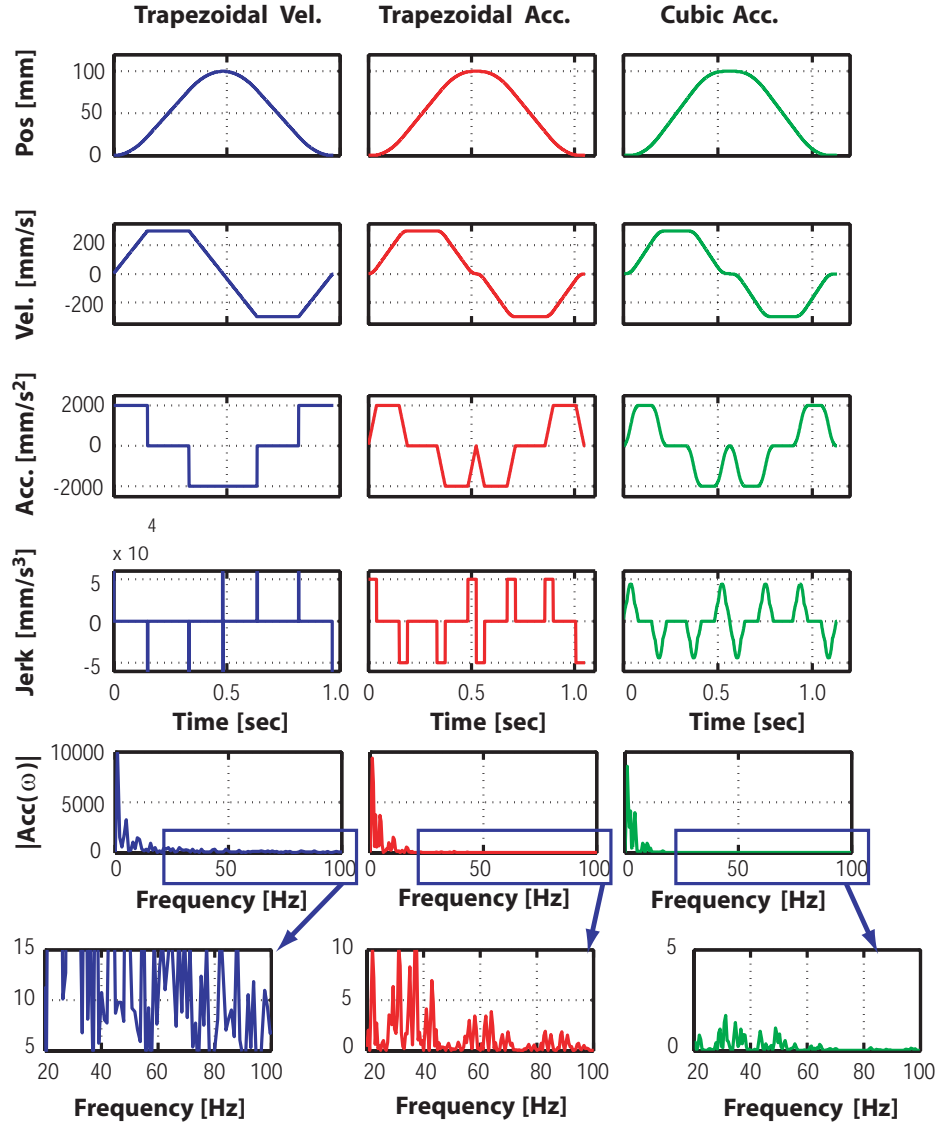


Figure 1.1: Frequency content of trajectory generation algorithms with infinite, constant and continuous jerk profiles.

This thesis presents modeling, identification and active damping of low frequency machine tool modes for CNC feed drives. Chapter 2 presents a brief overview of the existing literature on modeling, identification and vibration reduction in machine tools. The fundamental modes

of the machine tool column and ball screw drive are modeled, and the relative transfer function between the table and guide is developed analytically in Chapter 3. Chapter 4 is dedicated to identify the parameters of the transfer function from experimental excitation of servo motor and linear encoder output directly. It is shown that typically bending and torsional modes of the machine tool column structure, as well as the axial vibration mode of the ball screw interfere with the servo controller most. In Chapter 5, the experiments and simulations show that the controller becomes highly oscillatory with high vibration amplitudes unless they are damped. The proposed model is experimentally validated and the axial mode of the table drive is successfully damped with the acceleration feedback derived from linear encoder signals. If the machine tool is at the design stage, the same transfer function can be predicted using Finite Element model and tested in virtual environment for improved machine tool design. Chapter 6 contains the conclusion remarks and proposed future research directions.

Chapter 2

Literature Review

2.1 Overview

This chapter is dedicated to present an overview on state of the art in the field of modeling the structural vibrations in machine tools and summarizes the existing literature on different vibration reduction approaches. Therefore, it is structured as follows: Section 2.2 presents an overview on various modeling approaches to explain dynamics of flexible machine tools. Section 2.3 covers the existing literature on identification techniques to estimates the unknown parameters of the governing transfer function. An overview of existing literature on suppressing the oscillations in machine tools is presented in Section 2.4 and finally the chapter is summarized in Section 2.5.

2.2 Modeling the Dynamics of Flexible Machine Tools

Various modeling strategies exist to explain the dynamics of feed drives in machine tools. These schemes can be as simple as considering only the rigid body dynamics and neglecting all structural flexibilities, up to complex Finite Element (FE) models with up to millions of elements and a large number of degrees of freedom. Complex models provide higher accuracy at the expense of heavy computational load. Therefore, selection of the modeling technique is highly dependent on the modeling objective. For example, heavy computational loads of FEM makes them non-beneficial for controller design and simulation purposes. However, they are

quite efficient for topological optimization of machine tool structures.

The traditional approach for modeling the dynamics of feed drive systems is to develop *lumped rigid models* based on equivalent inertia (J_e) and viscous damping coefficient (B_e) reflected on motor shaft [2, 3, 4]. In this model the drive train is considered as a rigid combination of links, joints, and couplings which transfer the motion from motor shaft to table position, and all structural flexibilities are neglected. The simplest way of including structural flexibilities in modeling, is called *modular approach* in which the machine tool components are considered as point inertias connected with springs and dampers. Altintas et al. [5] modeled the ball-screw drive as a torsional spring connecting two rigid bodies and implemented the procedure presented by Dadalaue et al. [6] to obtain its torsional stiffness. Chen et al. [7] used springs to model the axial, torsional, and table-guideway stiffnesses of a ball-screw drive. They showed that in high acceleration motions, where large inertial forces are present, the compliance of the mechanical elements in a ball-screw drive system leads to significant vibrations and elastic deformations which degrade positioning accuracy of the table. Lee et al. [8] modeled the flexibilities of ball-screw drive and machine tool bed as linear springs and dampers. They proposed a procedure for tuning the parameters in a servo control system to avoid closed loop instability due to structural vibrations. A similar procedure for modeling machine tool flexibilities by assuming its components as lumped masses connected with linear or torsional springs and dampers is presented in [9, 10, 11].

Great amount of research has been dedicated to modeling machine tools by using Finite Element Methods (FEM). FEM is a powerful tool for modeling complex geometries and can handle problems with varying boundary conditions. Van Brussel et al. [12], Bianchi et al. [13] and Schafers et al. [14] developed full finite element models of machine tools. These models are capable of predicting machine tool behavior despite the change in boundary conditions due to different configuration of machine tool components. However, they have thousands of degrees of freedom leading to large matrices which impose high computational effort. Therefore,

in all cases, some model reduction algorithm is proposed to obtain a lower order model having less computational load and more suitable for control and simulation purposes.

Another approach for generating a mathematical model for an element (e.g. ball-screw) is to develop its distributed parameter representation. However, machine tool comprises numerous components; therefore, implementation of distributed parameter approach would become very difficult in practice because many partial differential equations need to be incorporated and different boundary conditions must be associated for each part. To solve this problem, researchers have resorted to *hybrid models*. In hybrid models some components (e.g. massive beams, bed plates, and foundation supports) are modeled as lumped point-wise mass, spring, and frictional assemblies, whereas distributed parameter formulation or finite element models are developed for components with large length/diameter and slenderness ratios which are more flexible, such as ball-screw drives [15].

Research efforts are mostly concentrated on modeling ball-screw dynamics. Whalley et al. [15] and Pislaru et al. [16] considered torsional and axial flexibilities of ball-screw drives and employed hybrid, distributed-lumped approach to the modeling of the x -axis dynamics of a milling machine. Varanasi et al. [17] developed distributed-parameter model of the lead-screw drive system by writing second order wave equations in the frequency domain for the longitudinal and torsional dynamics. They implemented Galerkin approach to obtain a low order model. Hybrid finite element models are widely used by researchers to model torsional, axial and lateral flexibilities of ball-screw drives in machine tools. Erkorkmaz et al. [18], Zhou et al. [19], and Kamalzadeh et al. [20] implemented finite element beam formulations to model torsional and axial flexibilities of ball-screw drives. Zaeh et al. [21], and Okwudire et al. [22] included lateral dynamics in their models as well as torsional and axial modes. These hybrid FE models are capable of predicting the ball-screw dynamics despite different locations of the table and nut along its stroke. In other words, they handle the varying boundary conditions.

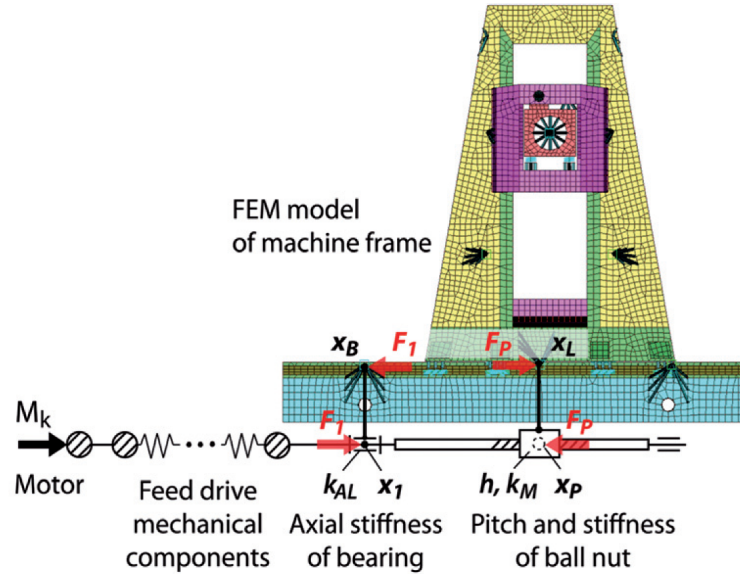


Figure 2.1: Hybrid model of machine tool [1].

Vesely [1] implemented modular approach to represent dynamics of ball-screw drive considering its torsional and axial flexibilities; he also employed finite element methods to model machine frame (Figure 2.1). Coupling these two models resulted in a hybrid model which includes ball-screw and frame structural dynamics.

Moreno-Castaneda et al. [23, 24] used transmission line modeling, quite similar to distributed parameter approach, to make an analogy between elements in transmission line and ball-screw feed drives. The developed model was based on linear elements even though the real feed drive system has non-linearities such as friction and backlash. Pislaru et al. [25] extended this work and presented a dynamic model of a non-linear control systems; they utilized transmission line modeling approach to model friction and backlash.

Figure 2.2 compares complexity, accuracy, and computational cost of different modeling techniques reviewed in this section. In Chapter 3, the modular approach is used, because of its simplicity, to write governing equations and provide a better understanding on how structural vibrations affect the feed drive transfer function in a C-frame milling machine. Linear and torsional springs are used to model the column bending as well as the axial and torsional

modes of ball-screw. Moreover, results of a full finite element model are also presented to demonstrate how FE methods are beneficial in predicting the effect of structural vibrations in control loop.

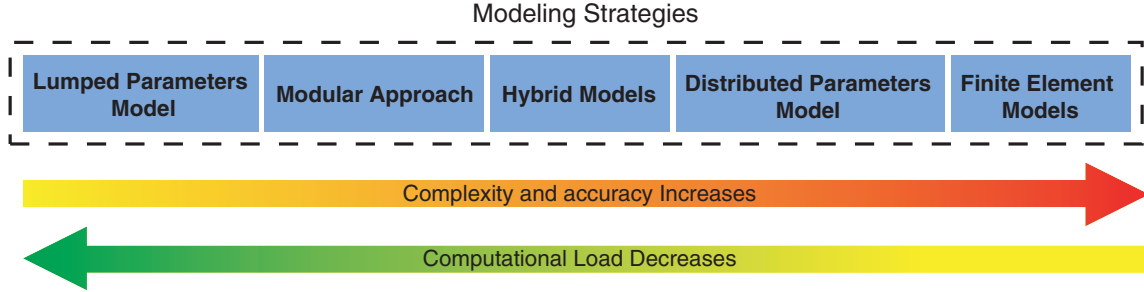


Figure 2.2: Comparison of modeling strategies

2.3 Identification of Machine Tool Dynamics

Accurately identified transfer functions are essential for designing complex control laws which fulfill desired performance specifications. Several strategies are proposed in literature for accurate identification of transfer functions from plant input (i.e position command, voltage, torque) to desired output (i.e. position, velocity, or acceleration). These approaches can generally be divided into two main groups. The first group includes procedures applicable to identify open loop transfer function and the second one deals with closed loop identification.

The traditional procedure for open loop identification of rigid body dynamics is called Ad-Hoc technique [26]. In this method the main effort is to force the simulated response to be as identical as possible with experimental results in time domain. Despite its simplicity, this method provides good estimates of the equivalent inertia, viscous damping coefficient and coulomb friction parameters, and is therefore favorable. Ad-Hoc technique is off-line, time consuming and needs an initial estimation of parameters which are to be identified.

Least Squares Estimation [27] is another approach widely used for identification of transfer functions. This is based on obtaining the discrete time (z-domain) equivalent of the transfer

function in continuous time (Laplace) domain and implementation of least squares optimization to minimize a desired cost function. The cost function can be defined in frequency or time domain. This approach is off-line, but more accurate than Ad-Hoc technique.

Recursive Least Squares identification [28] is an on-line algorithm which updates the identified parameters at each sampling period based on measurements prior to that sampling time. This approach is usually used in conjunction with adaptive controllers where plant parameters (e.g workpiece mass) change with time.

Erkorkmaz et al. [3] proposed Unbiased Least Squares (ULS) identification technique to find equivalent inertia, viscous damping coefficient and coulomb friction in positive and negative directions. Identification of these parameters is based on open-loop response of machine tool feed drive to a step shaped voltage command. This method is off-line too but more accurate than both Ad-Hoc and Least Squares techniques because it takes account for coulomb friction in finding the unknown parameters. The ULS technique is fast and identifies all the parameters together. In other words, there is no need to do separate experiments to obtain coulomb friction specifications.

The literature covered so far are mostly used for identification of rigid body dynamics. To include structural flexibilities in the mathematical model of the open loop, usually frequency response function (FRF) curve fitting is used. Casquero et al. [29] supplied a periodic Chirp signal in open-loop and took Fast Fourier Transform (FFT) of input and output signals to obtain the first resonance mode. Erkorkmaz et al. [30] used sine sweeping technique to measure FRF and implemented curve fitting techniques to obtain the transfer function from ball-screw actuating torque to linear position of the table.

The aforementioned techniques are concerned with open loop identification. However, in some cases, where it is not possible to conduct open loop experiments (e.g commercial CNC machines) or closed loop transfer function is required to design controllers (ZPETC [31]), we need to identify the closed loop transfer function. Tung et al. [32] assumed ARX, ARMAX,

and OE structures for the closed loop system. They implemented least squares, constrained least squares, and most likelihood estimator to identify the transfer function parameters in discrete time domain, and used the identified model to design feed-forward tracking controller. Yang et al. [33] considered the System Under Test (SUT) as a gray box and adopted ARX structure. They proposed two approaches for plant identification: Total Discrete Estimation (TDE) and Partial Continuous Estimation (PCE). They showed that the identification based on TDE approach is more precise. They also evaluated the effect of sampling time on accuracy of identified parameters and demonstrated that a faster sampling rate does not essentially result in better identification results. In other words, the proper selection of sampling time is affected by servo drive time constant.

The machine tool used in this project is controlled by a D-Space based open architecture CNC; therefore, it is possible to control each axis in open loop. Since the open loop identification methods bypass the complex control laws, they provide more accurate mathematical representations of feed drives dynamics than close loop identification algorithms. Hence, in Chapter 3, the procedure of developing an analytical model of feed drive dynamics based on fitting a transfer function to experimentally obtained FRF is explained. The described procedure is implemented in Chapter 4 for experimental identification.

2.4 Vibration Reduction in Production Machines

Vibration of flexible components in manipulators and production machines, such as robotic arms and machine tool feed drives, has received strong attention during past decades. Several techniques have been proposed and numerous instruments were developed to reduce the undesired vibrations. A literature review shows that the vibration reduction approaches can generally be categorized into two main streams: *avoidance* and *suppression*.

Vibration avoidance techniques are concerned with modification of supplied command to

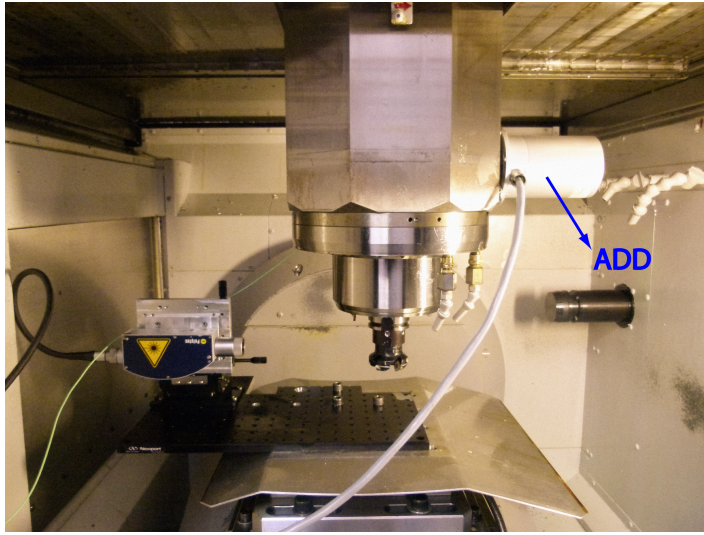
the drives to reduce excitation of structural dynamics. Trajectories with discontinuities in velocity, acceleration, and jerk profiles have relatively wider frequency content which excite machine's natural frequencies and lead to inertial vibrations. Trajectories having limited jerk [34] and continuous jerk [35] profiles are presented in literature to develop smooth reference commands. These trajectories exhibit lower frequency content at high frequency region compared to those with acceleration limited profiles; however, they still cause inertial vibrations in machines with low frequency structural modes. Pre-filtering the motion commands prior to be given to the machine with low-pass or notch filters has been quite advantageous for vibration avoidance by removing the frequency content of reference command which excites the structural modes [5]. However, the real time filters introduce delays and, in the case of low frequency modes, they limit the bandwidth of servo loop which reduces the productivity.

Singer and Seering [36] introduced *command shaping* as a method which can be applied to any trajectory to remove desired harmonics of the given command to the machine. In this approach, a sequence of pre-designed impulses, known as *command shaper*, is convoluted by the reference command, and the result is a modified trajectory which does not excite the modes of interest. They also presented different procedures for designing the impulses sequence which can provide a robust vibration avoidance, when slight shift in natural frequency or damping ratio exists. Although command shaping is highly efficient in vibration reduction, it adds considerable delay, distorts the given trajectory and results in geometrical contour errors [37]. Altintas and Khoshdarregi [38] utilized input shaping to reduce excitation of natural frequencies, and implemented a contouring error compensation algorithm to reduce trajectory distortion and improve contouring performance. It must be noted that, all these vibration *avoidance* techniques only prevent excitation of the structural modes due to supplied reference command, and are not beneficial in reducing vibrations caused by disturbances during machining operations.

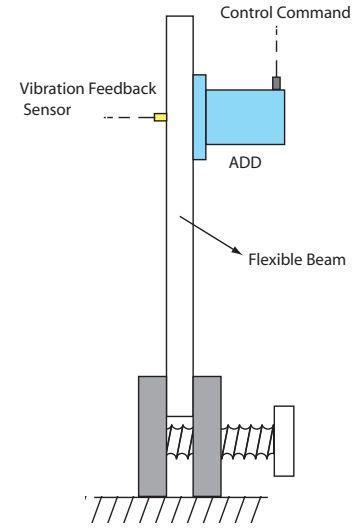
On the other hand, vibration suppression techniques known in literature as active damping are concerned with minimizing *generated* vibrations which are *sensible* through feedback

2.4. Vibration Reduction in Production Machines

sensors mounted on the machine. In other words, in active damping, a sensor (i.e. accelerometer) is added to the machine to measure vibrations in real time; an external actuator or machine servo drive itself is used in a feed back loop to generate suppressing force based on the measured vibrations. Therefore, efficiency of active damping is limited by the bandwidth of actuators and possibility of measuring vibration through feedback sensor.



(a) ADD attached to the spindle



(b) ADD attached to a flexible beam

Figure 2.3: Electromagnetic active damper

The external actuators can be electromagnetic, piezoelectric or hydraulic [5]. They can be directly attached to the flexible structure. However, incorporating external active dampers in design of CNC machines can be difficult and more costly. Figure 2.3 shows a schematic diagram of an industrial active damping device (ADD) attached to a flexible structure. In machine tools industry, external actuators are usually used to improve chatter stability by enhancing structural damping which allows larger maximum depth of cut for a stable cutting process [39].

Drive-based vibration reduction is achieved by using the machine tool feed drives or servo motors in joints of the robotic arms. For this purpose, the control loop is modified to increase

damping ratio for target modes. The damping enhancement is usually achieved through adding another feedback loop to increase the damping of the mode of interest while the outer loop takes care of accurate positioning of manipulator arm. The existing literature concerning how to design the active damping loop is very rich. Banavar and Dominic [40] considered a Linear Quadratic Gaussian (LQG) controller to provide adequate damping to the flexible modes and implemented an H_∞ controller in the outer loop to satisfy robustness toward unstructured perturbations. Symens et al. [41] used a gain-scheduling controller to reduce vibrations of the first structural mode in a pick and place machine, natural frequencies of which change for different lengths of the handling arm. Verschure et al. [42] incorporated an H_∞ controller in the internal loop to force a pick and place machine track a reference acceleration and lead-lag controller for the position loop to follow the reference position command.

Mahmood et al. [43] proposed a resonant controller structure in the internal loop to increase the damping for the flexible structure, and cascaded an integrator in the outer loop to eliminate steady state error in positioning of a flexible manipulator. However, the resonant controller is not robust with respect to variation of the system natural frequency. Dietmair and Verl [44] came up with the idea of compensating the phase delay of flexible structure at its natural frequencies in the internal loop through designing a damping network with incorporating phase compensators and band-pass filters. The simplicity of designing the active damping network without imposing significant computational load has made this approach favorable. This method can easily be applied to any flexible structure, and does not need a precise knowledge of the dynamic behavior of the machine. Moreover, it is relatively robust compared to non-modeled dynamics and frequency shift. Kenneth NG [26] implemented this approach to damp out the bending mode vibrations of a flexible beam, clamped to a fast linear driven motor, by using acceleration feedback with a gain of unity at its natural frequency.

In the field of machine tools, Chen and Tlustý [45] compared the functionality of using accelerometric feed back and an external tuned damper for vibration reduction of feed

drives. They also cascaded a feed-forward controller to improve tracking performance. Results showed that using accelerometric feedback for suppression of machine table's vibrations is quite efficient and also improves chatter stability in cutting process. However, due to the feed-forward controller, it was not robust to dynamic variations of drive train. Pritschow et al. [46] used Ferrari sensor to feedback the angular acceleration of the ball-screw drive and damp the vibrations.

Adaptive sliding mode controllers are used to effectively compensate and damp out the torsional and axial modes of ball-screw drives by Kamalzadeh and Erkorkmaz in [20] and [30] resulting in controllers with significant enhanced bandwidth. Altintas and Okwudire [47] proposed a disturbance adaptive sliding mode controller to enhance dynamic stiffness of a *direct driven* feed drive against cutting force and increased the servo loop bandwidth. Erkorkmaz and Kamalzadeh [18] suppressed the ball-screw's torsional mode by giving a canceling signal proportional to its twist angle measured by subtracting the outputs of two rotary encoders placed at either ends of the ball-screw.

The aforementioned methods are based on nominal frequency of vibration modes and do not include dynamic variations which, if large enough, can cause destabilization of control loop and saturation of actuators. To include dynamic variation of feed drives, Van Brussel [12] designed an H_∞ controller based on nominal position of the machine tool with incorporating the information about dynamic variations in model uncertainties. The developed controller showed a better performance in suppressing vibrations but demonstrated a worse disturbance rejection compared to a reference PID controller designed based on rigid body dynamics. Hanifzadegan and Nagamune [48] proposed a switching gain scheduling controller to reduce vibrations and achieve performance robustness despite varying position-dependent stiffness of ball-screw drive.

Figure 2.4 presents an overview of vibration reduction techniques explained in this section. Regarding to the simplicity and relative robustness of the active damping approach proposed

by Dietmair and Verl [44], this method is implemented in Chapter 5 to design the phase compensator in the internal feedback loop. The added feedback loop increases damping of the axial mode of ball-screw and reduces the vibrations significantly.

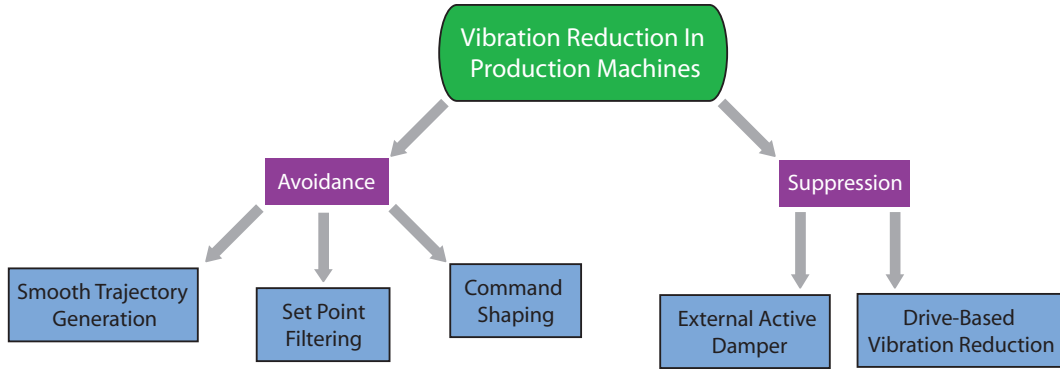


Figure 2.4: Vibration reduction approaches in production machines

2.5 Summary

A concise overview of existing literature in the field of modeling, identification, and vibration reduction in production machines are presented in this chapter. It is known that the modular approach is the simplest way of modeling structural flexibilities for controller design and simulation purposes. It was highlighted that open loop identification result in a better estimation of system parameters due to intrinsic bypassing of the complex control laws. Finally, vibration reduction approaches in production machines were investigated under two main groups of *avoidance* and *suppression*.

In this thesis, the mathematical model, developed based on the modular approach, for a C-frame machine tool is identified by utilizing frequency domain curve fitting algorithms. The identified model is used to reduce machine vibrations by modifying the servo control loop.

Chapter 3

Mathematical Modeling of Structural Dynamics

3.1 Overview

The previous chapters, mentioned that inertial loads excite structural flexibilities and lead to residual vibrations. This chapter focuses on developing a mathematical model which explains how feedback sensors mounted on the machine can pick up these vibrations. In developing the model, the fundamental modes of the machine tool column and ball-screw drive are considered. These modes have low eigen-frequencies and can be excited by inertial loads. The chapter is organized as follows: Section 3.2 introduces and compares ball-screw and linear driven feed drives which are widely used in industry. Section 3.3 presents the mathematical modeling procedure and the chapter is summarized in Section 3.4.

3.2 Machine Tool Feed Drives

Feed drives are a part of the control loop used for positioning the cutting tool and workpiece to the desired location in the machine tools [5]. These electromechanical actuators are classified as linear motors and ball-screw feed drives. Ball-screw feed drives (Figure 3.1) are an assembly of the coupling, ball-screw, and nut to convert the rotational motion generated by servo-motor to linear displacement at machine table. In some cases, a torque reduction gear set is placed

3.2. Machine Tool Feed Drives

between the servo-motor and the coupling. Each rotation of the ball-screw is converted to a pitch length linear travel of machine table through nut interface. The existence of several components in the drive train makes the driven inertia by rotary motors larger than that for linear drives.

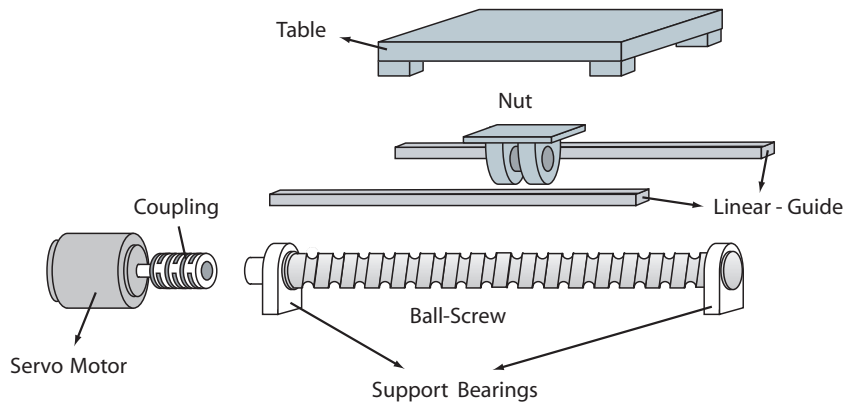


Figure 3.1: Ball-screw feed drive

The linear motor structure (Figure 3.2) is quite similar to an electric motor which its stator and rotor are unrolled. Therefore, the interaction between magnetic field of stator and rotor generates a linear force causing the armature, serving as machine table, to move linearly.

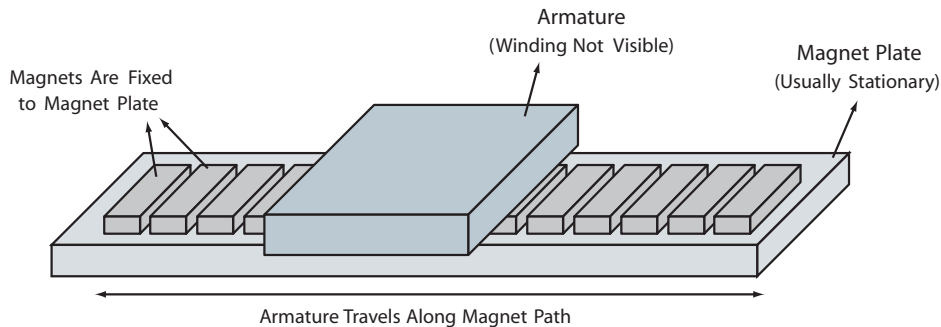


Figure 3.2: Linear drive

The existence of nut and gear set in ball-screw feed drives mitigate the effect of cutting force and inertial changes on servo loop performance. It also makes them suitable for moving large and heavy workpieces without a significant increase in motor size. Therefore, the ball-

screw's inherent "gear reduction" in addition to their lower cost have made them favorable in heavy-duty commercial CNC machines. However, the large inertia reflected on motor shaft limits their speed, acceleration and achievable bandwidth. Because of the flexibility of the long ball-screw shaft and wear in mechanical drive components, their motion delivery is not perfect [49]. In the cases of light workpieces and small mass variations linear drives are preferred because of their higher speed and acceleration capability.

Despite the widespread usage of ball-screw drives, they have several drawbacks: positioning of machine table at different locations changes supporting condition and causes ball-screw drives to have varying dynamics. Therefore, if the controller is designed based on identified parameters for one position (e.g table in the middle), the closed loop performance would not be optimal for operation of the machine in the whole travel length. Researchers have considered these dynamic variations in controller design and employed robust control approaches to tackle this problem [41]. Another concern about ball-screw drives is a non-linear phenomena called backlash which is due to the clearance in joints; however, this can be minimized by using preloaded balls in nut interface.

3.3 Mathematical Modeling of Feed Drives

The most common way of modeling the drive train in machine tools is to neglect the structural flexibilities and consider all of the elements as lumped masses connected with rigid links. Primarily, this approach is used to develop a rigid body model of a ball-screw drive. The modular approach is utilized to incorporate the ball-screw and column flexibilities in the mathematical model of a C-frame machine tool as shown in Figure 3.3.

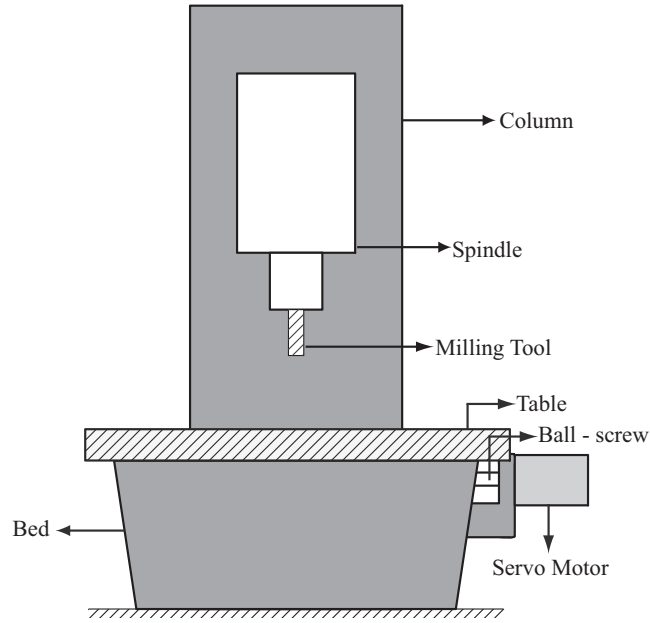


Figure 3.3: Schematic diagram of a C-frame milling machine

3.3.1 Rigid Body Model of the Ball-Screw Drive

Figure 3.4 shows schematic diagram of a ball-screw drive:

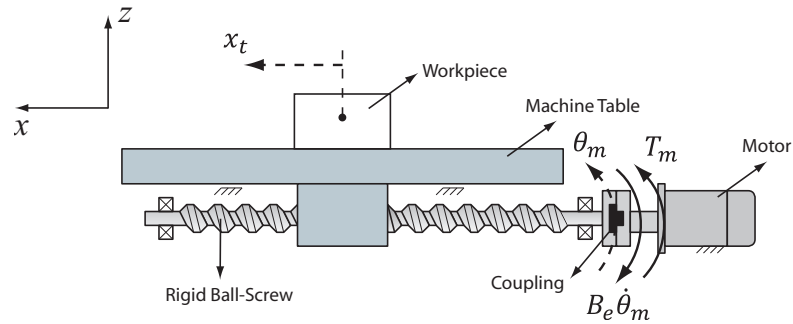


Figure 3.4: Rigid ball-screw mounted on a rigid bed

In rigid body modeling, all the flexibilities in the column, bed, ball-screw, coupling and bearings are neglected and they are assumed as rigid links and joints. Therefore, the angular displacement at motor shaft (θ_m) and nut (θ_n) are the same. The angular displacement is converted to linear motion at machine table (x_t) through the screw-nut interface. For each

rotation of the screw, machine table moves for a screw pitch length (h_p). The machine table displacement (x_t) is a function of angular motion at ball-screw and nut interface (θ_m) as:

$$x_t = r_g \theta_m; r_g = \frac{h_p}{2\pi} \quad (3.1)$$

where r_g is the nut transformation ratio. The actuating torque applied by servo motor (T_m) drives the equivalent inertia (J_e) and opposes the viscous friction torque ($B_e \frac{d\theta_m}{dt}$) reflected at the motor shaft. Therefore, the angular displacement at motor shaft can be modeled as:

$$T_m - B_e \frac{d\theta_m}{dt} = J_e \frac{d^2\theta_m}{dt^2} \quad (3.2)$$

combining Equations 3.1 and 3.2 and taking Laplace transform we have:

$$T_m(s) - \frac{B_e}{r_g} \frac{dx_t}{dt} = \frac{J_e}{r_g} s^2 x_t(s) \quad (3.3)$$

by organizing Equation (3.3), the transfer function between actuating torque and table linear displacement is:

$$G_t(s) \left[\frac{m}{N.m} \right] = \frac{x_t(s)}{T_m(s)} = \frac{r_g}{s(J_e s + B_e)} \quad (3.4)$$

in CNC machines, when linear encoder is used for position feedback measurements, the optical head of linear encoder is usually mounted on machine bed and the scale is placed on the machine table. Therefore, the linear encoder outputs the relative displacement between machine table and machine bed. In rigid-body modeling, it is assumed that the whole drive train is mounted on a rigid base, machine bed, and its displacement is zero. As a result, the encoder output is the same as absolute displacement of the machine table with respect to a stationary reference outside the machine. Hence, the transfer function between the linear encoder output and the actuating torque ($G_e(s)$) equals to $G_t(s)$.

3.3.2 Flexible Ball-Screw Model

Ball-screw drives used as machine tool feed drives exhibit axial and torsional flexibilities. In ball-screws with large pitch length and *light weight* table, the torsional deformation causes shrinkage and elongation in the axial direction attributed to Poisson's ratio (ν). This variation in length will be reflected as an axial displacement on the machine table. Therefore, there is a coupling between axial and torsional modes.

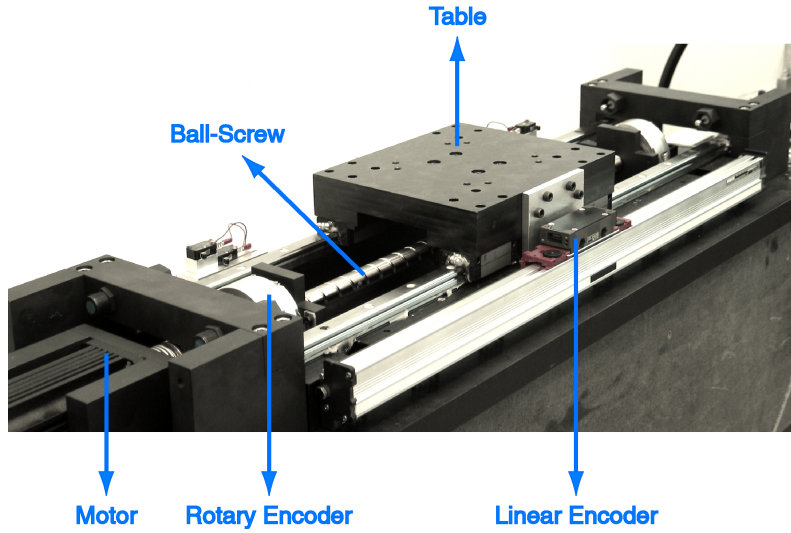


Figure 3.5: Ball-screw feed drive - UBC Mechatronics Laboratory

The torsional flexibility of a single axis ball-screw shown in Figure 3.5 (hereinafter known as ball-screw test bed) is modeled as a torsional (k_{ts}) spring with its associated damping (c_{ts}) connecting the inertias reflected at the motor (J_m) and the nut (J_n) as shown in Figure 3.6. The whole assembly is assumed to be mounted on a rigid bed. This setup consists of a ball-screw with a pitch length of 20 [mm] constrained axially by a thrust bearing at the closer end to the motor; a radial ball bearing is used to constrain the other end. It is driven by a brush-less DC motor connected to the ball screw through a bellow-type coupling. A linear encoder with 0.05 [μm] resolution attached to the table, and a rotary encoder with 0.1 [μm] mounted on the motor shaft are used for table position measurement. The test bed can have 1 [g] acceleration

3.3. Mathematical Modeling of Feed Drives

and maximum velocity of 27 [m/min].

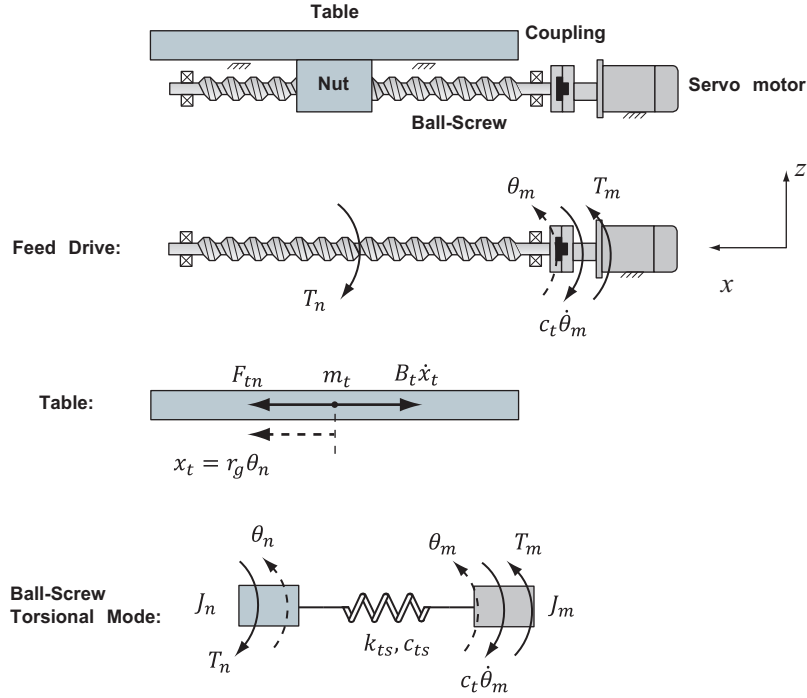


Figure 3.6: Flexible ball-screw mounted on a rigid bed

The linear force (F_{tn}) applied from the nut moves the machine table mass (m_t) on the guide-way. Ignoring external disturbance loads, and considering viscous damping (B_t) in the guide, the table dynamics is expressed as:

$$F_{tn} - B_t \dot{x}_t = m_t \ddot{x}_t; x_t = r_g \theta_n \quad (3.5)$$

The reaction force between machine table and the nut (F_{tn}) is transmitted to the ball screw having transmission ratio of (r_g) as a load torque (T_n):

$$T_n = F_{tn} \times r_g; r_g = \frac{h_p}{2\pi} \quad (3.6)$$

Considering the load torque (T_n) acting where the nut is located, the ball-screw vibrations

at nut interface (θ_n) can be modeled as:

$$-T_n - k_{ts}(\theta_n - \theta_m) - c_{ts}(\dot{\theta}_n - \dot{\theta}_m) = J_n \ddot{\theta}_n \quad (3.7)$$

The electrical servo motor creates torque (T_m), which rotates the motor shaft, coupling, and ball-screw. Therefore, the ball-screw vibrations observed at motor shaft can be expressed as:

$$T_m - c_t \dot{\theta}_m - k_{ts}(\theta_m - \theta_n) - c_{ts}(\dot{\theta}_m - \dot{\theta}_n) = J_m \ddot{\theta}_m \quad (3.8)$$

where θ_m is the angular displacement of the ball-screw at motor shaft and c_t represents the torsional viscous damping coefficient due to the viscous friction in the nut, bearings and the coupling. Taking Laplace transform of Equations (3.5) to (3.8), organizing them in terms of displacements (θ_n , θ_m), and motor torque (T_m) yields the following matrix equation:

$$\begin{bmatrix} \phi_{11} & -(c_{ts}s + k_{ts}) \\ -(c_{ts}s + k_{ts}) & \phi_{22} \end{bmatrix} \begin{bmatrix} \theta_n \\ \theta_m \end{bmatrix} = \begin{bmatrix} 0 \\ 1 \end{bmatrix} T_m \quad (3.9)$$

$$\phi_{11} = [J_n + m_t r_g^2] s^2 + [c_{ts} + B_t r_g^2] s + k_{ts}$$

$$\phi_{22} = J_m s^2 + (c_{ts} + c_t) s + k_{ts}$$

By solving Equation 3.9, the transfer function between machine table displacement (x_t), vibration of the ball-screw at motor shaft (θ_m) and motor torque (T_m) can be obtained as:

$$G_t(s) \left[\frac{m}{N.m} \right] = \frac{x_t(s)}{T_m(s)} = \frac{r_g \theta_n(s)}{T_m(s)} = \frac{r_g (c_{ts}s + k_{ts})}{s(J_e s + B_e)(s^2 + 2\zeta \omega_n s + \omega_n^2)} \quad (3.10)$$

$$G_m(s) \left[\frac{m}{N.m} \right] = \frac{r_g \theta_m(s)}{T_m(s)} = \frac{r_g ([J_m + m_t r_g^2] s^2 + [c_{ts} + B_t r_g^2] s + k_{ts})}{s(J_e s + B_e)(s^2 + 2\zeta \omega_n s + \omega_n^2)} \quad (3.11)$$

where J_e , and B_e are the equivalent inertia and viscous damping constants. ζ and ω_n represent

the damping coefficient and natural frequency of the ball-screw torsion mode. J_e , B_e , ζ , and ω_n can be evaluated from Equation (3.9).

Similar to the case of rigid body modeling in 3.3.1, because of the assumption on rigidity of the bed, the transfer function between linear encoder output and actuating torque ($G_e(s)$) equals to $G_t(s)$. The transfer functions in Equations 3.10 and 3.11 can be written as:

$$G_t(s) = G_r(s) \times G_{ft}(s); G_m(s) = G_r(s) \times G_{fm}(s) \quad (3.12)$$

where the rigid body motion is governed by transfer function:

$$G_r(s) \left[\frac{m}{N.m} \right] = \frac{r_g}{s(J_e s + B_e)}$$

and the structural dynamics part is dominated by one mode as:

$$G_{ft}(s) \left[\frac{m}{m} \right] = \frac{(\alpha_t s + \beta_t)}{(s^2 + 2\zeta \omega_n s + \omega_n^2)}; G_{fm}(s) \left[\frac{m}{m} \right] = K_{fm} \frac{(s^2 + \alpha_m s + \beta_m)}{(s^2 + 2\zeta \omega_n s + \omega_n^2)} \quad (3.13)$$

where K_{fm} , α_t , β_t , α_m , and β_m are functions of the variables used in Equations 3.10 and 3.11. These formulations will be used in identification of structural dynamics in Chapter 4.

3.3.3 Feed Drive In a Flexible Machine Tool

A mathematical model for the x axis feed drive of a three axis vertical machining center (FADAL VMC2216) shown in Figure 3.7 is developed. The model includes dynamics of the modes which are transmitted as axial vibrations of the horizontal (x) drive to the linear encoder. These modes are identified as axial vibrations of the ball screw, and bending and torsional vibrations of the C-framed column. The torsional mode of ball-screw is neglected as its natural frequency is far beyond the bandwidth of servo loop.

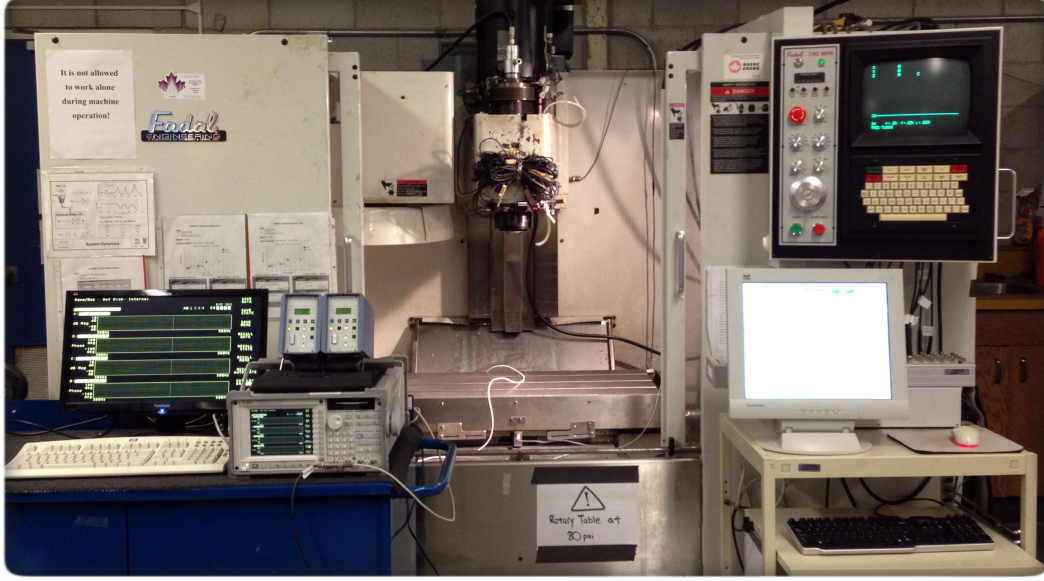


Figure 3.7: FADAL VMC2216 three axis machining center

A brush-less DC motor is used to apply torque to the ball-screw with 10 [mm] pitch length so that the table can have maximum acceleration of 2.5 [m/s^2] and reach maximum velocity of 25.4 [m/min]. Linear and rotary encoders with 1 [μm] resolution are used to measure table position. While the linear scale is mounted on the moving table, the encoder head is mounted on the stationary guide. The motor torque is transmitted to the ball screw with a flexible coupling that has a torsional viscous damping constant of c_t and angular displacement θ_m . (see Figure 3.8):

$$J_m \ddot{\theta}_m = T_m - T_n - c_t \dot{\theta}_m \quad (3.14)$$

where J_m is the total inertia of coupling, motor shaft, ball-screw and nut reflected at the motor shaft. The axial load (F_{tn}) felt at the nut – ball screw is transmitted as the load torque (T_n) as explained before in Equation 3.6.

The total axial displacement of the table (x_t) is the summation of the axial vibration of ball screw reflected at the nut (x_n) and the angular displacement of the ball screw (θ_m) translated as

3.3. Mathematical Modeling of Feed Drives

the axial displacement due to the nut interface:

$$x_t = x_n + r_g \theta_m \quad (3.15)$$

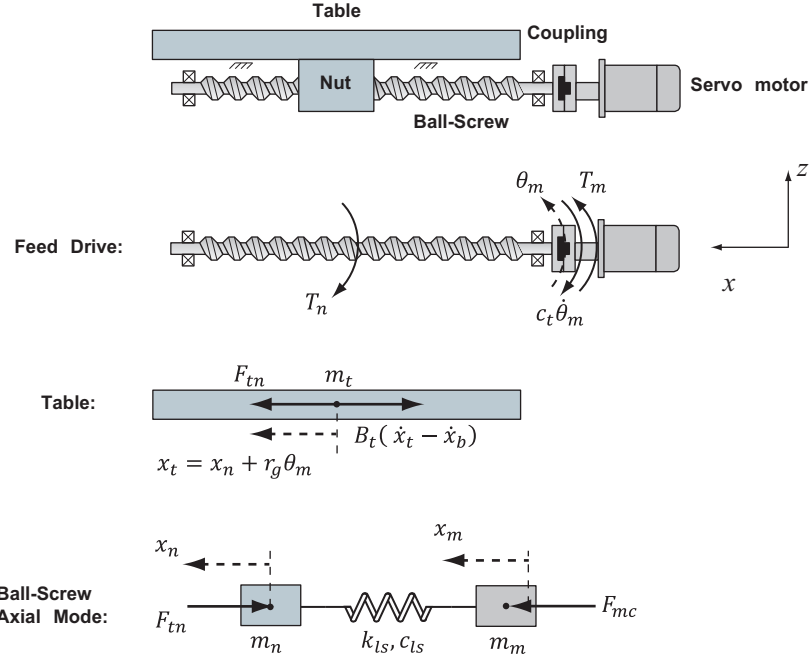


Figure 3.8: Flexible ball-screw model

The axial force (F_{tn}) applied from the nut moves the machine table mass (m_t) on the guide-way of the bed. Ignoring external disturbance loads, and considering viscous damping (B_t) in the guide, the table dynamic is expressed as:

$$m_t \ddot{x}_t = F_{tn} - B_t (\dot{x}_t - \dot{x}_b) \quad (3.16)$$

where $x_t - x_b$ is the relative vibration between the table (x_t) and the bed (x_b). The ball-screw is modeled as an axial spring (k_{ls}) with its associated damping coefficient (c_{ls}) as shown in Figure

of the column (x_c) at its center of gravity (COG) is modeled as:

$$m_c \ddot{x}_c = F_{cb} + B_t (\dot{x}_t - \dot{x}_b) - F_{mc} \quad (3.19)$$

where F_{cb} is the reaction force between the machine column and the ground, and B_t is the viscous friction constant between the bed and table. The (x_{cb}) of the column creates reaction moment (T_{cb}) which is absorbed by the bending stiffness and damping elements at the ground connection:

$$T_{cb} = k_{cb} \theta_{cb} + c_{cb} \dot{\theta}_{cb} \quad (3.20)$$

The moment equilibrium at the center of gravity can be expressed as:

$$F_{mc} R_{mb} - F_{cb} R_{gb} - B_t (\dot{x}_t - \dot{x}_b) R_{bb} - T_{cb} = J_{cb} \ddot{\theta}_{cb} \quad (3.21)$$

where R_{mb} , R_{gb} , and R_{bb} are the moment arms as shown in Figure 3.9. The column's torsional mode is modeled by a rigid mass (m_c) connected to the ground with a torsional spring (k_{tc}) and viscous damping element (c_{tc}) as shown in Figure 3.10.

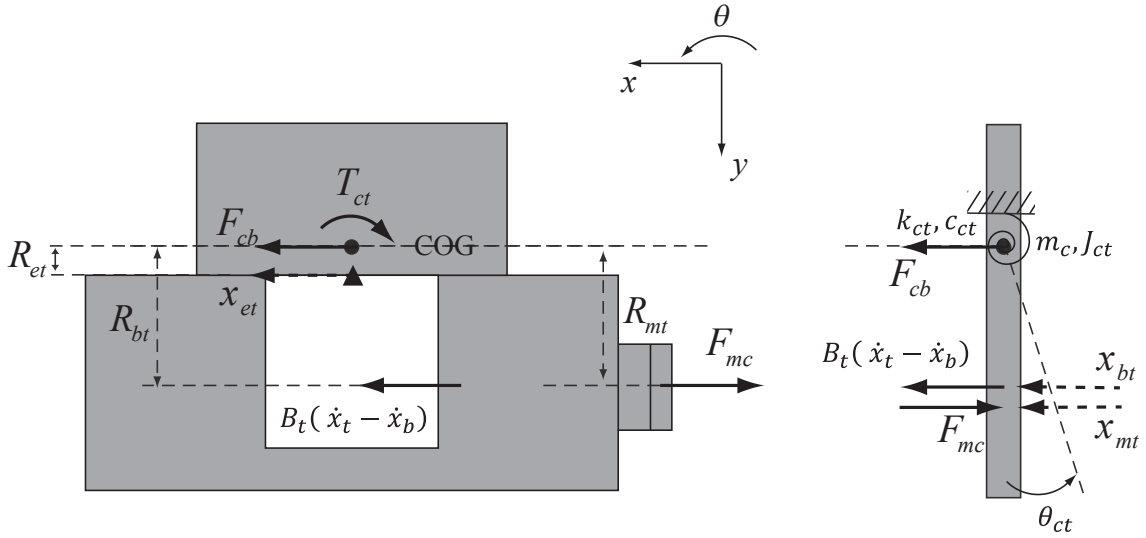


Figure 3.10: Bending mode of flexible machine tool structure

3.3. Mathematical Modeling of Feed Drives

The moment equilibrium around the center of gravity in x-y plane is:

$$-B_t(\dot{x}_t - \dot{x}_b)R_{bt} - T_{ct} + F_{mc}R_{mt} = J_{ct}\ddot{\theta}_{ct} \quad (3.22)$$

where T_{ct} is the reaction torque exerted on the column's center of gravity from the ground due to its torsional vibration (θ_{ct}):

$$T_{ct} = k_{ct}\theta_{ct} + c_{ct}\dot{\theta}_{ct} \quad (3.23)$$

The bending (θ_{cb}) and torsional (θ_{ct}) deflections of column causes linear displacements at the bed (x_b), motor shaft (x_m) and column's center of gravity (x_c) which can be evaluated by superposing the vibrations as:

$$\begin{cases} x_b = x_{bb} + x_{bt} \\ x_m = x_{mb} + x_{mt} \\ x_c = x_{cb} + x_{ct} \end{cases} \quad (3.24)$$

where (x_{bb}, x_{mb}, x_{cb}) and (x_{bt}, x_{mt}, x_{ct}) are contributed by the bending (b) and torsion (t) of the column at the top surface of the bed (b), at the motor shaft (m) and at the center of gravity of column (c), respectively. The torsional vibrations of machine column are assumed to occur at its center of gravity; hence, $x_{ct} = 0$. The linear displacements are estimated from the angular bending and torsional displacements from Figure 3.9 and Figure 3.10 as:

$$x_{bb} = (R_{gb} - R_{bb})\theta_{cb}; x_{bt} = -R_{bt}\theta_{ct} \quad (3.25)$$

$$x_{mb} = (R_{gb} - R_{mb})\theta_{cb}; x_{mt} = -R_{mt}\theta_{ct} \quad (3.26)$$

$$x_c = R_{gb}\theta_{cb} \quad (3.27)$$

where R_{mt} and R_{bt} are the moment arms as shown in Figure 3.10. Taking Laplace transform

of Equations 3.14 to 3.27, organizing them between output displacements (x_n , θ_m , θ_{cb} , θ_{ct}), motor torque (T_m) yields the following:

$$\Phi(s) \begin{bmatrix} x_n(s) \\ \theta_m(s) \\ \theta_{cb}(s) \\ \theta_{ct}(s) \end{bmatrix} = \begin{bmatrix} 0 \\ 1 \\ 0 \\ 0 \end{bmatrix} \times T_m \quad (3.28)$$

where the symmetric transfer function matrix ($\Phi(s)$) is:

$$\Phi(s) = \begin{bmatrix} \phi_{11} & \phi_{12} & \phi_{13} & \phi_{14} \\ \phi_{12} & \phi_{22} & \phi_{23} & \phi_{24} \\ \phi_{13} & \phi_{23} & \phi_{33} & \phi_{34} \\ \phi_{14} & \phi_{24} & \phi_{34} & \phi_{44} \end{bmatrix} \quad (3.29)$$

$$\phi_{11} = [m_n + m_t] s^2 + [c_{ls} + B_t] s + k_{ls}$$

$$\phi_{12} = [m_t s^2 + B_t s] r_g$$

$$\phi_{13} = [c_{ls} s + k_{ls}] (R_{mb} - R_{gb}) + B_t (R_{bb} - R_{gb}) s$$

$$\phi_{14} = [c_{ls} s + k_{ls}] R_{mt} + B_t R_{bt}$$

$$\phi_{22} = [J_m + m_t r_g^2] s^2 + [c_t + B_t r_g^2] s$$

$$\phi_{23} = B_t (R_{bb} - R_{gb}) r_g s$$

$$\phi_{24} = B_t R_{bt} r_g s$$

$$\begin{aligned} \phi_{33} = & \left[J_{cb} + m_c R_{gb}^2 + m_m (R_{gb} - R_{mb})^2 \right] s^2 + \left[c_{cb} + c_{ls} (R_{gb} - R_{mb})^2 + B_t (R_{gb} - R_{bb})^2 \right] s \\ & + \left[k_{cb} + k_{ls} (R_{gb} - R_{bb})^2 \right] \end{aligned}$$

$$\phi_{34} = [m_m s^2 + c_{ls} s + k_{ls}] (R_{mb} - R_{gb}) R_{mt} + B_t R_{bt} (R_{bb} - R_{gb}) s$$

$$\phi_{44} = [J_{ct} + m_m R_{mt}^2] s^2 + [c_{ct} + c_{ls} R_{mt}^2 + B_t R_{bt}^2] s + [k_{ct} + k_{ls} R_{mt}^2]$$

The transfer functions between the total displacement of table (x_t), total displacement of bed at the point where encoder optical head is mounted (x_{be}) and motor torque (T_m) can be evaluated from Equation (3.28) as:

$$G_t(s) \left[\frac{m}{N.m} \right] = \frac{x_t(s)}{T_m(s)} = \frac{x_n(s) + r_g \theta_m(s)}{T_m(s)} = \frac{\sum_{i=0}^6 p_i(s) s^i}{s(J_e s + B_e) \prod_{j=1}^3 (s^2 + 2\zeta_j \omega_{nj} s + \omega_{nj}^2)} \quad (3.30)$$

$$\begin{aligned} G_{be}(s) \left[\frac{m}{N.m} \right] &= \frac{x_{be}(s)}{T_m(s)} = \frac{(R_{gb} - R_{bb}) \theta_{cb}(s) - R_{et} \theta_{ct}}{T_m(s)} \\ &= \frac{\sum_{i=0}^4 q_i(s) s^4}{s(J_e s + B_e) \prod_{j=1}^3 (s^2 + 2\zeta_j \omega_{nj} s + \omega_{nj}^2)} \end{aligned} \quad (3.31)$$

where J_e and B_e are the equivalent inertia and viscous damping constants, and ζ_j , ω_{nj} are the damping coefficient and the natural frequency of the mode i . A linear encoder is used to measure the relative displacement between machine table (x_t) and bed (x_{be}) in x direction ($x = x_t - x_{be}$). Its location is shown by a filled triangle in Figures 3.9 and 3.10. The transfer function between the relative table position (x) and motor torque (T_m) can be obtained as:

$$G_e(s) \left[\frac{m}{N.m} \right] = G_t(s) - G_{be}(s) = \frac{x(s)}{T_m(s)} = \frac{x_t(s) - x_{be}(s)}{T_m(s)} = G_r(s) G_f(s) \quad (3.32)$$

where the rigid body motion is governed by transfer function:

$$G_r(s) \left[\frac{m}{N.m} \right] = \frac{r_g}{s(J_e s + B_e)} \quad (3.33)$$

and the structural dynamics part is dominated by three modes as:

$$G_f(s) \left[\frac{m}{m} \right] = \frac{\sum_{i=0}^6 l_i(s) s^i}{\prod_{i=1}^3 (s^2 + 2\zeta_i \omega_{ni} s + \omega_{ni}^2)} \quad (3.34)$$

The objective is to predict and control the relative vibrations (x) between the table and bed, which are felt by the position feedback sensor, the linear encoder.

3.4 Summary

This chapter presented the modeling of feed drives by taking structured flexibilities into account. The flexibilities contribute to low frequency vibrations of machine tools, and they are used to obtain the transfer function between motor torque and table displacement. For a light weight table, driven with a ball-screw, the coupled torsional-axial flexibility of the ball-screw is considered. A similar approach is extended to incorporate column flexibilities as torsional springs in modeling the feed drive of a typical C-frame CNC machine. It is shown that the transfer function between motor torque and table displacement is the product of $G_r(s)$ for rigid body dynamics and $G_f(s)$ for structural flexibilities. Because the machine components are connected through joints and couplings, flexibilities of the column are reflected on machine table as residual vibrations. These vibrations are observable through feedback sensors provided that they have sufficient resolution.

Chapter 4

Experimental Identification of Feed Drive Dynamics

4.1 Overview

This chapter concentrates on identification of the mathematical models developed in Chapter 3 for the ball-screw test bed and the vertical machining center (FADAL). Sections 4.2 to 4.4 present the identification procedure of the transfer functions which explain the rigid body and structural dynamics. Experimental identification results for the ball-screw test bed and the flexible machine tool (FADAL) are covered in Section 4.5. The identified mathematical model for FADAL is validated in Section 4.6 through simulating its dynamics in control loop and comparing the results with experiment. Section 4.7 evaluates the efficiency of finite element methods in predicting machine dynamics by comparing the experimentally measured FRF with the simulated FRF obtained from FEM. This chapter is summarized in Section 4.8.

4.2 Identification of Rigid Body Dynamics ($G_r(s)$)

Erkorkmaz et al. [3] proposed the Unbiased Least Squares approach to identify rigid body dynamics of machine tool feed drives. This approach is based on the rigid body model of the ball-screw drive developed in Section 3.3.1.

$$x(s) = \frac{r_g}{s(J_e s + B_e)} T_m(s)$$

Including the effect of disturbance torque (T_d) reflected on the motor shaft due to the friction and cutting forces, Equation (3.4) is modified as:

$$x(s) = \frac{r_g}{s(J_e s + B_e)} [T_m(s) - T_d(s)] \quad (4.1)$$

The control signal input ($u[V]$) is used to excite the axis dynamics. The applied torque to the ball-screw drive (T_m) can be obtained by multiplying the input voltage by amplifier and motor constants ($k_a[A/V], k_t[N.m/A]$) as:

$$T_m(s) = k_a k_t u(s) \quad (4.2)$$

Having the amplifier gain (k_a) and motor constant (k_t) known, the disturbance torque (T_d) is regarded as a disturbance equivalent voltage (d) to facilitate its estimation. Therefore, Equation (4.1) can be written in terms of the commanded (u) and disturbance (d) voltages as:

$$x(s) = \frac{k_a k_t r_g}{s(J_e s + B_e)} [u(s) - d(s)] \quad (4.3)$$

The machine table velocity measured by digital differentiation of the linear encoder signal can be expressed in terms of control input (u) and equivalent input disturbance (d) as:

$$v(s) = s x(s) = \frac{k_a k_t r_g}{J_e s + B_e} [u(s) - d(s)] \quad (4.4)$$

Considering $P_v = \frac{K_a K_t r_g}{J_e}$, and $Q_v = -\frac{B_e}{J_e}$, the derivative of table velocity in Laplace domain

can be obtained by rewriting Equation (4.4) in the following form:

$$sv(s) = P_v [u(s) - d(s)] + Q_v v(s) \quad (4.5)$$

Equations (4.3) to (4.5) can be expressed in state space notation as:

$$\begin{bmatrix} \dot{x}(t) \\ \dot{v}(t) \end{bmatrix} = \underbrace{\begin{bmatrix} 0 & 1 \\ 0 & Q_v \end{bmatrix}}_{A_c} \begin{bmatrix} x(t) \\ v(t) \end{bmatrix} + \underbrace{\begin{bmatrix} 0 & 0 \\ P_v & -P_v \end{bmatrix}}_{B_c} \begin{bmatrix} u(t) \\ d(t) \end{bmatrix} \quad (4.6)$$

The input voltage to the motor is commanded through a D/A converter; the table position and velocity are measured by sampling the encoder signal at discrete time intervals (T_s). Hence, Equation (4.6) expressed in discrete-time domain with a zero-order hold at the input stage is:

$$\begin{bmatrix} x(k+1) \\ v(k+1) \end{bmatrix} = A_d \begin{bmatrix} x(k) \\ v(k) \end{bmatrix} + B_d \begin{bmatrix} u(k) \\ d(k) \end{bmatrix} \quad (4.7)$$

where $A_d = e^{A_c T_s}$, $B_d = \int_0^{T_s} e^{A_c \lambda} d\lambda \cdot B_c$

Following the calculations presented in Appendix A, A_d and B_d are as follows:

$$A_d = \begin{bmatrix} 1 & -e^{Q_v T_s} \\ 0 & e^{Q_v T_s} \end{bmatrix}, \quad B_d = \frac{P_v}{Q_v} (e^{Q_v T_s} - 1) \begin{bmatrix} -1 & 1 \\ 1 & -1 \end{bmatrix} \quad (4.8)$$

By defining $Q_{vd} = e^{Q_v T_s}$ and $P_{vd} = \frac{P_v}{Q_v} (e^{Q_v T_s} - 1)$, Equation (4.7) results in the following recursive equation:

$$v(k) = Q_{vd} v(k-1) + P_{vd} (u(k-1) - d(k-1)) \quad (4.9)$$

In identification process, the only disturbance acting on the feed drive is Coulomb friction (d_f) in the guid-way, nut and bearings. The traditional approach to model Coulomb friction is assigning two constant values to the applied disturbance in positive and negative directions. Therefore, d_f can be expressed as follows:

$$d_f(v(k)) = \begin{cases} d_f^+ & \text{if } v(k) > 0 \\ 0 & \text{if } v(k) = 0 \\ d_f^- & \text{if } v(k) < 0 \end{cases} \quad (4.10)$$

The friction model in Equation (4.10) can be reformulated as:

$$d_f(v(k)) = PV(v(k)) \cdot d_f^+ + NV(v(k)) \cdot d_f^- \quad (4.11)$$

$$\begin{cases} PV = \text{Positive Velocity} = \frac{1}{2} \sigma(v(k)) \cdot (1 + \sigma(v(k))) \\ NV = \text{Negative Velocity} = -\frac{1}{2} \sigma(v(k)) \cdot (1 - \sigma(v(k))) \end{cases} \quad (4.12)$$

where σ is the sign function.

$$\sigma(v(k)) = \begin{cases} 1 & \text{if } v(k) > 0 \\ 0 & \text{if } v(k) = 0 \\ -1 & \text{if } v(k) < 0 \end{cases} \quad (4.13)$$

By incorporating Equation (4.11) into Equation (4.9), we have:

$$\begin{aligned} v(k) = & Q_{vd}v(k-1) + P_{vd}u(k-1) - \\ & P_{vd}PV(v(k-1))d_f^+ - P_{vd}NV(v(k-1))d_f^- \end{aligned} \quad (4.14)$$

or in matrix form:

$$\underbrace{v(k)}_{Y(k,1)} = \underbrace{\begin{bmatrix} v(k-1) & u(k-1) & -PV(v(k-1)) & -NV(v(k-1)) \end{bmatrix}}_{\Gamma(K,1)} \underbrace{\begin{bmatrix} Q_{vd} \\ P_{vd} \\ P_{vd}d_{f+} \\ P_{vd}d_{f-} \end{bmatrix}}_{\Theta} \quad (4.15)$$

Writing equation (4.15) for each sampling time, results in the following matrix equation:

$$\underbrace{\begin{bmatrix} v(2) \\ v(3) \\ \vdots \\ v(N) \end{bmatrix}}_Y = \Gamma \underbrace{\begin{bmatrix} Q_{vd} \\ P_{vd} \\ P_{vd}d_{f+} \\ P_{vd}d_{f-} \end{bmatrix}}_{\Theta} + \underbrace{\begin{bmatrix} e(2) \\ e(3) \\ \vdots \\ e(N) \end{bmatrix}}_E$$

Where N is the total number of sampled data, and

$$\Gamma = \begin{bmatrix} v(1) & u(1) & -PV(v(1)) & -NV(v(1)) \\ v(2) & u(2) & -PV(v(2)) & -NV(v(2)) \\ \vdots & \vdots & \vdots & \vdots \\ v(N-1) & u(N-1) & -PV(v(N-1)) & -NV(v(N-1)) \end{bmatrix} \quad (4.16)$$

Solving equation (4.16) by using least squares technique to minimize the error vector (E) gives the unknown matrix (Θ) as:

$$\Theta = (\Gamma^T \Gamma)^{-1} \Gamma^T Y \quad (4.17)$$

The first and second element of Θ are Q_{vd} and P_{vd} , respectively. d_{f+} and d_{f-} can be obtained

by dividing the third and fourth components by K_{vd} respectively. Therefore, identification based on the ULS technique gives all the parameters engaged in rigid body modeling and there is no need to conduct a separate experiments to find Coulomb friction parameters. The equivalent inertia and viscous damping coefficient can be obtained by using equations below:

$$J_e = \frac{(Q_{vd} - 1)k_t k_a T_s}{P_{vd} \ln(Q_{vd})} \quad (4.18)$$

$$B_e = \frac{(1 - Q_{vd})k_t k_a}{P_{vd}} \quad (4.19)$$

To identify the parameters, Erkorkmaz suggested a pulse-shaped voltage command (Figure 4.1) to be commanded to the amplifier in open-loop while having the servo drive in torque control mode. The amplitude of the supplied voltage must be scaled with different factors, k_u , to provide sufficient excitation to overcome static friction and the parameters should be estimated for each k_u . Here care must be taken in selecting k_u to avoid saturation of the amplifier. The estimated parameters (J_e and B_e) for the largest value of k_u , which does not saturate the drives, must be considered as the identified parameters.

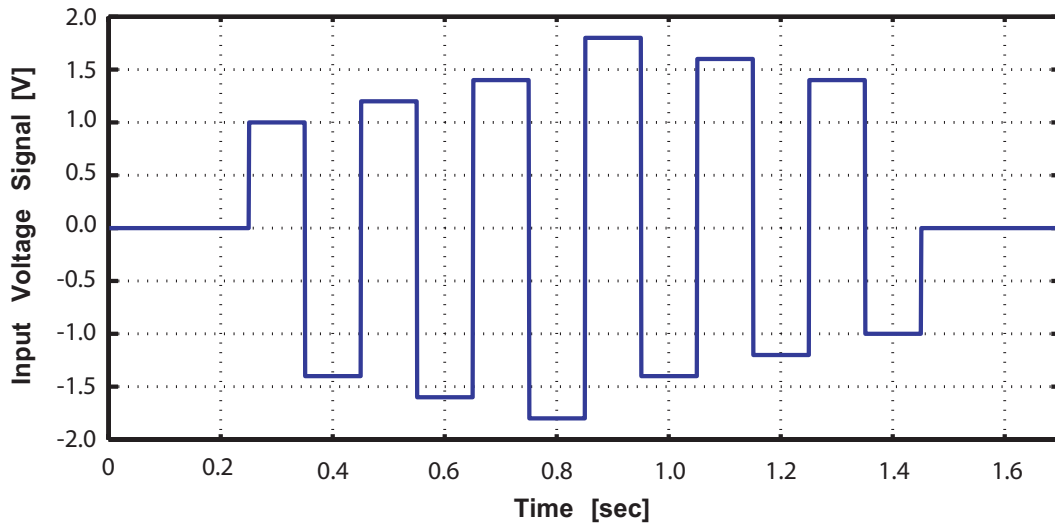


Figure 4.1: Least square identification reference command

4.3 Identification of Structural Flexibilities

The structural dynamics of the drive in the machine tool with structural flexibilities ($G_f(s)$) is identified by sending sweep sinusoidal waves to the amplifier at a frequency range of modes. The frequency response function (FRF) of the system is measured with a Fourier analyzer. The measured FRF ($G_e(s = j\omega)$) is divided by rigid body dynamics ($G_r(j\omega)$) at each frequency to isolate the structural dynamics ($G_f(s = j\omega)$). If the linear encoder resolution is not high, the low frequency modes with large masses cannot be measured accurately. In such cases, one accelerometer is placed at the bed where the encoder reading head is mounted, and another is placed on the table while exciting the motor. The FRFs from the two locations are subtracted and divided by $(j\omega)^2$ to find $\left(G_e(j\omega) = \frac{x_t(j\omega) - x_{be}(j\omega)}{T_m(j\omega)}\right)$, which is equivalent to linear encoder based measurements. For the machine tool with column and ball-screw flexibility (see section 3.3.3), the numerator of the transfer function (Equation (3.34)) is reorganized as the product of second order polynomials to suit the identification algorithm:

$$G_f(s) = K_f \frac{\prod_{i=1}^3 (s^2 + a_i s + b_i)}{\prod_{i=1}^3 (s^2 + 2\zeta_i \omega_{ni} s + \omega_{ni}^2)} \quad (4.20)$$

in which four parameters need to be identified ($a_i, b_i, \zeta_i, \omega_{ni}$) for each mode. The natural frequency (ω_{ni}) and damping ratio (ζ_i) are estimated from experimental FRFs either using Peak Picking (PP) algorithm [50] for well-separated modes, or Rational Fraction Polynomials (RFP) method [51] for closely spaced modes. These two algorithms are explained in section 4.4. Having damping ratios and natural frequencies identified, the denominator of $G_f(s)$ is known; and only the numerator coefficients are left as unknowns. Replacing s with $(j\omega)$ in Equation (4.20), magnitude of $G_f(s)$ becomes:

$$|G_f(j\omega)| = K_f \sqrt{\frac{\prod_{i=1}^k ((b_i - \omega^2)^2 + a_i^2)}{\prod_{i=1}^k ((\omega_{ni}^2 - \omega^2)^2 + (2\zeta_i \omega_{ni} \omega)^2)}} \quad (4.21)$$

where the unknowns are stored in a parameter vector as:

$$\{\beta\} = [K_f, a_1, a_2, a_3, b_1, b_2, b_3]^T \quad (4.22)$$

The parameters are estimated using non-linear least squares method. Starting with an initial guess, β^0 , Gauss-Newton iteration is used to identify the unknown parameters:

$$\{\beta\}^{s+1} = \{\beta\}^s - \left([\mathbf{J}_f]^T [\mathbf{J}_f] \right)^{-1} [\mathbf{J}_f]^T f(\beta^s) \quad (4.23)$$

where the Jacobin matrix (J_f) is:

$$[\mathbf{J}_f] = \begin{bmatrix} \frac{\partial f}{\partial K_f} & \frac{\partial f}{\partial a_1} & \frac{\partial f}{\partial a_2} & \frac{\partial f}{\partial a_3} & \frac{\partial f}{\partial b_1} & \frac{\partial f}{\partial b_2} & \frac{\partial f}{\partial b_3} \end{bmatrix} \quad (4.24)$$

with the partial derivative terms:

$$\frac{\partial f}{\partial K_f} = \sqrt{\frac{\prod_{i=1}^k \left((b_i - \omega^2)^2 + a_i^2 \right)}{\prod_{i=1}^k \left((\omega_{ni}^2 - \omega^2)^2 + (2\zeta_i \omega_{ni} \omega)^2 \right)}} \quad (4.25)$$

$$\frac{\partial f}{\partial a_j} = \sqrt{\frac{\prod_{i=1, i \neq j}^k \left((b_i - \omega^2)^2 + a_i^2 \right)}{\prod_{i=1}^k \left((\omega_{ni}^2 - \omega^2)^2 + (2\zeta_i \omega_{ni} \omega)^2 \right)}} \times \frac{a_j}{\sqrt{\left((b_j - \omega^2)^2 + a_j^2 \right)}} \quad (4.26)$$

$$\frac{\partial f}{\partial b_j} = \sqrt{\frac{\prod_{i=1, i \neq j}^k \left((b_i - \omega^2)^2 + a_i^2 \right)}{\prod_{i=1}^k \left((\omega_{ni}^2 - \omega^2)^2 + (2\zeta_i \omega_{ni} \omega)^2 \right)}} \times \frac{(b_j - \omega^2)}{\sqrt{\left((b_j - \omega^2)^2 + a_j^2 \right)}} \quad (4.27)$$

In non-linear least squares problems, when dealing with a large number of unknowns, the iteration convergence highly depends on an appropriate initial guess of the unknowns. To facilitate reconstruction of experimental FRF and find the appropriate initial guess, curve fitting is done in several steps. In the first step ($m = 1$), iterations start with considering only the first

mode and neglecting higher modes dynamics. As $G_f(s)$ must have DC gain of 1, the unknown parameters are initialized as:

$$K_f^1 = 1; a_1^1 = 0; b_1^1 = (\omega_{n1})^2 \quad (4.28)$$

where the superscript indicates the step number ($m = 1$). Outputs of the first step are stored in K_f^1 , a_1^1 , and b_1^1 and they are used as the initial guess in the second step ($m = 2$) where dynamics of the second mode are taken into account. Therefore, the initial guesses for the parameters to be identified in the second step are made as:

$$K_f^2 = K_f^1; a_1^2 = a_1^1; b_1^2 = b_1^1 \quad (4.29)$$

$$a_2^2 = 0; b_2^2 = \frac{(\omega_{n1} \omega_{n2})^2}{K_f^1 b_1^2} \quad (4.30)$$

A similar procedure is followed in the third step ($m = 3$) as:

$$K_f^3 = K_f^2; a_1^3 = a_1^2; b_1^3 = b_1^2; a_2^3 = a_2^2; b_2^3 = b_2^2 \quad (4.31)$$

$$a_3^3 = 0; b_3^3 = \frac{(\omega_{n1} \omega_{n2} \omega_{n3})^2}{K_f^2 b_1^3 b_2^3} \quad (4.32)$$

The flowchart shown in Figure 4.2 summarizes the steps for the identification of $G_f(s)$.

4.4 Modal Parameters (ζ, ω_n) Estimation

The existing literature for modal parameter estimation is rich and a wide range of approaches in time domain and frequency domain has been developed. In this section, the Peak-Picking (PP) algorithm and Rational Fraction Polynomial (RFP) approach are briefly explained.

4.4. Modal Parameters (ζ, ω_n) Estimation

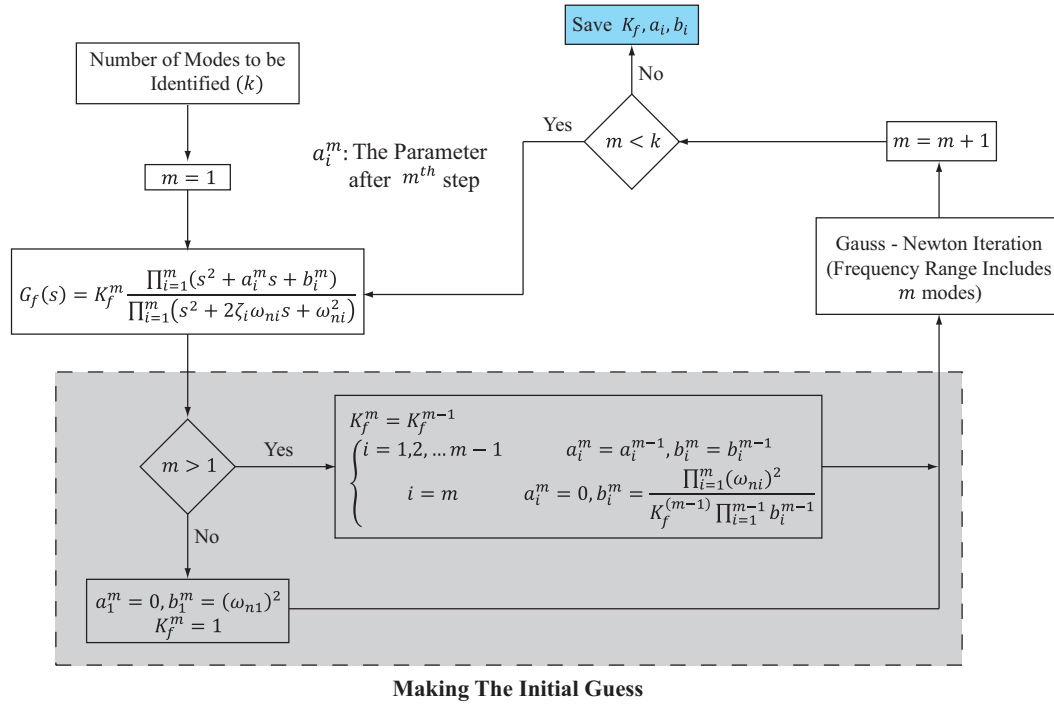


Figure 4.2: Identification of G_f Flowchart

4.4.1 The Peak Picking Method

For a single degree of freedom mass-spring and damper system (Figure 4.3) with mass of m , stiffness of k , and damping coefficient of c , the transfer function between applied force to the mass and its vibration response has the following structure:

$$G(s) = \frac{x_s}{F_s} = \frac{\omega_n^2/k}{s^2 + 2\zeta\omega_n s + \omega_n^2}; \text{ Where } \zeta = \frac{c}{2\sqrt{km}}, \omega_n = \sqrt{\frac{k}{m}} \quad (4.33)$$

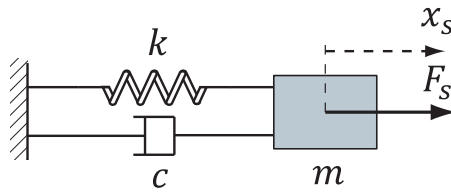


Figure 4.3: Single degree of freedom oscillator (Mass, Spring, and Damper System)

4.4. Modal Parameters (ζ, ω_n) Estimation

The frequency response function of the single degree of freedom oscillator can be obtained by replacing the Laplace operator (s) with ($j\omega$) in Equation (4.33) as:

$$G(j\omega) = \frac{\omega_n^2/k}{(\omega_n^2 - \omega^2) + j(2\zeta\omega_n\omega)} \quad (4.34)$$

The real and imaginary parts of Equation (4.34) are extracted through multiplying its numerator and denominator by $(\omega_n^2 - \omega^2) - j(2\zeta\omega_n\omega)$:

$$Re[G(j\omega)] = \frac{\omega_n^2(\omega_n^2 - \omega^2)/k}{(\omega_n^2 - \omega^2)^2 + (2\zeta\omega_n\omega)^2} \quad (4.35)$$

$$Im[G(j\omega)] = \frac{\omega_n^2(2\zeta\omega_n\omega)/k}{(\omega_n^2 - \omega^2)^2 + (2\zeta\omega_n\omega)^2} \quad (4.36)$$

FRF plot of the single degree of freedom oscillator in terms of its real and imaginary parts is depicted in Figure 4.4.

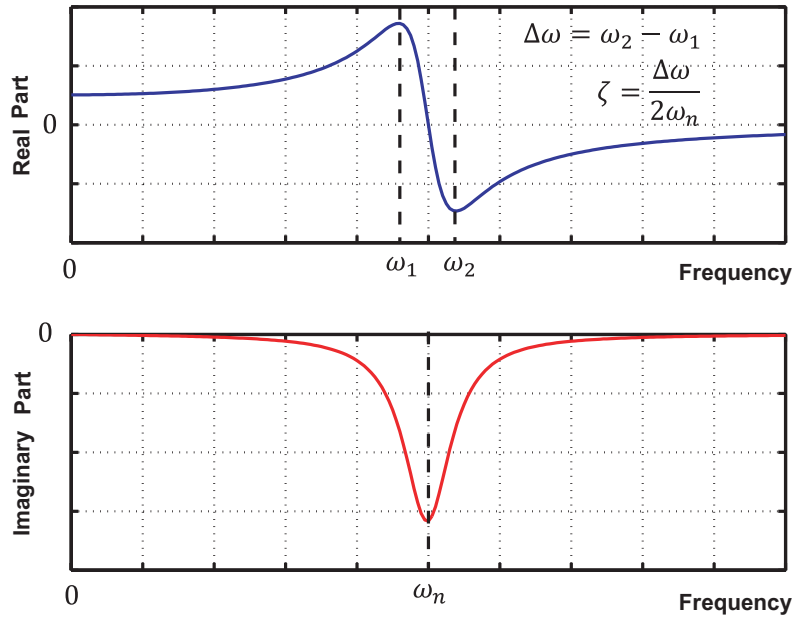


Figure 4.4: Transfer function of a SDOF system represented by its real and imaginary parts

As this Figure 4.4 indicates, the real part shows two extremums at the frequencies of $(\omega_1 = \omega_n(1 - \zeta))$ and $(\omega_2 = \omega_n(1 + \zeta))$; the imaginary plot has a peak at the natural frequency (ω_n) . As a result, for a single degree of freedom oscillator, it is possible to identify its natural frequency (ω_n) and damping ratio (ζ) by reading the frequencies associated with the extremums of real and imaginary plots of its experimental FRF and using the following equation.

$$\zeta = \frac{\Delta\omega}{2\omega_n}; \Delta\omega = \omega_2 - \omega_1 \quad (4.37)$$

The explained procedure is called *Peak Picking* approach to identify modal parameters of a flexible system. This is the simplest method for identifying the modal parameters of a flexible structure in frequency domain. It is also quite efficient for flexible systems with well-separated modes where dynamics of one mode is not affected with dynamics of the neighboring mode. More details on this approach are presented in [52].

4.4.2 The Rational Fraction Polynomial (RFP) Method

When two modes are closely spaced, each of the modes affects the neighboring mode frequency response; this interference makes modal parameter estimation more difficult. Therefore, when the flexible system exhibits closely spaced modes, more advanced methods must be utilized for more accurate estimation of modal parameters.

A plenty of studies are published in literature to define a numerical indicator for modal interference [53, 54]. Modal Overlap Factor (μ) is referred to the ratio between the half-power modal bandwidth and the average modal spacing [54]. Considering Figure 4.5, for two closely spaced modes, the modal overlap factor for each mode (μ_i) is defined as:

$$\mu_i = \frac{\Delta f_i}{\Delta F} \quad (4.38)$$

When μ is larger than 30%, modes are coupled and accurate estimation of modal parameters requires more advanced identification techniques than Peak-Picking algorithm, such as Rational Fraction Polynomials (RFP).

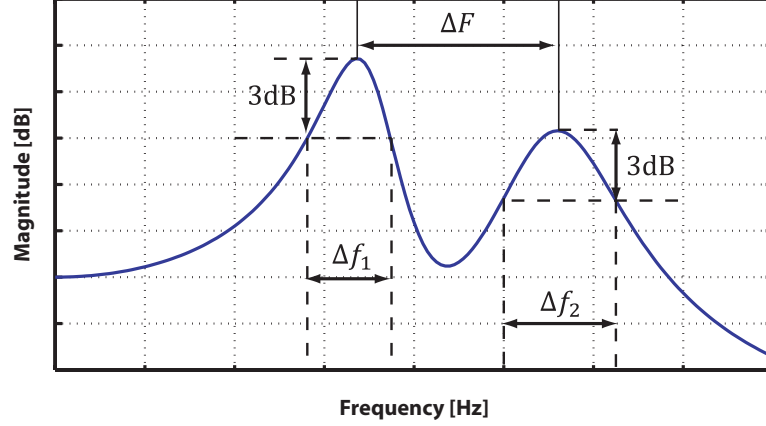


Figure 4.5: Magnitude plot of frequency response function for a system with two closely spaced modes

Rational fraction form denotes a fraction which has two polynomials in its numerator and denominator, and the order of denominator (n) is independent of the order of numerator (m) (see Equation (4.39)). The polynomial in denominator is called characteristic equation, and its roots represent poles of the system.

$$H(j\omega) = \frac{\sum_{k=0}^m a_k s^k}{\sum_{k=0}^n b_k s^k}; s = j\omega \quad (4.39)$$

The main effort is finding coefficients of the numerator (a_k) and denominator (b_k) such that the reconstructed FRF ($\frac{\sum_{k=0}^m a_k s^k}{\sum_{k=0}^n b_k s^k}$) makes a good fit with the experimentally measured FRF ($H(j\omega)$). The curve fitting problem can be expressed as minimizing the error criterion (J) defined as follows:

$$e_i = \sum_{k=0}^m a_k s_i^k - \underbrace{H(j\omega_i)}_{h_i} \sum_{k=0}^n b_k s_i^k; s_i = j\omega_i \quad (4.40)$$

$$J = \sum_{i=1}^L e_i^2 \quad (4.41)$$

The polynomials in numerator and denominator of Equation 4.39, and therefore the experimental FRF ($H(j\omega)$) have Hermitian symmetry about the origin of the frequency axis. In other words, their real part are even functions and their imaginary part are odd functions. As Richardson and Formenti [51] proposed, Equations 4.39 and 4.40 can be expressed in terms of orthogonal polynomials ($\phi_{i,j}$ and $\theta_{i,j}$) as:

$$H(j\omega) = \frac{\sum_{k=0}^m c_k \phi_{i,k}}{\sum_{k=0}^n d_k \theta_{i,k}}; d_n = 1 \quad (4.42)$$

$$e_i = \sum_{k=0}^m c_k \phi_{i,k} - h_i \sum_{k=0}^n d_k \theta_{i,k} \quad (4.43)$$

where the orthogonality condition is defined as:

$$\sum_{i=-L}^L \phi_{i,k} \phi_{i,j} = \begin{cases} 0 & k \neq j \\ 1 & k = j \end{cases} \quad \text{and} \quad \sum_{i=-L}^L \theta_{i,k} |h_i|^2 \theta_{i,j} = \begin{cases} 0 & k \neq j \\ 1 & k = j \end{cases} \quad (4.44)$$

L indicates the number of frequencies in which the experimental FRF ($H(j\omega_i)$) is measured. For negative frequencies ($i = -L, \dots, -1$) the experimental FRF (h_i) is constructed by using its Hermitian symmetry property. Equation 4.43 can be expressed in matrix form as:

$$\{E\} = [P] \{C\} - [T] \{D\} - \{W\} \quad (4.45)$$

where

$$\{E\} = \begin{bmatrix} e_{-L} \\ \vdots \\ e_L \end{bmatrix}; [P] = \begin{bmatrix} \phi_{-L,0} & \phi_{-L,1} & \cdots & \phi_{-L,m} \\ \vdots & \vdots & \ddots & \vdots \\ \phi_{L,0} & \phi_{L,1} & \cdots & \phi_{L,m} \end{bmatrix} \quad (4.46)$$

$$[T] = \begin{bmatrix} h_{-L}\theta_{-L,0} & h_{-L}\theta_{-L,1} & \cdots & h_{-L}\theta_{-L,n-1} \\ \vdots & \vdots & \ddots & \vdots \\ h_L\theta_{L,0} & h_L\theta_{L,1} & \cdots & h_L\theta_{L,n-1} \end{bmatrix}, \{W\} = \begin{bmatrix} h_{-L}\theta_{-L,n} \\ \vdots \\ h_L\theta_{L,n} \end{bmatrix} \quad (4.47)$$

$$\{C\} = \begin{bmatrix} c_0 & c_1 & \cdots & c_m \end{bmatrix}^T, \{D\} = \begin{bmatrix} d_0 & d_1 & \cdots & d_{n-1} \end{bmatrix}^T \quad (4.48)$$

This new formulation overcomes some numerical analysis problems from which the old least squares techniques suffer. The procedure of calculating the orthogonal polynomials at each frequency ($\phi_{i,j}$ and $\theta_{i,j}$) is presented in Appendix B. The numerator and denominator coefficients (c_k and d_k) of the transfer function expressed in terms of orthogonal polynomials (see Equation 4.42) are obtained through least square minimization of the error vector ($\{E\}$) as:

$$\begin{cases} \{D\} = -[I - [X]^T [X]]^{-1} [X]^T \{H\} \\ \{C\} = \{H\} - [X] \{D\} \end{cases} \quad (4.49)$$

where

$$[X] = -\text{Re}([P^*]^T [T]) \{H\} = \text{Re}([P^*]^T \{W\}) \quad (4.50)$$

The star sign (*) indicates the complex conjugate matrix. Once these coefficients are known, the coefficients of the denominator of the transfer function in terms of Laplace variable (b_k in Equation 4.39) can easily be recovered as:

$$b_k = \sum_{i=k}^n d_i p_k^i; p_k^i = \begin{cases} 0 & k < 0 \text{ or } k > i \\ \frac{1}{D_0} & i = k = 0 \\ \frac{1}{D_i} p_{k-1}^{i-1} + V_{i-1} p_k^{i-2} & 0 \leq k \leq i \end{cases} \quad (4.51)$$

The proof of Equation 4.51 is presented in Appendix B. Having these coefficients, it is possible to reconstruct the characteristic equation in its ordinary form. Damping ratio (ζ) and natural

frequency (ω_n) of a specific mode which is considered in curve fitting can be calculated from the roots of the identified characteristic equation. Besides modal analysis, this technique can be utilized for identification of poles, zeros and resonances of combined electromechanical servo-systems.

4.5 Experimental Identification Results

Considering the mathematical models developed in sections 3.3.2 and 3.3.3, the experimental results of the identified transfer functions for the ball-screw test bed and the flexible machine tool (FADAL VMC2216) are presented in sections 4.5.1 and 4.5.2, respectively.

4.5.1 Ball-Screw Test Bed

The amplifier gain (k_a), motor torque constant (k_t), and ball-screw pitch length (h_p) for the ball-screw test bed are given in manufacturer's catalogue as:

$$k_a = 0.887 \left[\frac{A}{V} \right]; k_t = 0.72 \left[\frac{N.m}{A} \right]; h_p = 20 [mm] \quad (4.52)$$

From Equation (3.1), the nut transformation ratio (r_g) is:

$$r_g = \frac{h_p}{2\pi} = \frac{20 \times 10^{-3} [m]}{2\pi [rad]} = 0.0032 \left[\frac{m}{rad} \right] \quad (4.53)$$

The estimated inertia (J_e) and viscous damping coefficient (B_e) for different gain values (k_u) are presented in Figure 4.6. For small values of k_u , the motor does not provide enough power to overcome sticking friction in the guide-way; hence, the identification procedure overestimates the parameters of interest. By increasing k_u , the given voltage to servo drive increases and a higher torque is applied at the ball-screw. Therefore, machine table moves with a higher

4.5. Experimental Identification Results

velocity; a more rapid motion of the table mitigates the effect of nonlinear friction around zero velocity on parameter identification.

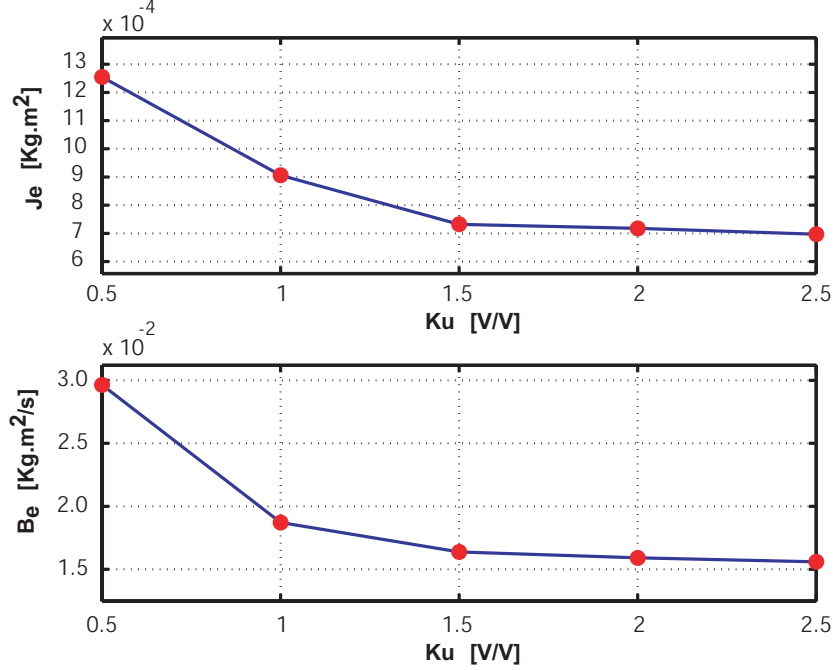


Figure 4.6: Estimated inertia (J_e) and viscous damping coefficient (B_e) by unbiased least squares technique

According to manufacturer's catalogue, the saturation limit for the amplifier is 5 [V]; hence, k_u cannot be larger than $2.5 \left[\frac{\text{V}}{\text{V}} \right]$. The estimated parameters for $k_u = 2.5$ are considered as the identified inertia and viscous damping coefficients reflected on the motor shaft as:

$$J_e = 6.9703 \times 10^{-4} [\text{Kg.m}^2]; B_e = 0.0156 [\text{kg.m}^2/\text{s}] \quad (4.54)$$

Considering Equation (3.4), the rigid body transfer function between motor torque (T_m) and machine table displacement (x_t) can be obtained as:

$$G_r \left[\frac{\text{m}}{\text{N.m}} \right] = \frac{r_g}{s(J_e s + B_e)} = \frac{0.0032}{s(6.9703 \times 10^{-3} s + 0.0156)} \quad (4.55)$$

4.5. Experimental Identification Results

To identify the contribution of structural dynamics (G_{ft} and G_{fm} in Equation (3.13)) in table vibration (x_t), the experimental FRFs between motor torque (T_m) and machine table displacement measured through linear and rotary encoders are reconstructed by curve fitting. The experimental FRFs are obtained through sweeping sinusoidal voltage commands from 10 - 300 [Hz]. Table position is measured directly by using the linear encoder. The rotary encoder gives table position based on angular displacement of the ball-screw at motor shaft (θ_m); therefore, it outputs $r_g \theta_m$. Experimental FRFs and bode plot of the rigid body transfer function ($k_a k_t G_r(j\omega)$) are depicted in Figure 4.7.

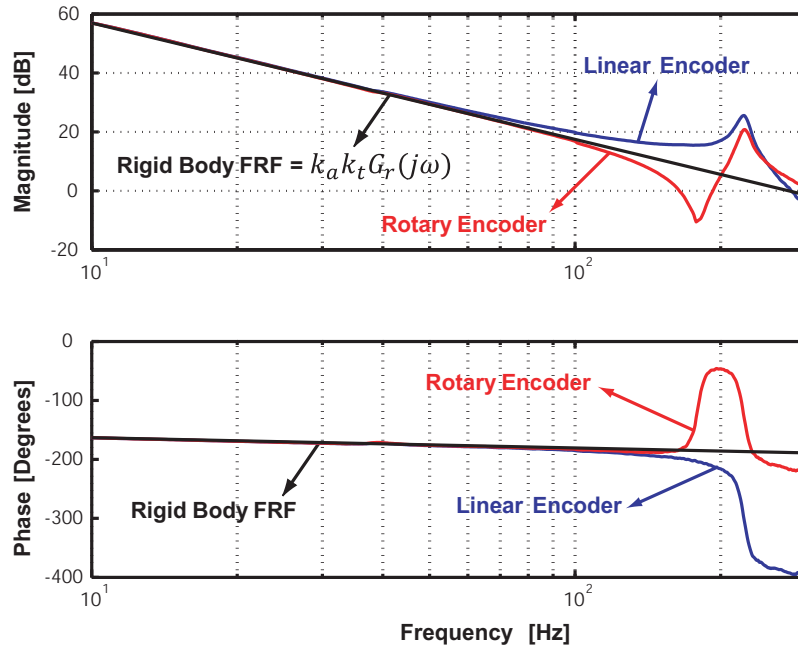


Figure 4.7: The experimental FRF between motor torque and table displacement measured by linear and rotary encoders

Figure 4.7 shows that the ball-screw drive has a torsional mode around 220 [Hz] which is clearly captured by linear and rotary encoders. The rigid body transfer function FRF coincides with the experimental FRF in low frequency region (1-100 [Hz]). This means that, in low frequency region, the rigid body transfer function can successfully explain ball-screw dynamics.

4.5. Experimental Identification Results

Figure 4.8 presents the contribution of ball-screw flexibility (G_{ft} and G_{fm}) in linear scale obtained through dividing experimental FRF by rigid body FRF at each frequency in the range of 10-300 [Hz]. From the flexible ball-screw modeling in section (3.3.2), the governing equations for G_{ft} and G_{fm} have the following structure:

$$G_{ft}(s) \left[\frac{m}{m} \right] = \frac{(\alpha_t s + \beta_t)}{(s^2 + 2\zeta \omega_n s + \omega_n^2)}; G_{fm}(s) \left[\frac{m}{m} \right] = K_{fm} \frac{(s^2 + \alpha_m s + \beta_m)}{(s^2 + 2\zeta \omega_n s + \omega_n^2)}$$

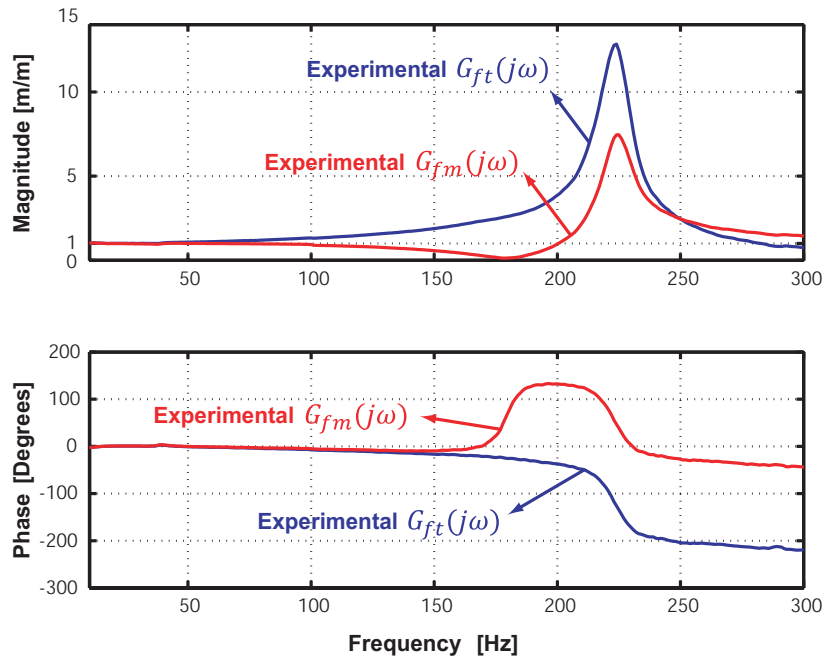


Figure 4.8: Contribution of the ball-screw torsional flexibility in the experimental FRFs measured by linear and rotary encoders

Because there is no other mode closely located to the ball-screw torsional mode, peak picking algorithm is used to identify the natural frequency (ω_n) and damping ratio (ζ) from real and imaginary plots of G_{ft} and G_{fm} shown in Figure 4.9. As explained in Section 4.4, the imaginary plot shows a peak at the natural frequency ($\omega_n = 223.91$ [Hz]). The damping ratio (ζ) is calculated as:

$$\zeta = \frac{\omega_2 - \omega_1}{2\omega_n} = \frac{229 - 212}{2 \times 223.91} = 0.038 \quad (4.56)$$

4.5. Experimental Identification Results

where ω_1 and ω_2 are shown in Figure 4.9.

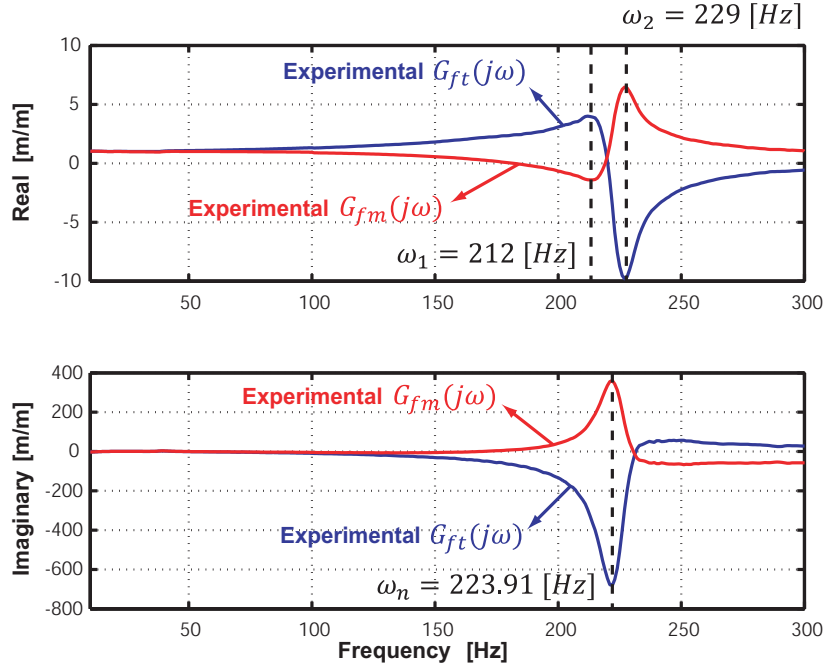


Figure 4.9: Real and imaginary plots of the experimental FRF for G_{ft} and G_{fm}

Considering Figure 4.7, the experimental FRF measured by the rotary encoder $G_m(j\omega)$ shows an anti-resonant mode around 180 [Hz]. This sharp attenuation in bode plot means that G_{fm} possesses imaginary zeros in its numerator. Therefore, the FRF obtained by dividing G_{ft} by G_{fm} at each frequency, which is shown in Figure 4.10, exhibits a mode around 180 [Hz] and has the following structure:

$$\frac{G_{ft}}{G_{fm}} = \frac{1}{K_{fm}} \frac{\alpha_t s + \beta_t}{s^2 + \alpha_m s + \beta_m} \quad (4.57)$$

Its modal parameters (ζ' and ω_n') are estimated by peak picking algorithm as:

$$\zeta' = 0.02574; \omega_n' = 180[\text{Hz}] \quad (4.58)$$

The denominator coefficients (α_m and β_m) in Equation (4.57), can be expressed in terms of

4.5. Experimental Identification Results

the identified modal parameters (ζ' and ω_n') as:

$$\beta_m = (\omega_n')^2 = 1.279 \times 10^6; \alpha_m = 2\zeta'\omega_n = 58.22 \quad (4.59)$$

According to Figure 4.8, G_{ft} and G_{fm} have a gain of 1 in low frequency region. Hence:

$$K_{fm}\beta_m = \omega_n^2 \implies K_{fm} = \frac{\omega_n^2}{\beta_m} = \frac{(223.91 \times 2 \times \pi)^2}{1.279 \times 10^6} = 1.5475 \quad (4.60)$$

$$\beta_t = \omega_n^2 = 1.979 \times 10^6 \quad (4.61)$$

The only unknown parameter is α_t . This parameter is identified by least squares minimization of the error in phase plot, between experimental and reconstructed FRF of $\frac{G_{ft}(j\omega)}{G_{fm}(j\omega)}$, shown in Figure 4.10, as:

$$\alpha_t = -53.952 \quad (4.62)$$

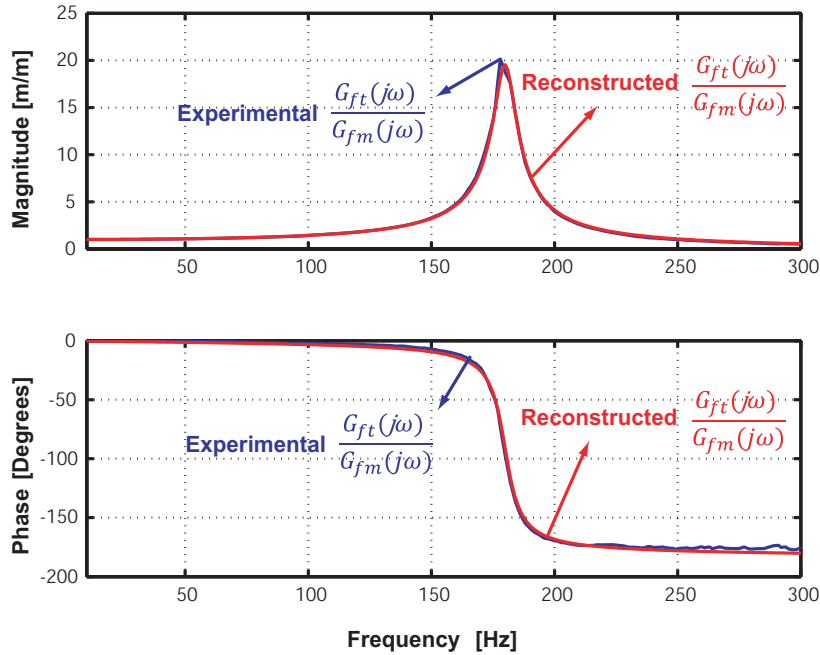


Figure 4.10: Magnitude and phase plot of experimental and reconstructed $\frac{G_{ft}(j\omega)}{G_{fm}(j\omega)}$

4.5. Experimental Identification Results

The identified parameters are summarized in Table 4.1.

Table 4.1: Identified parameters of the flexible ball-screw drive

$J_e = 6.9703 \times 10^{-4} [kg.m^2]$	$B_e = 0.0156 \left[\frac{kg.m^2}{s} \right]$	$r_g = 0.0032 \left[\frac{m}{rad} \right]$
$k_a = 0.887 \left[\frac{A}{V} \right]$	$k_t = 0.72 \left[\frac{N.m}{A} \right]$	$K_{fm} = 1.5475$
$\zeta = 0.038$	$\omega_n = 1406.9 \left[\frac{rad}{s} \right]$	$\alpha_t = -53.952$
$\alpha_m = 58.22$	$\beta_t = 1.979 \times 10^6$	$\beta_m = 1.279 \times 10^6$

The identified transfer functions between motor torque (T_m) and table displacement (x_t) measured by linear and rotary ($r_g \theta_m$) encoders are:

$$G_t = \frac{x_t(s)}{T_m(s)} = \frac{0.0032 (53.952s + 1.979 \times 10^6)}{s(6.9703 \times 10^{-4}s + 0.0156)(s^2 + 106.92s + 1.979 \times 10^6)} \quad (4.63)$$

$$G_m = \frac{r_g \theta_m(s)}{T_m(s)} = 1.5475 \times \frac{0.0032 (s^2 + 58.22s + 1.279 \times 10^6)}{s(6.9703 \times 10^{-4}s + 0.0156)(s^2 + 106.92s + 1.979 \times 10^6)} \quad (4.64)$$

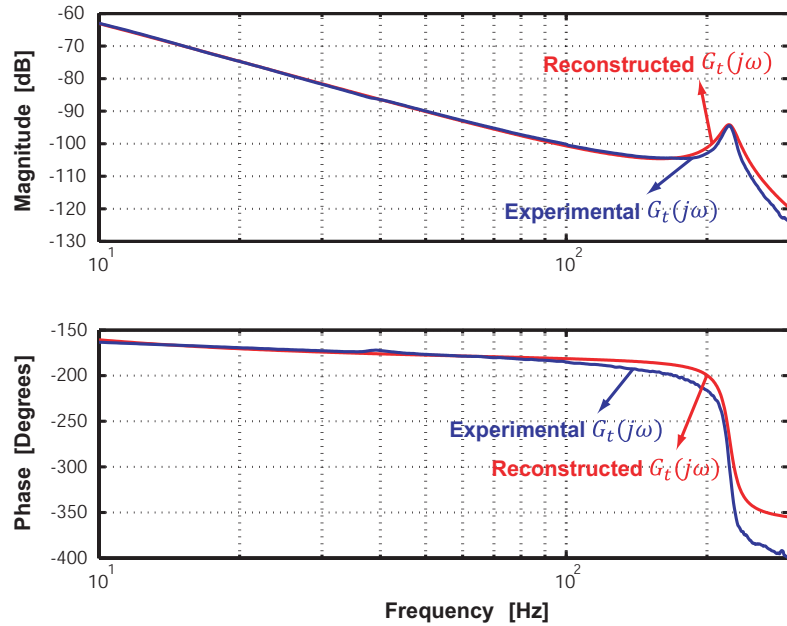


Figure 4.11: Experimental and reconstructed FRF of the transfer function between motor torque (T_m) and table position capture by linear encoder (x_t) (see Equation (4.63))

4.5. Experimental Identification Results

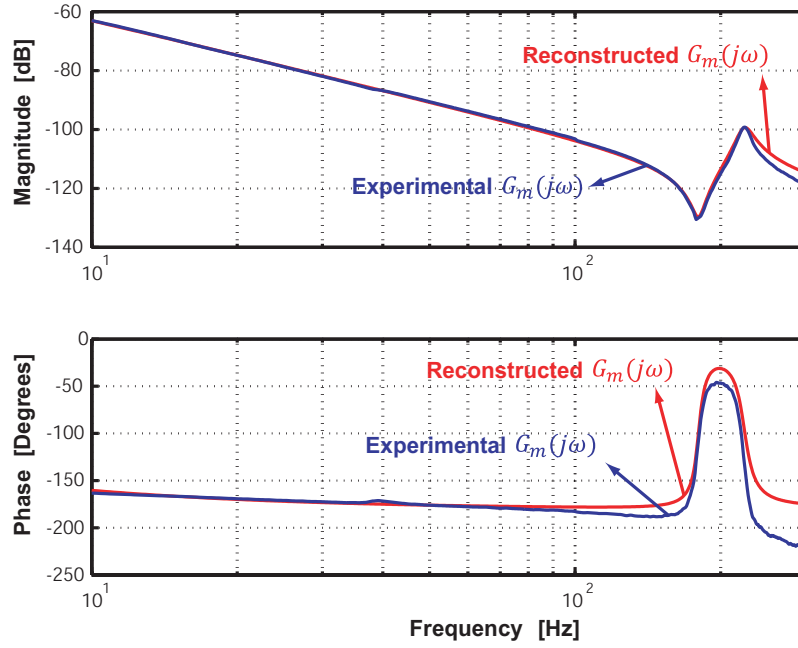


Figure 4.12: Experimental and reconstructed FRF of the transfer function between motor torque (T_m) and table position capture by rotary encoder ($r_g \theta_m$) (see Equation (4.64))

Bode plots of the identified transfer functions shown in Figures 4.11 and 4.12 provide a good fit with the experimentally measured FRFs in magnitude plot. The small discrepancy in the phase plot in high frequency region is due to the existence of non-linear friction in the ball-screw test bed which works as an additional damping. This additional damping changes the phase plot and increases the time delay. The effect of sticking friction is considerable in high frequency region where machine table vibration amplitude is less than 3 micro-meters. Moreover, FEM modeling of the ball-screw test bed [22] shows that, beside the torsional mode, the experimental setup exhibits lateral flexibilities which is not included in developing the mathematical model.

Direct FRF at the ball-screw table is also measured by using a hammer instrumented with a force sensor and mounting an accelerometer on the table. These FRFs are presented in Figure 4.13. When the small hammer (HA5 in Figure 4.14) with the aluminum tip is used, a shift in measured natural frequency and an overestimation of damping ratio is observed. This

4.5. Experimental Identification Results

discrepancy is due to non-linearities such as clearance in joints and nonlinear friction in the guide-way [55].

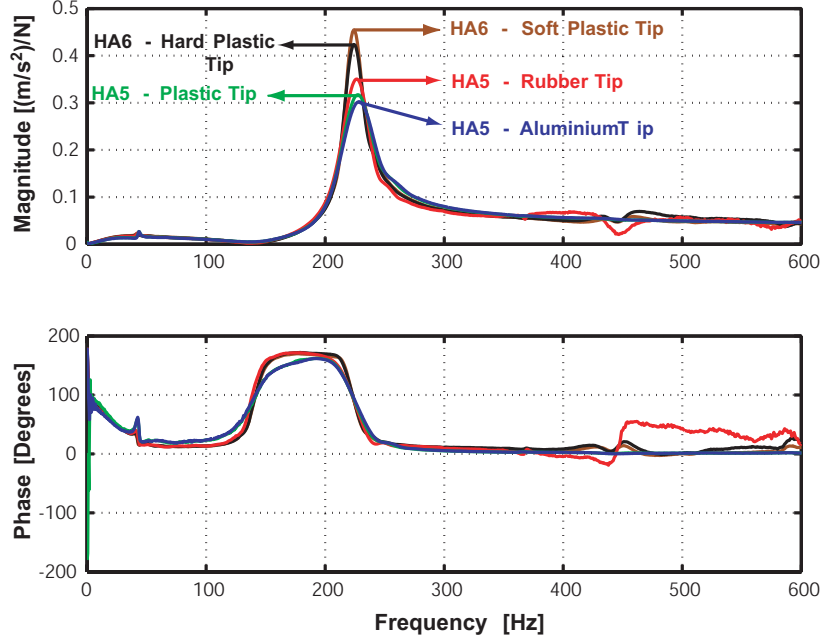


Figure 4.13: Direct FRFs measured at ball-screw table

Lampaert et al [56] studied the effect of nonlinear friction on frequency response function measurements. They concluded that the nonlinear friction in the pre-sliding region works as additional springs connected to the table which increase the stiffness and cause over estimation of the natural frequency. Halverson and Brown [55] emphasized on the effect of clearance and nonlinear damping in the joints on FRF measurements by impact testing. They pointed out that if excitation is close to a joint which has clearance, or the damping is a function of relative displacement, the apparent damping in the measured frequency response will be higher than the actual value as a result of large relative motion at that location. They also proposed pre-loading the system to take up clearances in joints and bearings.

Excitation of the structure with a larger force (harder hammer hit) removes the clearance instantly and breaks the pre-sliding friction bonds in the guide-way; therefore, a more in-

4.5. Experimental Identification Results

tense excitation of structure, which is possible by using softer tips, mitigates the effect of non-linearities (but does not remove them) and leads to a more accurate measurement of the natural frequency and damping ratio.

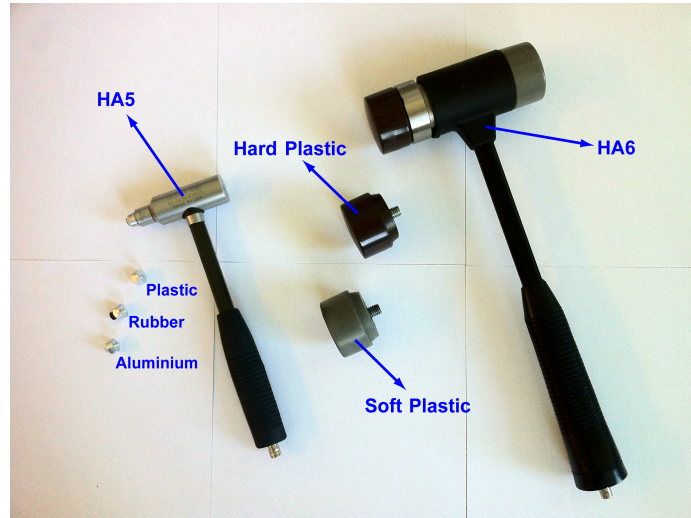


Figure 4.14: The hammers used for direct FRF measurements at ball-screw table

Figure 4.13 shows that by using softer tips (plastic and rubber) and a larger hammer (HA6) the measured natural frequency and damping ratio converge to those obtained by giving pure sinusoidal waves and using the FFT analyzer. In summary, systems which are an assembly of several components exhibit non-linearities due to the friction and clearance in joints and bearings; therefore, excitation of their structure with pure random (e.g white noise) or sine signal yields the most accurate analysis of their frequency response.

4.5.2 Flexible Machine Tool - FADAL VMC2216

The amplifier gain (k_a), motor torque constant (k_t), and ball-screw pitch length (h_p) for feed drive of the FADAL VMC 2216 for which the mathematical model is developed in Chapter 3, are given in manufacturer's catalogue as:

$$k_a = 0.4769 \left[\frac{A}{V} \right]; k_t = 6.5723 \left[\frac{N.m}{A} \right]; h_p = 10 [mm] \quad (4.65)$$

From Equation (3.1), the nut transformation ratio (r_g) is:

$$r_g = \frac{h_p}{2\pi} = \frac{10 \times 10^{-3} [m]}{2\pi} = 0.0016 \left[\frac{m}{rad} \right] \quad (4.66)$$

The equivalent inertia (J_e) and viscous damping coefficient (B_e) reflected on the motor shaft are identified as [3]:

$$J_e = 7.95 \times 10^{-3} [kg.m^2]; B_e = 0.0265 \left[\frac{kg.m^2}{s} \right] \quad (4.67)$$

Considering Equation (3.4), the rigid body transfer function between motor torque (T_m) and machine table displacement (x_t) can be obtained as:

$$G_r \left[\frac{m}{N.m} \right] = \frac{r_g}{s(J_e s + B_e)} = \frac{0.0016}{s(7.95 \times 10^{-3} s + 0.0265)} \quad (4.68)$$

Similar to the ball-screw test bed, the sine sweeping approach in the frequency range of 2-500 [Hz], is employed to measure the x -axis feed drive FRFs between supplied voltage (u) and the table position read by linear and rotary encoders. Experimental FRFs are depicted in Figure 4.15. The FRF measurements based on the linear encoder output indicates dominant modes at 49.01, 61.91, and 97.88 Hz which correspond to bending of the column, torsion of the column and axial mode of the ball screw, respectively. The modes are verified by analyzing

4.5. Experimental Identification Results

the mode shapes of the machine from experimental measurements and Finite Element study presented by Law et al in [57]. FRF measurements based on the rotary encoder output shows only one mode around 380 [Hz]; this mode is the torsional mode of ball-screw drive captured best by the rotary encoder. Its frequency is located far beyond the bandwidth of control loop (40-80 [Hz]); therefore this mode is not included in the mathematical modeling (see section 3.3.3) and identification.

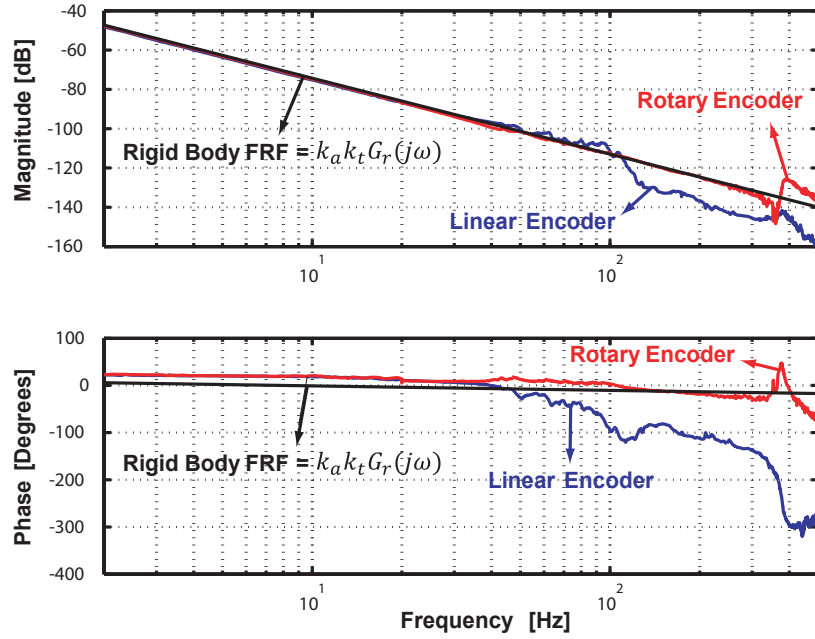


Figure 4.15: Experimental FRFs of the feed drive in x direction for FADAL VMC2216

In FRF measurement, an accelerometer is mounted on the table beside the encoders output. Figure 4.16 compares the measured acceleration FRFs in linear scale by using accelerometer and by taking double derivative of linear encoder output. This figure shows a discrepancy between obtained FRFs based on accelerometer and linear encoder measurements; the mode around 49 Hz is the most flexible one when accelerometer output is used to obtain acceleration FRF; however, the acceleration FRF based on linear encoder reveals that the mode around 97 [Hz] is the most flexible mode.

4.5. Experimental Identification Results

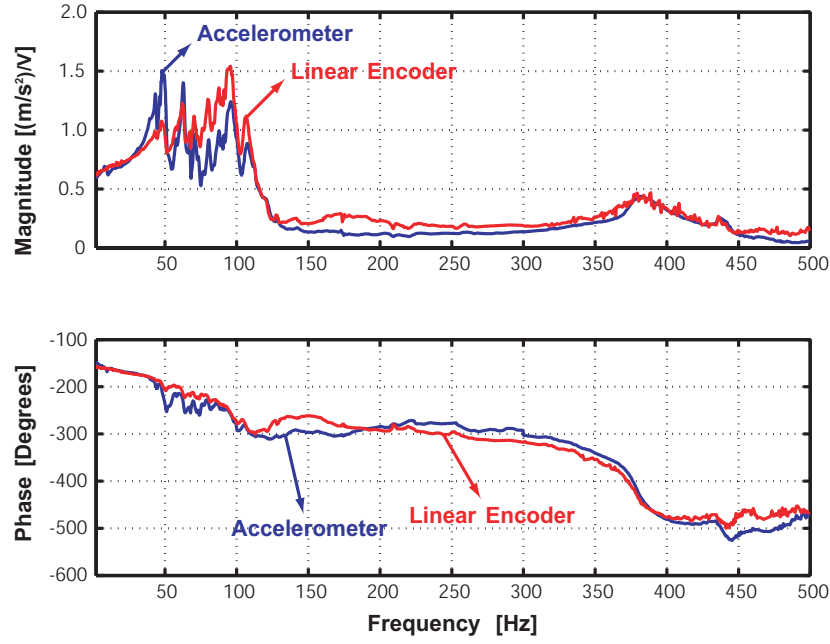


Figure 4.16: Comparison of the experimental FRF between table acceleration and input voltage to the amplifier measured by linear encoder (red line) and accelerometer (blue line)

As explained before, linear encoder outputs the relative displacement between machine table and bed. On the other hand, the accelerometer measures absolute acceleration of table in x direction. The mode shape at a specific frequency could be in a way which results in relative displacement of the machine table and bed to be different from linear displacement of machine table with respect to a stationary origin outside the machine. In such a case, we expect to see a discrepancy in measured FRFs. In the range of 30 to 60 [Hz], the machine table and bed move in the same direction since the vibrations are associated with the column bending and torsion modes; therefore, linear encoder output is less than absolute vibration of the table. Between 60 and 100 [Hz], vibrations are dominated by the axial mode of the ball-screw drive. Hence, the machine table and bed move in the opposite directions, leading the output of linear encoder to be larger than the table's absolute vibration amplitude. For further investigation, another experiment is conducted; the accelerometer (1) is attached to the bed where the optical head is placed and the accelerometer (2) is attached to the machine table where the scale is located. As

4.5. Experimental Identification Results

claimed before, subtracting the FRF obtained through the accelerometer (1) from that measured by the accelerometer (2) must lead to an FRF similar to that measured by using linear encoder. Figure 4.17 shows that this expectation is fulfilled and the obtained FRFs match.

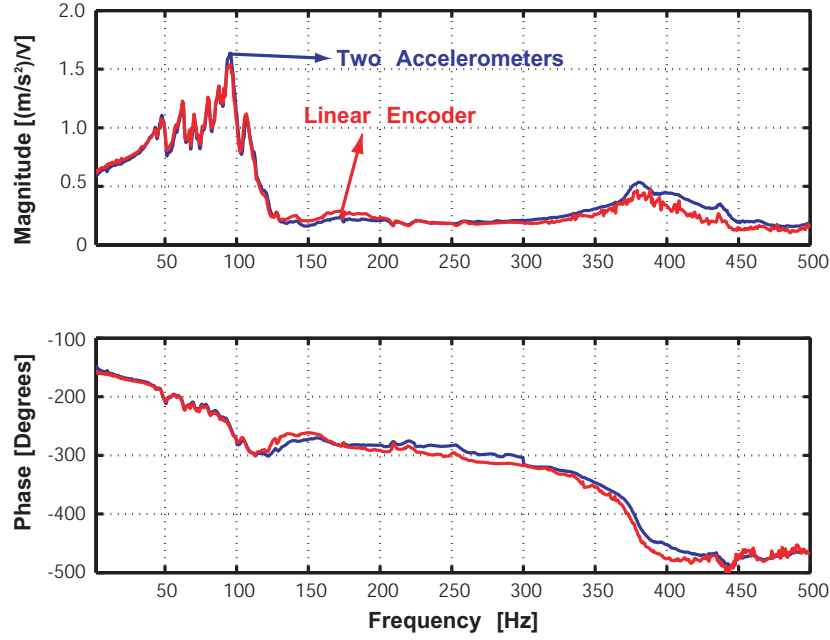


Figure 4.17: Experimental acceleration FRF - Comparison of using two accelerometers (blue line) and linear encoder (red line)

According to the mathematical modeling of the feed drive for machine tool with structural flexibilities presented in Section 3.3.3, the transfer function between motor torque (T_m) and table position measured by linear encoder (x) has the following structure:

$$G_e(s) = \frac{x(s)}{T_m(s)} = \underbrace{\frac{r_g}{s(J_e s + B_e)}}_{G_r(s)} \times K_f \underbrace{\frac{\prod_{i=1}^3 (s^2 + a_i s + b_i)}{\prod_{i=1}^3 (s^2 + 2\zeta_i \omega_{ni} s + \omega_{ni}^2)}}_{G_f(s)} \quad (4.69)$$

So far, the rigid body transfer function ($G_r(s)$) is identified. The total FRF is divided by rigid body dynamics ($G_r(j\omega)$) at the frequency domain to obtain the FRF of the structural dynamics ($G_f(j\omega)$).

4.5. Experimental Identification Results

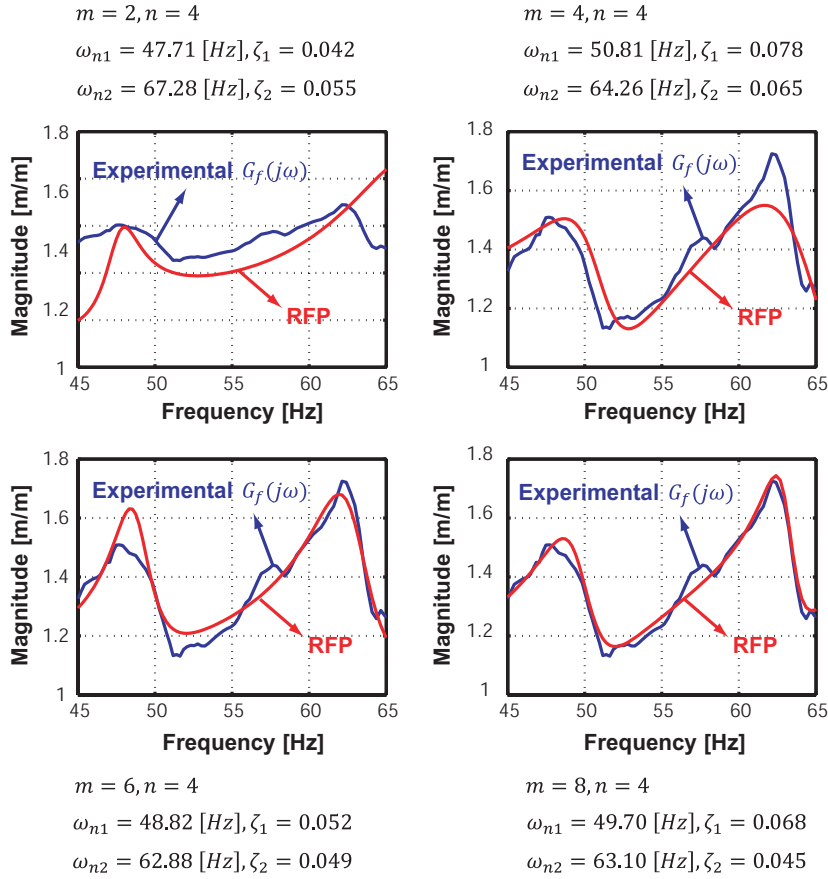


Figure 4.18: Estimation of modal parameter with RFP method for the closely spaced column bending and torsion modes.

The contribution of structural dynamics ($G_f(s)$) is estimated by implementing the identification algorithm presented in Section 4.3. Experimentally measured FRF exhibits three dominant modes in the frequency range of 2-150 [Hz]. These three modes are at 49, 61, and 97 [Hz] and correspond to bending of the column, torsion of the column and axial mode of the ball screw, respectively. They are considered in the modeling procedure in Section 3.3.3.

Because the first two modes are closely-spaced, Peak-Picking method fails to estimate their modal parameters properly and Rational Fraction Polynomial (RFP) approach is utilized (Figure 4.18). For this purpose, in *RFP modal parameter estimation* over the frequency range of (45-65 [Hz]), a 4th order polynomial is chosen for the denominator ($n = 4$) to include the

4.5. Experimental Identification Results

dynamics of column bending and torsion modes. As proposed by Richardson and Formenti [51], the order of numerator is increased in 4 steps to provide a more accurate estimation of natural frequencies and damping ratios. As Figure 4.18 shows, by increasing the order of numerator (m), the RFP technique compensates the effect of non-modeled dynamics and provides a better fit. The axial mode of the ball-screw is relatively far from the first two modes and its modal parameters are estimated by Peak-Picking algorithm (similar to the flexible ball-screw drive) as $\zeta_3 = 0.1$ and $\omega_{n3} = 96.84$ [Hz].

Having the modal parameters estimated, the denominator of $G_f(s)$ is known. To identify the unknown coefficients of its numerator, the nonlinear curve fitting approach shown in Figure 4.2 is followed. The estimated modal parameters from RFP and Peak-Picking techniques are fine-tuned in each step to improve the fitting accuracy.

The identified transfer function parameters from linear encoder (position) and servo command measurements are given in Table 4.2.

Table 4.2: Identified parameters of structural transfer function of the feed drive ($G_f(s)$ [m/m], see Equation (4.69)).

$K_f = 0.492$			
$a_1 = 60.65$	$b_1 = 105.62 \times 10^3$	$\zeta_1 = 0.083$	$\omega_{n1} = 307.94$
$a_2 = 88.36$	$b_2 = 150.23 \times 10^3$	$\zeta_2 = 0.060$	$\omega_{n2} = 388.93$
$a_3 = 272.5$	$b_3 = 694.56 \times 10^3$	$\zeta_3 = 0.091$	$\omega_{n3} = 615$

Figure 4.19 compares the experimental and reconstructed FRF of $G_f(j\omega)$ over the frequency range of interest (2-150 [Hz]). The identified open loop FRF of the system which contains both rigid body ($G_r(s)$) and structural dynamics ($G_f(j\omega)$) are superimposed on the measured FRF in Figure 4.20. This figure indicates that the reconstructed FRF matches the experimental FRF in both magnitude and phase plots.

4.5. Experimental Identification Results

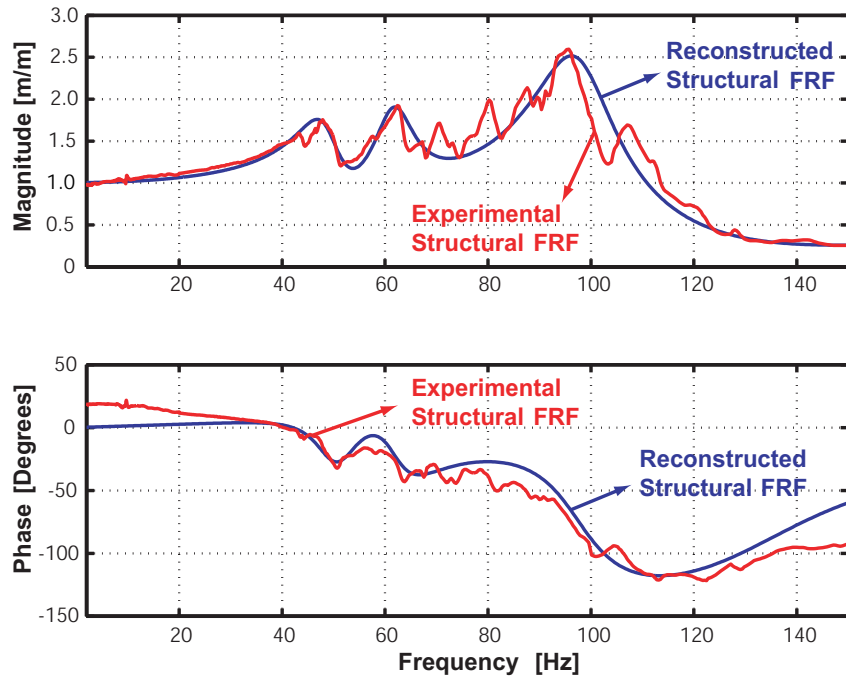


Figure 4.19: Experimental FRF of the feed drive structure ($G_f(s)$, see Equation (4.69)).

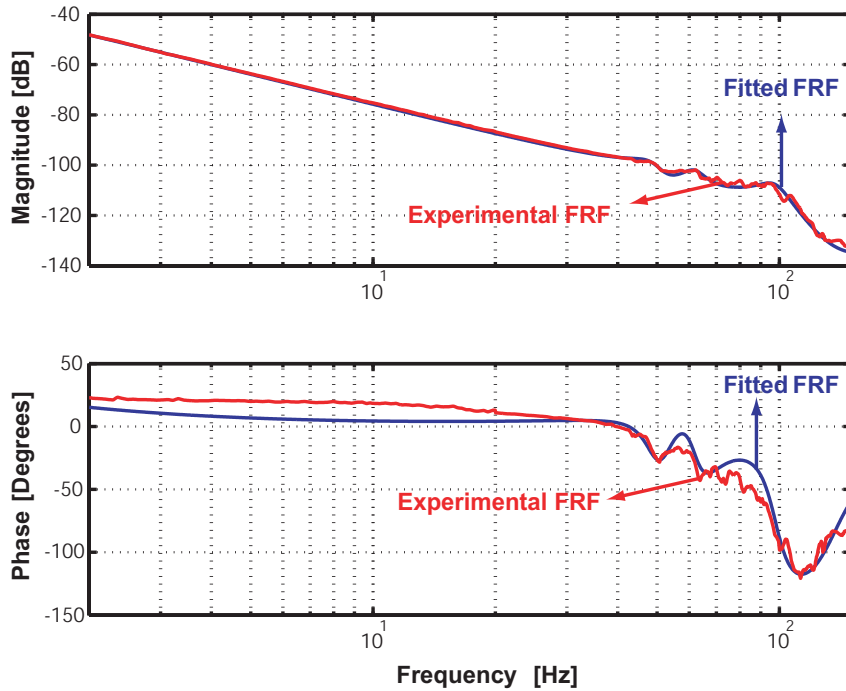


Figure 4.20: Experimental and reconstructed FRF of the open loop transfer function ($G_e(s)$, see Equation (4.69)).

4.6 Validation of the Identified Model for the Flexible Machine Tool

To validate the identified mathematical model for the flexible machine tool, its dynamics are simulated in control loop and the simulation and experimental results are compared. An Adaptive Sliding Mode Controller (ASMC) is implemented to control feed drive motion along a reference trajectory. The sliding mode controller is designed based on rigid body dynamics ($G_r(s)$ in Equation 4.68) and has the following structure [58]:

$$u_{smc} = K_s \sigma + m_e [\ddot{x}_r + \lambda (\dot{x}_r - \dot{x}_T)] + b_e \dot{x}_T + \hat{d} \quad (4.70)$$

$$m_e = \frac{J_e}{k_a k_t r_g}; b_e = \frac{B_e}{k_a k_t r_g}$$

$$\text{Sliding Surface: } \sigma = (\dot{x}_r - \dot{x}_T) + \lambda (x_r - x)$$

$$\text{Disturbance Observer: } \hat{d} = \rho \int_0^t \kappa \sigma dt$$

$$\kappa = \begin{cases} 0 & (\hat{d} < d^- \& \sigma < 0) \\ 0 & (\hat{d} > d^+ \& \sigma > 0) \\ 1 & \text{Otherwise} \end{cases}$$

In Equation 4.70, \dot{x}_T indicates the table velocity measured by the tachogenerator coupled to the motor shaft, x is the table position measured by the linear encoder and x_r represents the reference position commanded from the trajectory generation module in CNC. The nonlinear sliding mode controller is tuned to have a bandwidth of 30 [Hz] with parameters $\lambda = 200$ [rad/s], $k_s = 0.1$ [V/(mm/s)], $\rho = 30$ [V/mm]. The compensated disturbance is limited to voltage equivalent of $(d^-, d^+) = (-0.3, +0.3)$ [V]. The reflected mass and viscous damping coefficients are calculated from the identified rigid body parameters as $m_e = 1.5625$ and $b_e =$

5.3125, respectively. Figure 4.21 shows the block diagram of the servo loop used for the simulation and experiments.

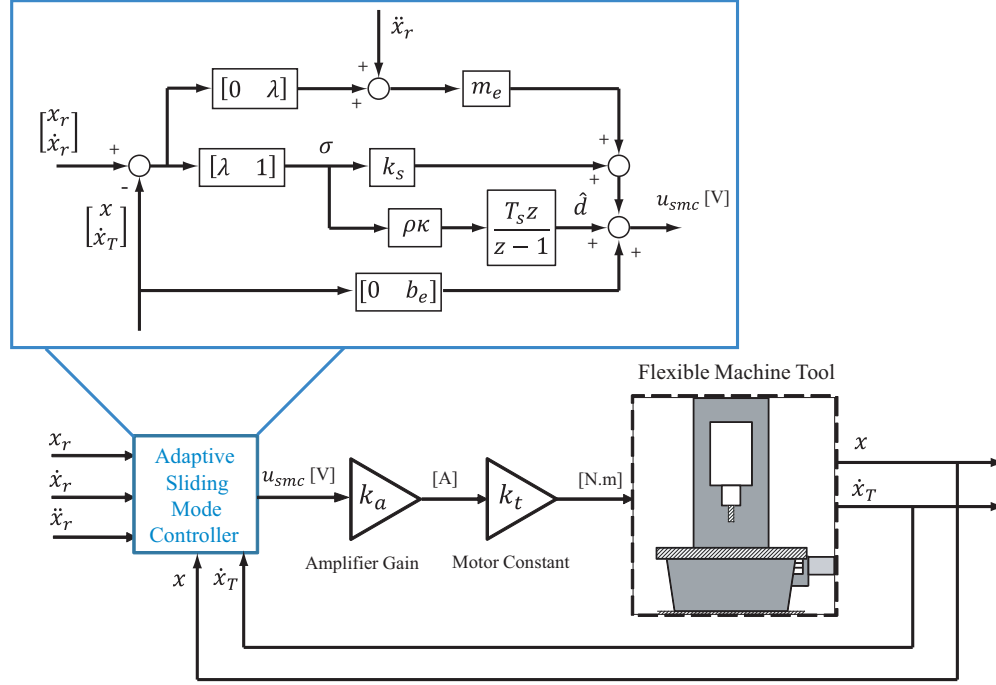


Figure 4.21: The control loop block diagram

In experimental implementation, the reference velocity (\dot{x}_r) and acceleration (\ddot{x}_r) are obtained by numerical differentiation of the reference position command (x_r). The integration term in controller disturbance compensation is computed numerically through Euler technique where the control interval (T_s) is set to 1 [ms]:

$$\dot{x}_r = \frac{1}{T_s} [x_r(k) - x_r(k-1)] \quad \ddot{x}_r(k) = \frac{1}{T_s} [\dot{x}_r(k) - \dot{x}_r(k-1)] \quad (4.71)$$

$$\hat{d}(k) = \hat{d}(k-1) + T_s \rho \kappa \sigma(k) \quad (4.72)$$

The given trajectory is a back and forth motion with trapezoidal velocity profile (Figure 4.22) to excite structural dynamics properly, and is designed to attain maximum acceleration and deceleration of 2 [m/s], and feedrate of 0.3 [m/s].

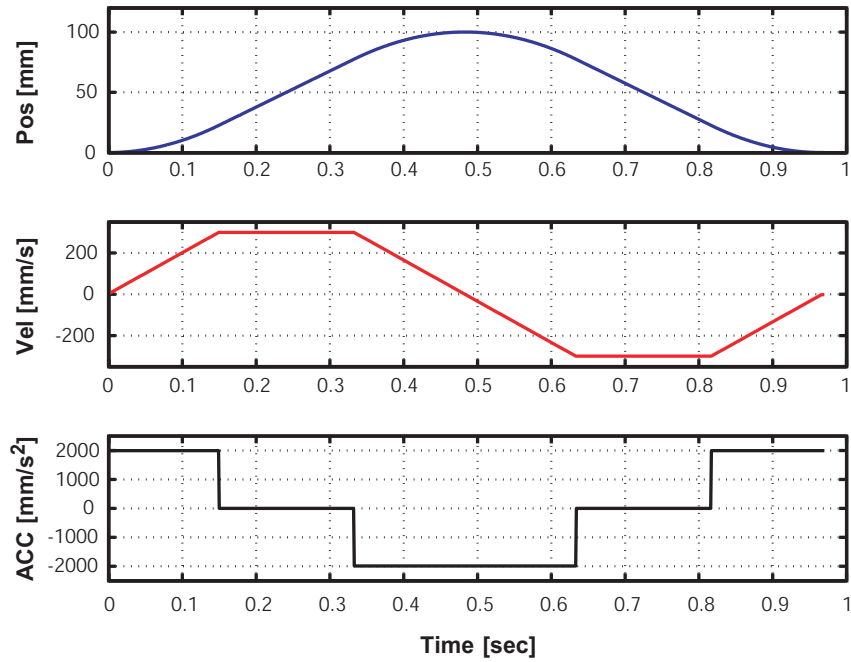


Figure 4.22: Reference trajectory with trapezoidal velocity profile

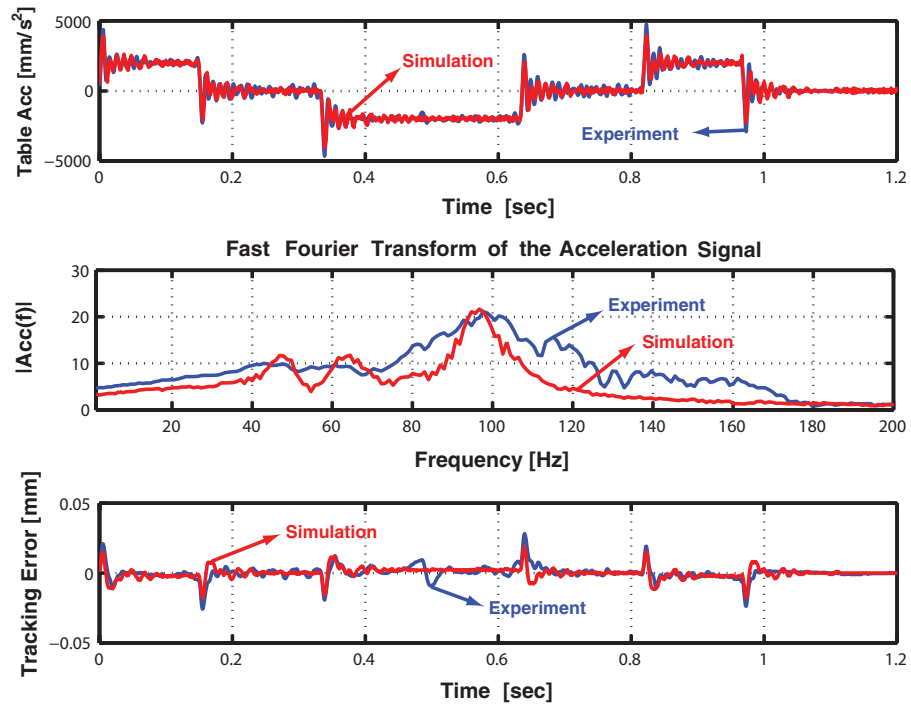


Figure 4.23: Comparison of simulated and experimental machine acceleration

Figure 4.23, compares the simulated and experimental table acceleration measured by the linear encoder. The second plot in Figure 4.23 presents the FFT transform of the measured acceleration in the low frequency range of (1-200 [Hz]). As it shows, with the medium bandwidth adaptive sliding mode controller ($\lambda = 200$ [rad/s]), the supplied trajectory excites the low frequency modes (49, 61, and 97 [Hz]) and the ball-screw axial mode (97 [Hz]) is more flexible than column bending and torsion modes (49 and 61 [Hz]).

4.7 Structural Dynamics in Finite Element Models

Finite element models are proven to be quite efficient in analyzing structural dynamics ahead of physical production for the purpose of improving the designed machine structure. In this section, based on a Finite Element model developed in ANSYS[®] software for the same machine [57], the simulated FRF between motor torque and table displacement measured by linear encoder is extracted and compared with experimental results presented in Section 4.5.2.

The finite element model does not include the conversion of motor torque to axial force between the machine table and the nut. This axial force which is the main source of vibrations in real machine, is imitated in FE by exerting an external axial force in *negative* direction at the ball-screw where the nut is mounted. The FRFs between this axial force and axial vibration at the nodes where encoder scale (node A in Figure 4.24) and its optical head (node B in Figure 4.24) are mounted in the real machine are subtracted. The contribution of structural vibration in the frequency response function between the torque applied at the ball-screw and the table vibration captured by the linear encoder can be approximated by multiplying the resultant FRF by the transfer function between motor torque and axial force ($1/r_g$). This FRF which is depicted in Figure 4.25 reveals the existence two low frequency modes around 39 [Hz] and 130 [Hz], which are associated with the column bending and ball-screw axial flexibilities, respectively, and lots of higher frequency modes.

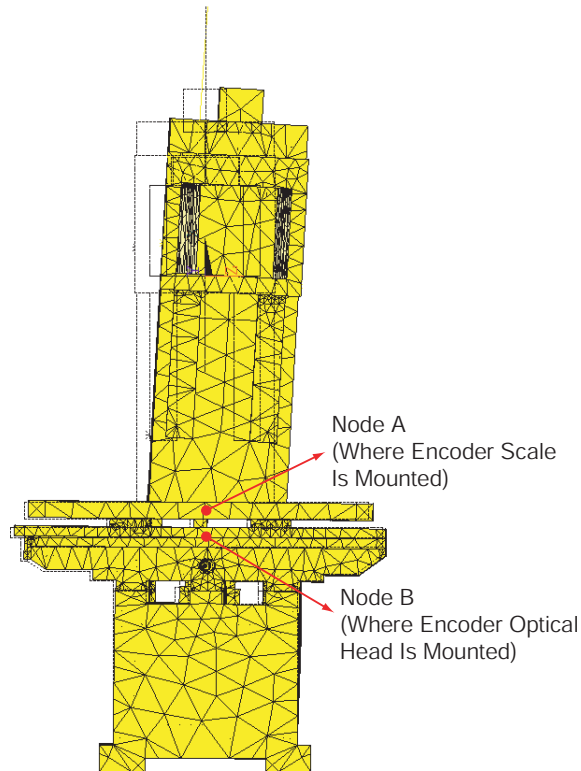


Figure 4.24: Finite Element model of the column bending mode for the machine tool with structural flexibility

Although the FRF obtained by finite element modeling can successfully predict existence of the column bending mode and dominance of the ball-screw axial mode in machine table response, there is still a large discrepancy between the simulated and experimental FRFs. The discrepancies can be seen in frequency and amplitude of the predicted modes; however, they are acceptable as long as the simulated and experimental mode shapes are the same. The main reason for the observed differences is that a typical machine tool includes many types of joints (bolted connections, connections between the guide-block and rail, between ball-screw and nut, and the bearing supports), each with different characteristics that have different effects on the overall machine dynamic response. Therefore, if an accurate FRF prediction is sought, the joints' dynamics effects also must be taken into account [59]. Moreover, in developing the

finite element model, it is assumed that all the modes have the same damping ratio (ζ_i) of 5%, however, experimental results show that different modes manifest different damping ratios.

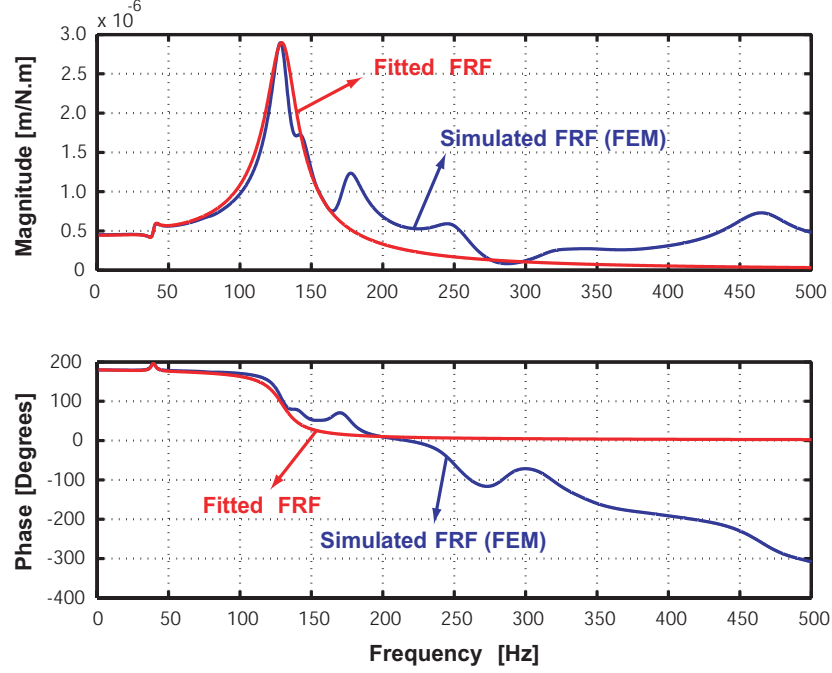


Figure 4.25: Comparison of Fitted and Simulated FRF of structural dynamics obtained from FEM ($G_f'(s)$, see Equation 4.75)

Following a similar procedure presented in the modeling section (see Section 3.3.3) with only considering the column bending and the ball-screw axial modes, the transfer function between motor torque and table position capture by linear encoder has the following structure:

$$G_e(s) = \frac{x(s)}{T_m(s)} = \underbrace{\frac{r_g}{s(J_e s + B_e)}}_{G_r(s)} \times K_f \underbrace{\frac{\prod_{i=1}^2 (s^2 + a_i s + b_i)}{\prod_{i=1}^2 (s^2 + 2\zeta_i \omega_{ni} s + \omega_{ni}^2)}}_{G_f(s)} \quad (4.73)$$

Because the column torsion mode is eliminated, the numerator and denominator of $G_f(s)$ are of 4th order. As stated before, the developed finite element model is not capable of modeling the rigid body motion of the machine table; therefore, the FRF depicted with blue color in Figure 4.25 only represents the contribution of structural vibrations on the machine table

4.8. Summary

response. The overall machine table response including the rigid body and structural dynamics can be obtained by superposing the structural vibrations ($G'_f(s)$) on top of the rigid body motion as ($G_r(s)$) and as:

$$G_e(s) = G_r(s) + G'_f(s) \quad (4.74)$$

Since $G'_f(s)$ represents the dynamics of two modes (column bending and ball-screw axial modes), in *summation* form, we have:

$$G'_f(s) \left[\frac{m}{N.m} \right] = \frac{r_1}{s^2 + 2\zeta_1 \omega_{n1}s + \omega_{n1}^2} + \frac{r_2}{s^2 + 2\zeta_2 \omega_{n2}s + \omega_{n2}^2} = K_f \frac{(s^2 + \alpha s + \beta)}{\prod_{i=1}^2 (s^2 + 2\zeta_i \omega_{ni}s + \omega_{ni}^2)} \quad (4.75)$$

Table 4.3: Identified parameters of $G'_f(s) [m/N.m]$ (see Equation (4.75)).

$K_f = -0.3075$	$\alpha = 24.8$	$\beta = 6.038 \times 10^4$	
$\zeta_1 = 0.05$	$\omega_{n1} = 249.9$	$\zeta_2 = 0.08$	$\omega_{n2} = 817.09$

Table 4.3 summarizes the parameters of $G'_f(s)$ identified by following a similar procedure presented in Section 4.3. Comparison of the fitted FRF ($G'_f(j\omega)$) with the simulated FRF obtained from finite element modeling is shown in Figure 4.25.

4.8 Summary

In the ball-screw test bed, the direct table frequency response to disturbance force and its indirect frequency response to the motor torque are measured by conducting impact test and sweeping sinusoidal voltage supplied to the motor, respectively. Comparison of the experimental FRFs reveal that the sine sweeping technique leads to more accurate measurement of the natural frequency and the damping ratio of the ball-screw torsional mode than hammer test.

4.8. *Summary*

The feed drive rigid body dynamics is identified by ULS technique and its structural dynamics is estimated by Peak Picking algorithm and curve fitting in frequency domain.

For the vertical machining center, the experimental FRF showed many low frequency modes among which the column bending and torsion and the ball-screw axial mode were dominant. The machine table dynamics is identified in a similar way to the ball-screw test bed. However, proximity of the modes required more advanced techniques for estimation of modal parameter; therefore, Rational Fraction Polynomials was utilized. The identified mathematical model is validated by simulating feed drive dynamics in control loop and comparing the results with experiment.

At the end, the simulated FRF obtained from finite element modeling of the machine structure was compared with experimentally measured FRF. Despite the observed discrepancies, it was shown that the finite element model can efficiently predict the machine mode shapes and dominance of the ball-screw axial mode in the machine table response.

Chapter 5

Drive-Based Vibration Reduction

5.1 Overview

This chapter addresses the effect of structural vibrations on the control loop of CNC machine tools. The mathematical model of the flexible machine tool, identified in Chapter 4, is used in Section 5.2 to simulate the performance of the servo loop with a high bandwidth sliding mode controller. Section 5.3 is focused on modification of the controller structure by using the machine table's acceleration in the feedback loop to attenuate the undesired effects of structural dynamics. Efficiency of the active vibration control technique is validated experimentally in Section 5.5 followed by the summary of the chapter in Section 5.6.

5.2 Structural Dynamics in Control Loop

Designing high bandwidth controllers is essential for accurate positioning of feed drives, and developing new techniques for smooth trajectory generation mitigates the excitation of flexible dynamics in machine tools. In this section, the identified mathematical model of the vertical machining center ($G_e(s)$ in Equation (4.69)) is simulated in a control loop to evaluate the effect of structural dynamics on feed drive motion when rapid positioning is demanded. For this purpose the Adaptive Sliding Mode Controller (ASMC) introduced in Section 4.6 is tuned to have a high bandwidth (~ 80 [Hz]) with parameters $\lambda = 600$ [rad/s], $k_s = 0.3$ [V/(mm/s)] and $\rho = 50$ [V/mm]. The disturbance is limited to voltage equivalent of $(d^+, d^-) = (+0.7, -0.7)$

[V] and the reflected mass and viscous damping coefficients (m_e and b_e) are the same as Section 4.6.

$$u_{smc} = K_s \sigma + m_e [\ddot{x}_r + \lambda (\dot{x}_r - \dot{x}_T)] + b_e \dot{x}_T + \hat{d}$$

where σ , m_e , b_e , and \hat{d} are introduced in Equation 4.70. The trajectory generation of the CNC is set to cubic acceleration with a saturation limit of 2 [m/s] and feedrate of 0.3 [m/s] as shown in Figure 5.1. The control interval is set to 1 [ms].

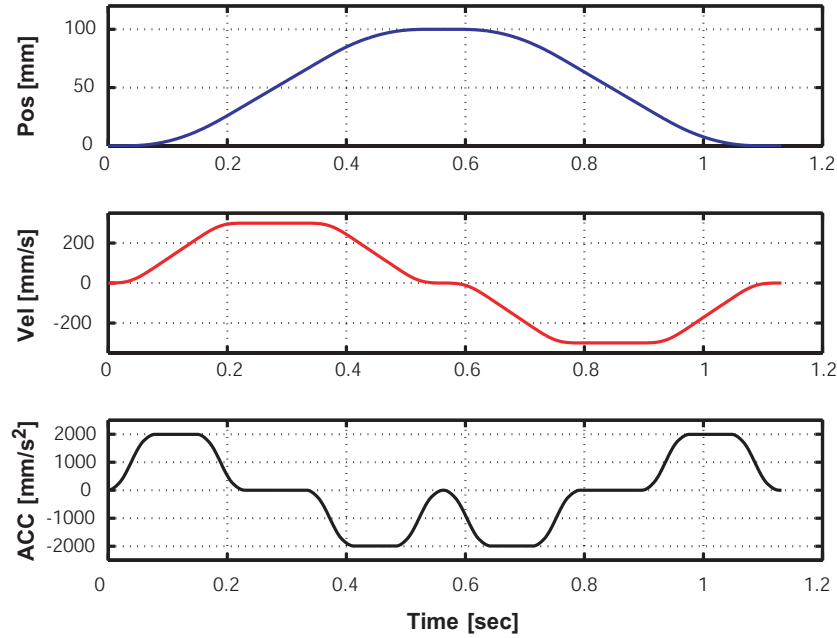


Figure 5.1: Reference trajectory with cubic acceleration profile

The control system is simulated by including both the rigid body and the structural dynamics of the drive (Equation 4.69) to mimic the real machine tool drive controller. The simulated and experimentally measured acceleration of the table are shown in Figure 5.2. The frequency spectrum shows that the axial mode (97.88 [Hz]) of the ball screw is heavily excited by the high bandwidth controller. The tracking errors have amplitude of 50 [μ m] which leave unacceptable vibration marks on the finish surface. In addition, the controller attempts to counteract

the vibrations felt by the position feedback (linear encoder), and sends high frequency control commands with large amplitudes which saturate the amplifier. Although the high bandwidth controllers are desirable for accurate tracking of multi-axis tool paths, the increased frequency content of the controller input excites the machine tool vibrations. The bandwidth of the drive had to be reduced to less than 30 [Hz] ($\lambda = 200$ [rad/s]) in order to avoid excitation of the vibrations. The structural vibrations must either be avoided through shaping position commands ahead of the control loop, or be actively damped in the control loop if a high bandwidth controller is desired to be used on high feed machine tools.

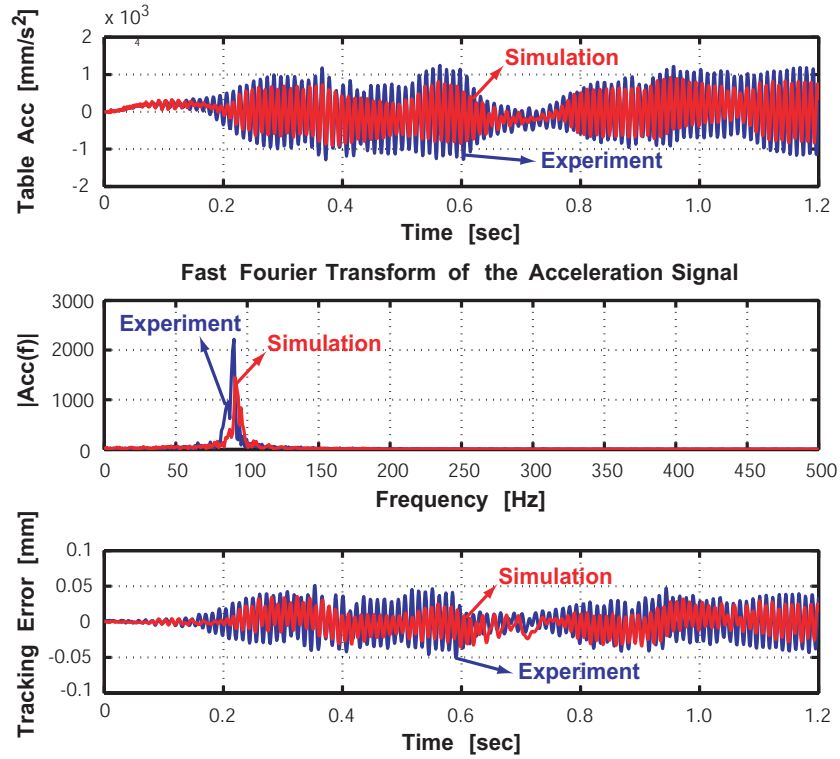


Figure 5.2: Comparison of simulation and experimental results for the ball screw drive controlled by a high bandwidth sliding mode controller without active damping.

Figure 5.3 presents the simulated table acceleration when machine dynamics in control loop is replaced by the FRF obtained based on the finite element model (Equation (4.73)). The fast Fourier transform of the acceleration signal shows that, similar to Figure 5.2, the axial

mode of the ball-screw is heavily excited and caused saturation of the amplifier output current. Therefore, the model developed based on the finite element analysis of the machine structure is capable of predicting the effect of structural flexibilities in control loop ahead of physical production and can be used to improve the design.

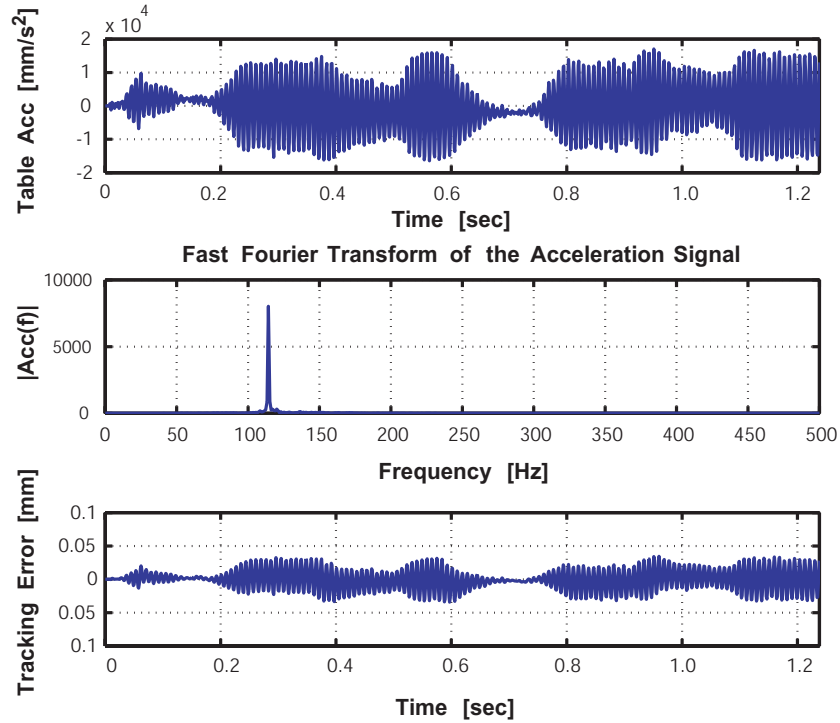


Figure 5.3: The simulated table acceleration based on the FE model - high bandwidth sliding mode controller without active damping.

5.3 Vibration Reduction with Acceleration Feedback

Drive based vibration reduction proposed by Dietmair and Verl [44] is an effective, and at the same time low cost method of increasing damping ratio for a specific mode in production machines and robotic arms. This method increases the damping ratio by modifying the velocity loop, when there is a cascade control structure where position and velocity loops can be distinguished. Section 5.3.1 provides an overview of the theoretical basis of using acceleration

feedback for active vibration reduction for the cascade control structure. Section 5.3.2 extends this approach to the case of using nonlinear sliding mode controller in servo loop.

5.3.1 Cascade Control Structure

A thin bar, used as a single degree of freedom (SDOF) oscillator, which is mounted on a ball-screw drive's table is shown in Figure 5.4.

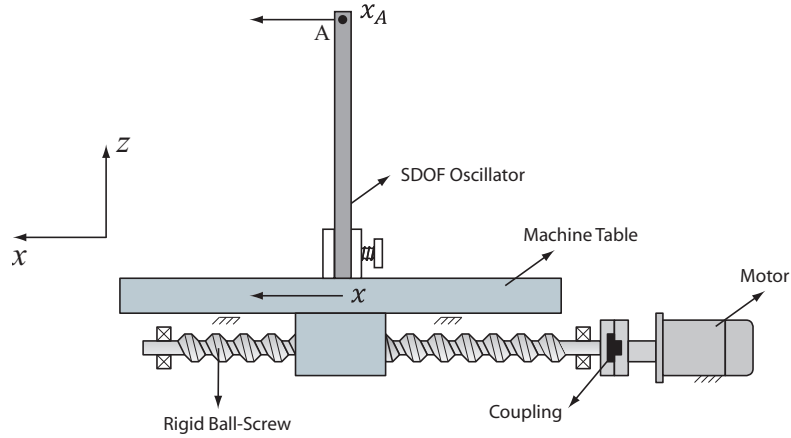


Figure 5.4: A single degree of freedom oscillator mounted on the ball-screw table.

This bar exhibits bending flexibilities and its dynamics can be expressed as:

$$\frac{x_A}{x} \simeq \frac{\omega_n^2}{s^2 + 2\zeta\omega_n s + \omega_n^2} \quad (5.1)$$

where x_A represents the vibrations at the oscillator's tip point and x indicates the ball-screw's table displacement. The inertial forces generated by the rapid positioning of the machine table cause the flexible beam to vibrate. Drive based vibration reduction concerns the algorithms which enhance the damping ratio of a target mode and lead to faster vibration attenuation of the flexible beam.

Figure 5.5 presents the control loop block diagram of the ball-screw drive when a cascade control law is implemented.

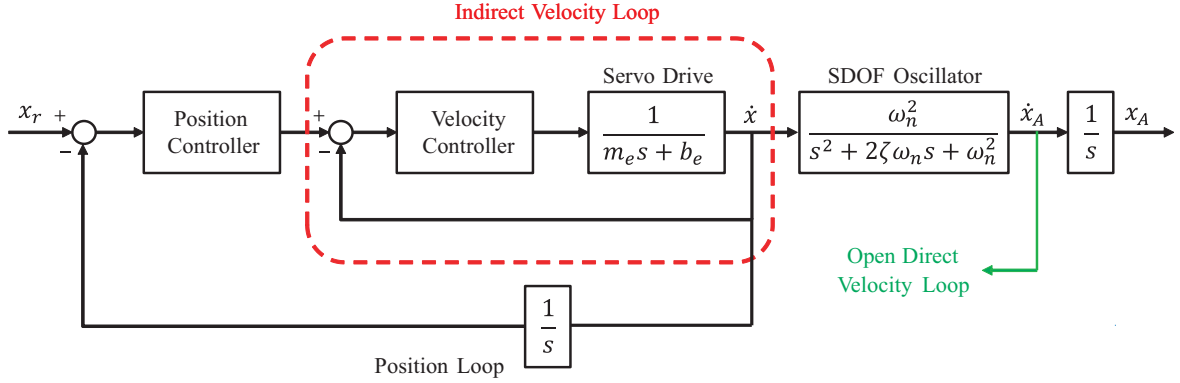


Figure 5.5: Cascade control structure for the ball-screw drive

The indirect velocity loop uses the motor's angular velocity measured from a tacho-generator or rotary encoder mounted on the motor shaft [5] to ensure a fast system response in tracking the velocity command. The position loop uses the linear or rotary encoder position feed back for accurate positioning of the machine table (x).

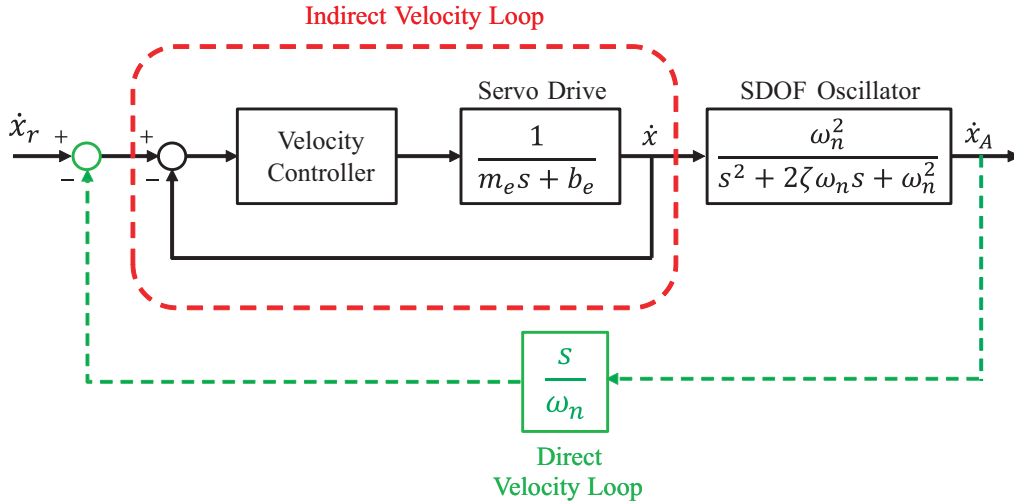


Figure 5.6: Velocity loop of ball screw drives with single degree of freedom oscillator and active damping

An easy to implement approach of suppressing the oscillator's vibrations, is to include its dynamics in the control loop of the ball-screw drive; for this purpose, 90° phase shift with unity gain at the natural frequency (ω_0) is made in the direct velocity loop as shown in Figure

5.6. The direct velocity loop uses the velocity measured at the oscillator's tip point (\dot{x}_A) for feedback. This velocity can be measured by using a laser vibrometer or an accelerometer attached to the point A in Figure 5.4.

In considering the dynamics of the SDOF oscillator, provided that its vibrations occur at a frequency (ω_0) within the bandwidth of the indirect velocity loop, this loop can be approximated by its DC gain (K_v) as shown in Figure 5.7.

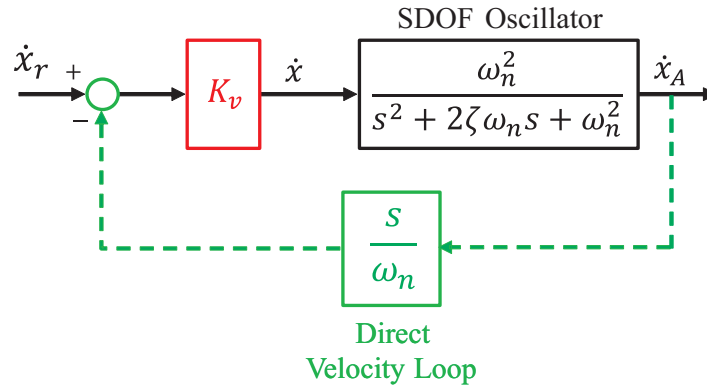


Figure 5.7: Velocity loop of ball screw drives with single degree of freedom oscillator and active damping - The indirect velocity loop is replaced by its DC gain (K_v)

The closed loop transfer function of the direct velocity loop ($G_v(s)$) obtained from Figure 5.7 is:

$$G_v(s) = \frac{\dot{x}_A(s)}{\dot{x}_r(s)} = \frac{K_v \omega_n^2}{s^2 + 2(\zeta + K_v/2)\omega_n s + \omega_n^2} \quad (5.2)$$

Equation 5.2 reveals that the damping property is enhanced. For systems with multiple modes, an active damping network must be designed in which each mode is isolated by cascading a band-pass filter prior to the phase-shifter, summation of the phase shifter outputs builds the feedback to the velocity loop. The bandpass filters limit the effect of the phase compensator within a frequency range.

5.3.2 Adaptive Sliding Mode Controller

The simulation and experimental results presented in Section 5.2 showed that, although a smooth trajectory with cubic acceleration profile is supplied to the servo loop, utilizing a high bandwidth controller causes inertial forces to excite the structural flexibilities. The vibrations induced by the inertial forces lead to heavy control effort which saturates the servo loop's amplifier. To solve the saturation problem and reduce these vibrations, the table's acceleration measured by taking double derivative of the linear encoder signal is used in the direct velocity loop to increase the damping ratio of the problematic mode (Axial mode of the ball-screw).

The controller used in Section 5.2 is an adaptive sliding mode controllers which, due to the adaptation in the disturbance compensation term (\hat{d}), has a nonlinear control structure. Therefore, in the first step, the controller must be restructured in a way that it is possible to distinguish the direct velocity loop, the indirect velocity loop and the position control loop. For this purpose, by considering κ in Equation 4.70 as a constant, the control law is linearized as:

$$\begin{aligned}
 u_{smc} = & K_s [(\dot{x}_r - \dot{x}_T) + \lambda (x_r - x)] + m_e [\ddot{x}_r + \lambda (\dot{x}_r - \dot{x}_T)] + \\
 & b_e \dot{x}_T + \kappa \rho \left[(x_r - x) + \lambda \int_0^t (x_r - x) dt \right] = \\
 & k_v \left[(\dot{x}_r - \dot{x}_T) + k_p [x_r - x] + k_{ff} \ddot{x}_r + k_I \int_0^t (x_r - x) dt \right] + b_e \dot{x}_T
 \end{aligned} \tag{5.3}$$

where

$$k_v = (K_s + m_e \lambda); k_p = \frac{K_s \lambda + \kappa \rho}{K_s + m_e \lambda}; k_{ff} = \frac{m_e}{K_s + m_e \lambda}; k_I = \frac{\kappa \rho \lambda}{K_s + m_e \lambda} \tag{5.4}$$

Figure 5.8 depicts the closed loop block diagram with the linearized adaptive sliding mode controller from which it is possible to extract the direct and indirect velocity loops and the position loop. As this figure shows, the control law in the indirect velocity loop is a proportional controller of gain k_v which is independent of κ .

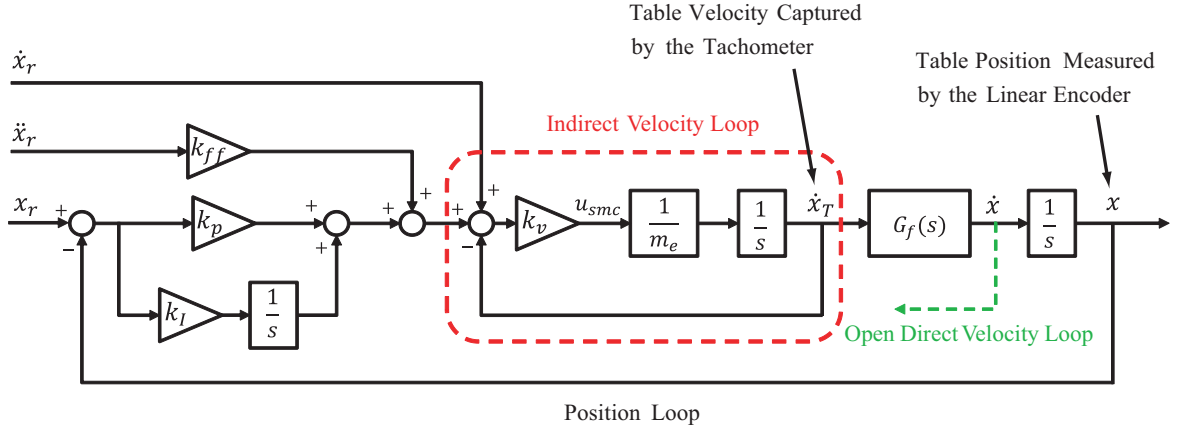


Figure 5.8: Control loop for the linearized adaptive sliding mode controller

The velocity loop of the adaptive sliding mode controller has been modified to include a damping network as presented in Figure 5.9.

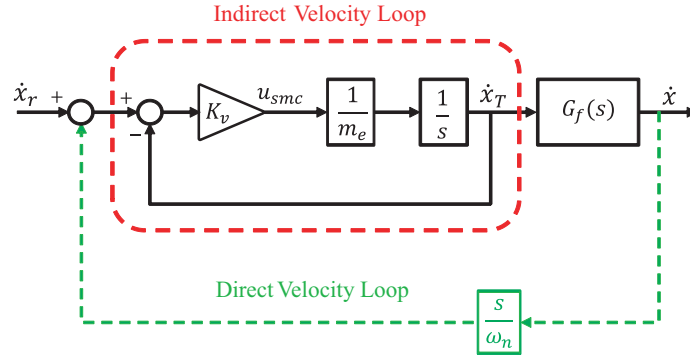


Figure 5.9: Velocity loop of the linearized adaptive sliding mode controller with active damping network included in the direct velocity loop

Similar to the SDOF oscillator, the phase shifter is a signal differentiator which is normalized at the natural frequency of the ball-screw axial mode ($\omega_n = 97$ [Hz]). In this case, although the flexible machine tool has several modes, the damping network includes no bandpass filters, because the modes are closely spaced and incorporating band-pass filters for each mode leads to sharp phase shifts in the phase plot; these sharp phase shifts make the control loop highly susceptible to non-modeled dynamics and non-linearities in the system, which renders the ineffectiveness of the active damping network. Therefore, the most flexible mode felt by the

5.3. Vibration Reduction with Acceleration Feedback

linear encoder, which is the ball-screw axial mode, is considered for vibration reduction based on the servo drive.

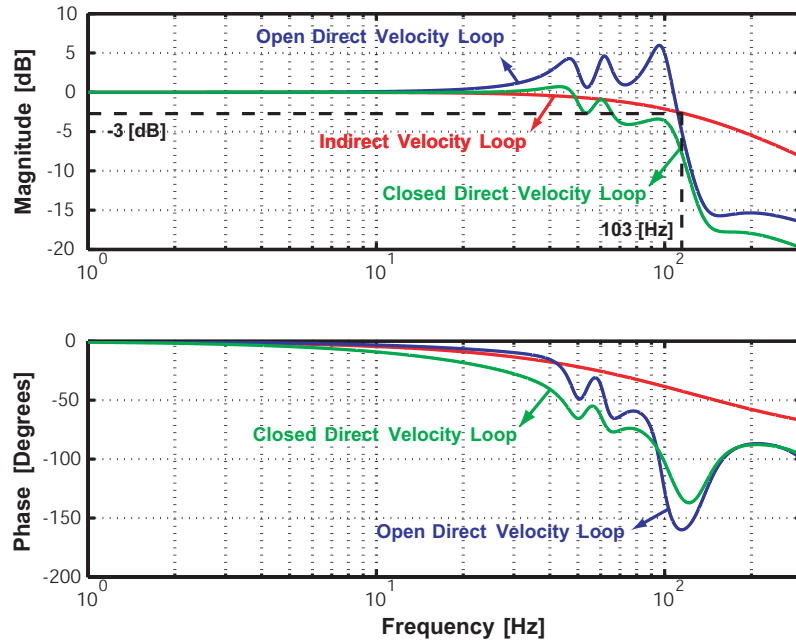


Figure 5.10: Bode plots of different velocity loops

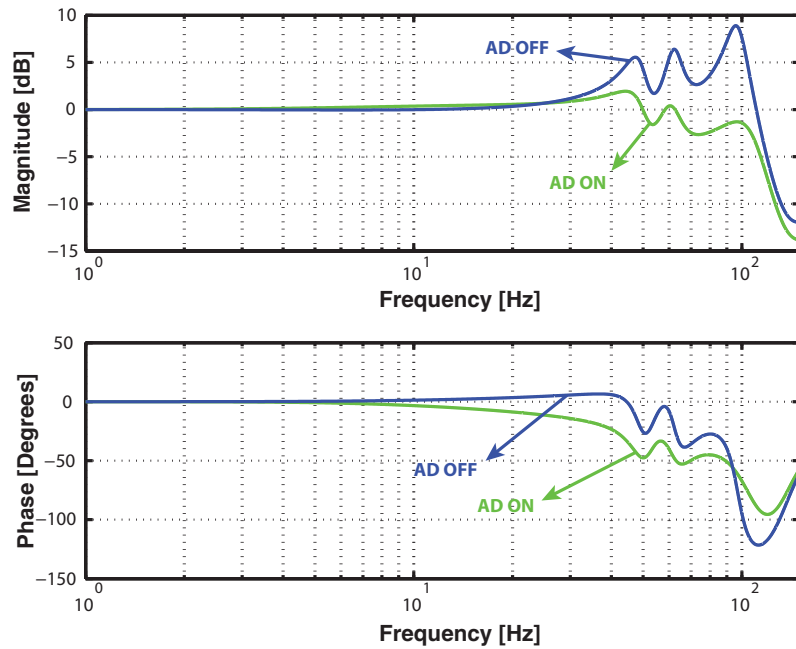


Figure 5.11: Bode plots of the position loop with and without active damping

Bode plots of the indirect and direct velocity loops for the adaptive sliding mode controller are compared in Figure 5.10. Figure 5.11 compares the bode plots for the position loop with and without active damping.

Table 5.1: Comparison of damping ratios before and after active damping

	Mode 1 (49 [Hz])	Mode 2 (61 [Hz])	Mode 3 (97 [Hz])
Without AD	$\zeta_1 = 0.083$	$\zeta_2 = 0.060$	$\zeta_3 = 0.091$
With AD	$\zeta'_1 = 0.10$	$\zeta'_2 = 0.07$	$\zeta'_3 = 0.17$
Percentage of Increase	20.48%	16.67%	86.61%

The frequency of the ball-screw axial mode is around 97 [Hz] which lies within the bandwidth of the indirect velocity loop (~ 103 [Hz]); therefore, modifying the control loop must be efficient for drive-based vibration reduction, and as Figure 5.10 shows the damping ratio of the axial mode of the ball-screw drive is increased by adding the damping network. As Table 5.1 indicates, the damping ratios for all three modes are increased, even though the damping network was designed based on the ball-screw's vibrations only.

The phase shifter included in the direct velocity loop is an s transfer function which takes derivative of the velocity signal and gives the acceleration as an output. Therefore, instead of using the measured velocity and the phase shifter, it is possible to normalize the acceleration signal at the natural frequency (ω_n) in the augmented feedback loop. The table's acceleration can be estimated from the linear encoder output. However, taking double derivative of the encoder output introduces a heavy noise to the acceleration signal. This noisy signal is not appropriate for the feedback loop, it can saturate the amplifier and overheat the motor. Employing a low pass filter is the initial attempt to minimize the noise but it adds delay to the feedback loop which deteriorates the active damping network performance. Designing a Kalman filter based on the identified mathematical model is beneficial in removing the noise without sacrificing the vibration control performance.

5.4 Kalman Filter Design

The Kalman Filter algorithm uses the identified model (Equation 4.69) to estimate the states of a linear system based on the measurements which contain sensor noise and other inaccuracies.

$$G_e(s) = \frac{x(s)}{T_m(s)} = \frac{r_g}{s(J_e s + B_e)} \times K_f \frac{\prod_{i=1}^3 (s^2 + a_i s + b_i)}{\prod_{i=1}^3 (s^2 + 2\zeta_i \omega_{ni} s + \omega_{ni}^2)}$$

The state space representation of the identified mathematical model in discrete time domain obtained by using the Control Toolbox in MATLAB® software is:

$$\begin{cases} z(k+1) = A_d z(k) + B_d u(k) \\ y(k) = C_d z(k) + D_d u(k) \end{cases} \quad (5.5)$$

where $u(k)$ is control input to the servo amplifier. The output vector ($y(k) = [x(k) \ddot{x}(k)]^T$) contains measured table position (x) and acceleration (\ddot{x}). The matrices A_d , B_d , C_d and D_d for the experimental machine are derived as:

$$A_d = \begin{bmatrix} 0.5311 & -0.5523 & -0.2160 & -0.3436 & -0.1119 & -0.2497 & -0.0263 & 0 \\ 0.8239 & 0.7016 & -0.1015 & -0.1900 & -0.0556 & -0.1403 & -0.0148 & 0 \\ 0.2316 & 0.4599 & 0.9836 & -0.0335 & -0.0093 & -0.0249 & -0.0026 & 0 \\ 0.0411 & 0.1243 & 0.5100 & 0.9956 & -0.0012 & -0.0033 & -0.0003 & 0 \\ 0.0027 & 0.108 & 0.0654 & 0.2558 & 1 & -0.0002 & 0 & 0 \\ 0.0001 & 0.0007 & 0.0056 & 0.0328 & 0.2560 & 1 & 0 & 0 \\ 0 & 0 & 0 & 0.0003 & 0.0041 & 0.0320 & 1 & 0 \\ 0 & 0 & 0 & 0 & 0 & 0 & 0.001 & 1 \end{bmatrix}$$

$$B_d = \begin{bmatrix} 0.0064 & 0.0036 & 0.0006 & 0.0001 & 0 & 0 & 0 & 0 \end{bmatrix}^T, D_d = \begin{bmatrix} 0 \\ 0.303 \end{bmatrix}$$

$$C_d = \begin{bmatrix} 0 & 0 & 0 & 0.0001 & 0.0001 & 0.0004 & 0.0012 & 0.7415 \\ 7.9394 & 13.2433 & 8.2565 & 13.0299 & 5.8278 & 11.9945 & -1.2357 & 0 \end{bmatrix}$$

The control input ($u(k)$) is given to the servo drive as $u'(k)$ after being quantized by D/A convertor with the resolution of δu . The table position ($x(k)$) is also measured as x_m after being quantized by the linear encoder with resolution of δx . The estimated acceleration $\ddot{x}_m(k)$ is different from the actual table acceleration ($\ddot{x}(k)$) because of the quantization error in position measurement (\tilde{x}).

$$\begin{cases} u'(k) = u(k) + \tilde{u}(k) \\ x_m(k) = x(k) + \tilde{x}(k) \\ \ddot{x}_m(k) = \ddot{x}(k) + \tilde{\ddot{x}}(k) \end{cases} \quad (5.6)$$

In experimental implementation, Equation 5.5 can be written in a more accurate way as:

$$\begin{cases} z(k+1) = A_d z(k) + B_d u(k) + B_d \tilde{u}(k) \\ \begin{bmatrix} x_m(k) \\ \ddot{x}_m(k) \end{bmatrix} = C_d z(k) + D_d u(k) + D_d \tilde{u}(k) + \begin{bmatrix} \tilde{x}(k) \\ \tilde{\ddot{x}}(k) \end{bmatrix} \end{cases} \quad (5.7)$$

In Kalman Filter design, \tilde{u} is called the process noise which is introduced at the system input and $\begin{bmatrix} \tilde{x}(k) \\ \tilde{\ddot{x}}(k) \end{bmatrix}$ is called measurement noise which happens at system output and is caused by poor measurement sensors. The process noise ($\tilde{u}(k)$) lies in $(-\delta u/2, \delta u/2)$ and the position quantization error ($\tilde{x}(k)$) is in the range of $(-\delta x/2, \delta x/2)$. They are assumed to have uniform distributions with zero mean values [30].

$$E(\tilde{u}(k)) = 0, E(\tilde{x}(k)) = 0 \quad (5.8)$$

$$R_u = \frac{(\delta u)^2}{12}, R_x = \frac{(\delta x)^2}{12} \quad (5.9)$$

The voltage output of the 16 bits D/A convertor is in the range of $(-10, +10)$ [V], hence its resolution is $\delta u = 20/2^{16} = 0.305176 \times 10^{-3}$ [V]. The linear encoder resolution is $\delta x = 10^{-6}$ [m]. Therefore, from Equations 5.9, the quantization error covariance values are calculated as:

$$R_u = 7.7610 \times 10^{-9} [V^2]; R_x = 8.3333 \times 10^{-8} [mm^2] \quad (5.10)$$

To reach a satisfactory performance for the Kalman Filter, $R_{\ddot{x}}$ is tuned to be 50×10^{-3} [mm²/s²]. The process noise (Q) and measurement noise (R) covariance matrices are defined as:

$$Q = R_u; R = \begin{bmatrix} R_x & 0 \\ 0 & R_{\ddot{x}} \end{bmatrix} \quad (5.11)$$

The Kalman filter, composed of the state estimator ($\hat{z}(k+1|k)$) and filtered position and acceleration ($\hat{y}(k|k) = [\hat{x}(k) \ \hat{\ddot{x}}(k)]^T$), has the following structure [60]:

$$\begin{cases} \hat{z}(k+1|k) = A_d \hat{z}(k|k-1) + B_d u(k) + L(y(k) - C_d \hat{z}(k|k-1) - D_d u(k)) \\ \hat{y}(k|k) = C_d (I - M C_d) \hat{z}(k|k-1) + (I - C_d M) D_d u(k) + C_d M y(k) \end{cases} \quad (5.12)$$

The gain matrix (L) and innovation gain matrix (M) are calculated in terms of the noise covariance data (Q, R) as:

$$L = (A P C^T + D_d Q B_d^T) (C P C^T + R + B_d Q B_d^T)^{-1} \quad (5.13)$$

$$M = P C^T (C P C^T + R + B_d Q B_d^T)^{-1} \quad (5.14)$$

where P is solution to the corresponding algebraic Riccati equation. Having the covariance matrices of the process noise and measurement noise computed off-line, the L and M matrices are evaluated for the experimental machine as follows:

$$L = \begin{bmatrix} 0.0035 & 0.0010 & 0.0055 & 0.0001 & -0.0041 & -0.0188 & 0.1787 & 0.0217 \\ 0 & 0 & 0 & 0 & 0 & 0 & 0 & 0 \end{bmatrix}^T$$

$$M = \begin{bmatrix} 0.0021 & -0.0039 & -0.0042 & 0.0026 & -0.0045 & -0.0177 & 0.1793 & 0.0215 \\ 0 & 0 & 0 & 0 & 0 & 0 & 0 & 0 \end{bmatrix}^T$$

5.5 Experimental Implementation

The adaptive sliding mode controller has been modified to include a damping network as presented in Figure 5.12. The noise in the estimation of acceleration from double digital differentiation of the encoder signal is minimized by the Kalman Filter designed in Section 5.4.

The inertial vibrations are actively damped by the following acceleration feedback added to sliding mode controller command:

$$u(k) = u_{smc}(k) - k_v \frac{\hat{\ddot{x}}(k-1)}{\omega_n} \quad (5.15)$$

where k_v is the gain of indirect velocity loop of adaptive sliding mode controller. The sliding mode controller parameters were set the same as in the case without active damping network (see Section 5.2), and the active damping is set to damp the axial mode ($\omega_n = 611$ [rad/s] = 97.88 [Hz]) of the ball screw. The servo performances with and without active damping are compared in Figure 5.13. The vibration mode is completely damped out, and the amplitudes of tracking error oscillations (i.e. vibrations) are reduced from 50 [μm] to 5 [μm].

As Figure 5.14 shows, when active damping is applied the saturation problem with the

controller is solved.

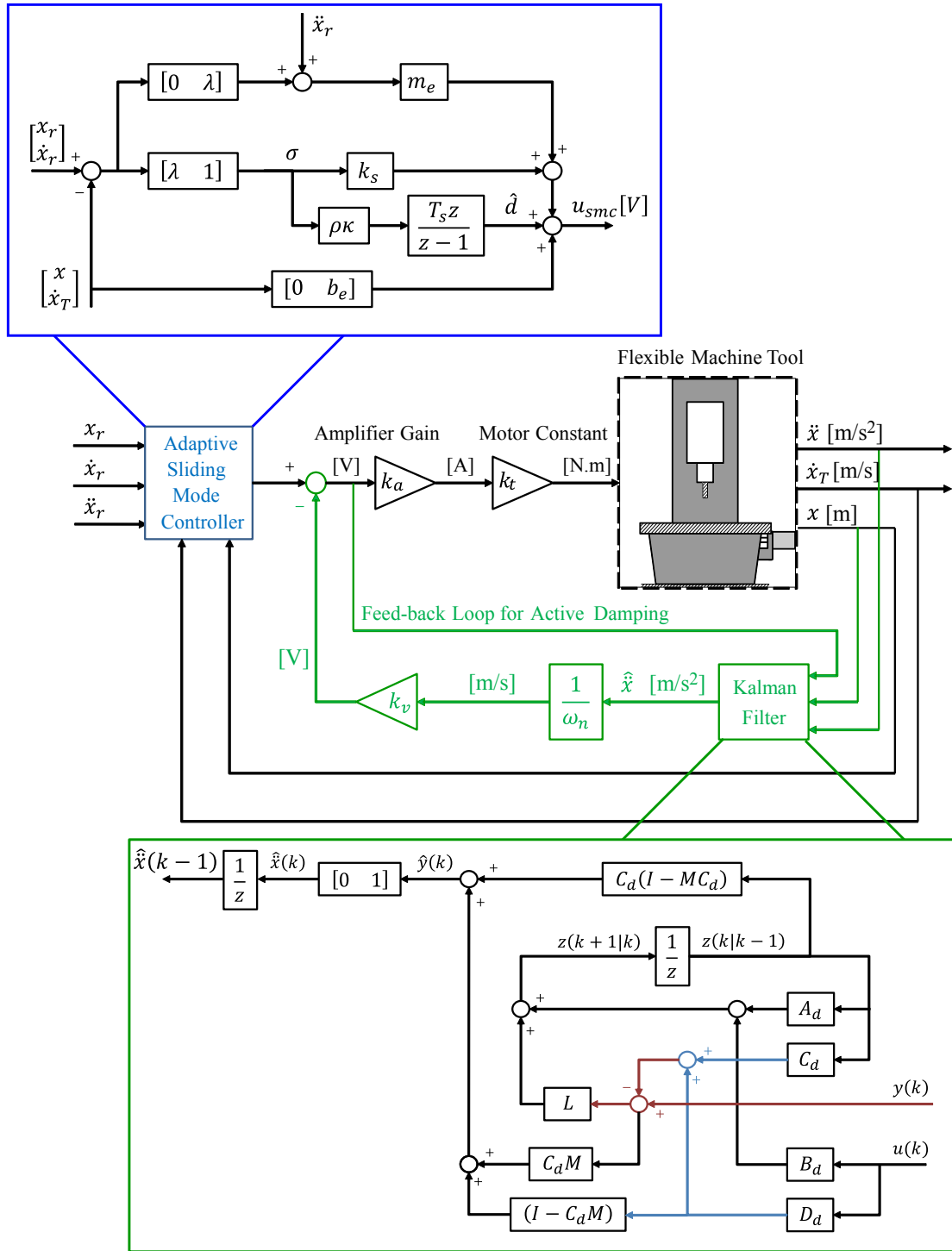


Figure 5.12: Block diagram of sliding mode controller with and without active damping of vibration mode with a natural frequency ω_n

5.5. Experimental Implementation

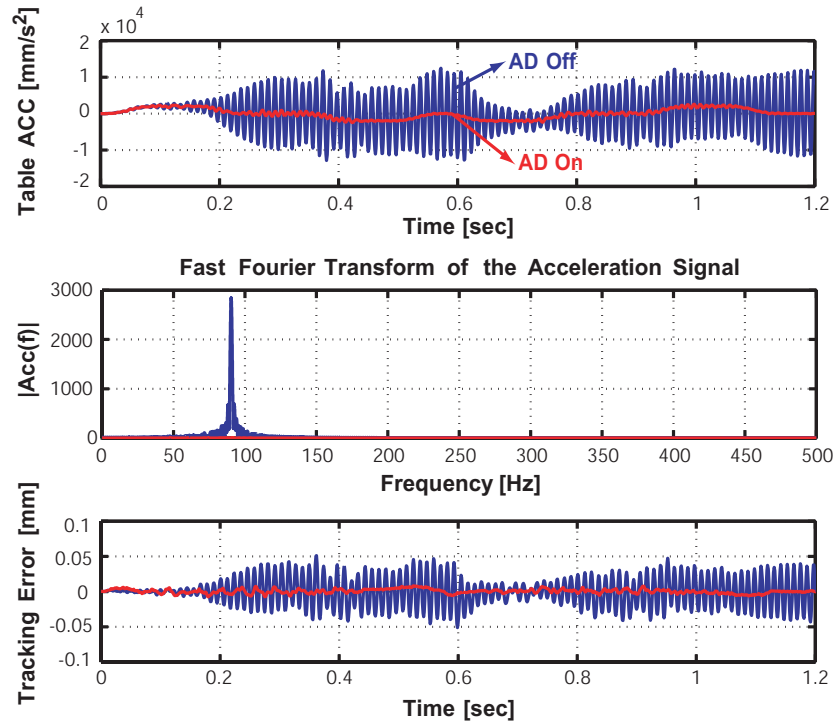


Figure 5.13: Comparison of experimental results for the machine tool feed drive with and without active damping (AD)

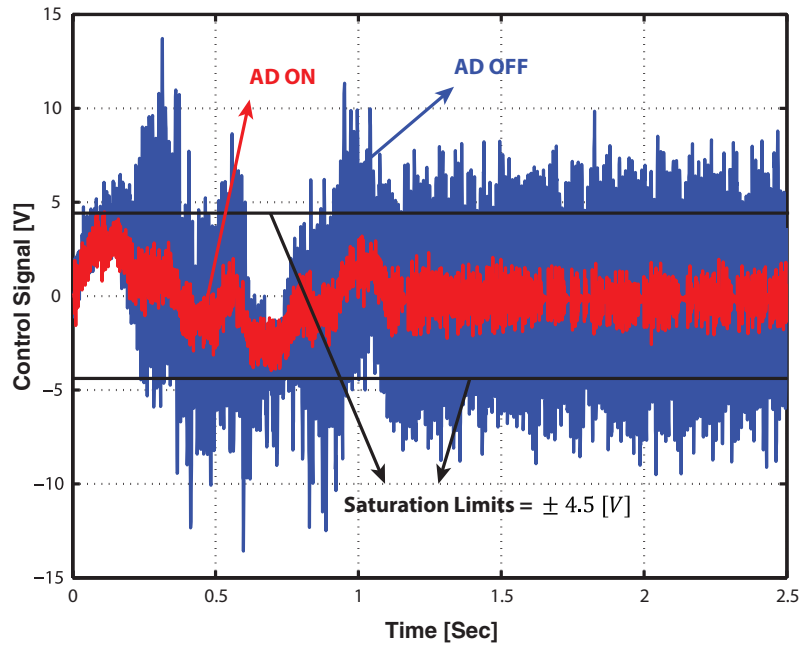


Figure 5.14: Comparison of the control command (u) with and without active damping (AD)

5.6 Summary

The simulation and experimental results showed that although a smooth trajectory was commanded to the servo loop, structural modes are excited. The residual vibrations, which were sensible through the feedback sensors, resulted in saturation of the servo amplifier and ceaseless vibration of the machine tool structure. It was shown that using the table's acceleration, which is normalized at the natural frequency of the ball-screw axial mode, increased the damping property of the problematic mode and caused faster attenuation of the structural vibrations. This acceleration was estimated by passing the double derivative of the linear encoder signal through a Kalman filter. Experimental result confirmed the efficiency of active vibration control technique in stabilizing the control loop and solving the saturation problem.

Chapter 6

Conclusion and Future Work

In this thesis, a mathematical model of the horizontal feed drive (x -axis) of a C-frame CNC machining center has been developed. The mathematical model has been intended to explain the interaction between the control loop and structural dynamics. The model includes the fundamental low frequency modes of the machine tool column and ball screw drive to find the transfer function between the motor torque applied at the ball-screw and table position measured by the linear encoder. In the modeling procedure, the ball-screw axial and column bending and torsional modes have been represented by lumped inertias connected with linear and torsional springs and dampers. These modes are excited by inertial forces generated through acceleration and deceleration of large machine tool components.

The mathematical model was identified by fitting the obtained transfer function to the experimental FRF, which is measured by sine sweeping technique, in frequency domain. The experimental FRF showed that although the column bending mode is dominant in the machine table response, the ball-screw's axial mode gains dominancy when the relative vibration between the machine table and the bed, which is the linear encoder output, is of interest.

By utilizing the identified model, simulations were conducted to analyze the interaction between a high bandwidth adaptive sliding mode controller and the structural dynamics. The simulation results, which were verified by experiments, showed that the axial mode of the ball screw was heavily excited by the high bandwidth controller, although a smooth trajectory was supplied to the servo loop. The controller attempted to counteract against the vibrations felt by the linear encoder; therefore, it sent high frequency control commands with large amplitudes

which saturated the amplifier. Saturation of the amplifier led to incessant vibration of the machine table and drastically increased the tracking error.

A similar procedure was applied on the simulated FRF which was obtained from the finite element modeling of the machine tool structure. The FE model could predict structural mode shapes and dominance of the ball-screw axial mode in machine table response which caused saturation of the control signal.

Considering the experimental setup, a Kalman Filter was used to estimate the acceleration of the machine table from double digital differentiation of the encoder signal. The measured acceleration was added in the feedback loop for active control of the undesired vibrations. The modified control loop with enhanced damping resulted in faster attenuation of the ball-screw vibrations, stabilized the servo loop and solved the saturation problem.

In conclusion:

1. Structural flexibilities not only affect the surface finish of the final product, they also interfere with the control loop provided that the feedback sensors can feel the vibrations. The sensed vibrations can impose heavy control efforts to the control system which saturates the actuators in the servo-loop and destabilizes the closed loop system.
2. FE softwares are proven to be efficient in predicting the role of structural dynamics on cutting process in machine tools. They are typically used for analysis and topology optimization of the machine tool structure. They are also beneficial in modeling the control-structure interaction and can help control engineers in choosing the best locations for the feedback sensors and improve their design.
3. Active control of machine tool's vibrations by designing an active damping network increases the damping property of the structural modes significantly. It helps in enhancing the servo loop bandwidth, and improves the closed loop performance. Design of the active damping network can be performed independently from the controller design and

it is only beneficial when the vibrations are captured by the feedback sensors. However, for multi-mode systems with closely spaced modes, design of a proper active damping network is cumbersome.

4. The increased damping due to vibration control can increase the minimum depth of cut for a stable process in stability lobes diagram. Therefore, the vibration control can increase the productivity significantly.

This research can be continued to improve damping of the machine tools. A mathematical model which includes structural dynamics can be used for Hardware in Loop Simulations (HiLS) of machine dynamics to visually depict the machine mode shapes during the cutting process and the surface quality of the finished product. The Active vibration control technique implemented in this thesis can be extended to the case of three or five axis CNC machines to damp structural vibrations and improve the tracking and contouring performances; moreover, it can be combined with input shaping to minimize the excitation of structural flexibilities. Finally, It is essential to investigate the effect of active damping on the cutting process; therefore, future work can be concentrated on evaluating the effect of feed drives' vibration control on increasing the stiffness and damping in the FRF between tool-tip and table top. The increased damping property can enhance the productivity of cutting process by increasing the absolute minimum depth of cut for a stable process.

Bibliography

- [1] J. Vesely and M. Sulitka, “Machine tool virtual model,” *Modern Machinery (MM) Science Journal*, pp. 146–151, 2009.
- [2] D. Ford, “A CAD-CAE aid to design of a machine tool system,” Ph.D. dissertation, The University of Huddersfield, U.K., 1989.
- [3] K. Erkorkmaz and Y. Altintas, “High speed CNC system design. part II: Modeling and identification of feed drives,” *International Journal of Machine Tools and Manufacture*, vol. 41, pp. 1487–1509, 2001.
- [4] C. Pislaru, “Parameter identification and hybrid mathematical modelling techniques applied to non-linear control systems,” Ph.D. dissertation, The University of Huddersfield, U.K., 2001.
- [5] Y. Altintas, A. . Verl, C. Brecher, L. Uriarte, and G. Pritschow, “Machine tool feed drives,” *CIRP Annals - Manufacturing Technology*, vol. 60, pp. 779–796, 2011.
- [6] A. Dadalau, M. Mottahedi, K. Groh, and A. Verl, “Parametric modeling of ball screw spindles,” *Production Engineering*, vol. 4, pp. 625–631, 2010.
- [7] J. Chen, Y. Huang, and C. Cheng, “Mechanical model and contouring analysis of high-speed ball-screw drive systems with compliance effect,” *The International Journal of Advanced Manufacturing Technology*, vol. 24, pp. 241–250, 2004.

- [8] K. Lee, S. Ibaraki, A. Matsubara, Y. Kakino, Y. Suzuki, S. Arai, and J. Braasch, "A servo parameter tuning method for high-speed NC machine tools based on contouring error measurement," in *Proceeding of The Laser Metrology, Machine Tool, CMM and Robotic Performance (LAMDAMAP) Conference*, vol. 3, 2003.
- [9] P. Poignet, M. Gautier, and W. Khalil, "Modeling, control and simulation of high speed machine tool axes," in *Advanced Intelligent Mechatronics, IEEE/ASME International Conference on*, 1999, pp. 617–622.
- [10] T. Yang and C. Lin, "Identifying the stiffness and damping parameters of a linear servomechanism," *Mechanics Based Design of Structures and Machines*, vol. 32, pp. 283–304, 2004.
- [11] M. Kim and S. Chung, "Integrated design methodology of ball-screw driven servomechanisms with discrete controllers. part I: Modelling and performance analysis," *Mechatronics*, vol. 16, pp. 491–502, 2006.
- [12] H. Van Brussel, P. Sas, I. Nemeth, P. De Fonseca, and P. Den Braembussche, "Towards a mechatronic compiler," *Mechatronics, IEEE/ASME Transactions on*, vol. 6, pp. 90–105, 2001.
- [13] G. Bianchi, F. Paolucci, P. Van den Braembussche, H. Van Brussel, and F. Jovane, "Towards virtual engineering in machine tool design," *CIRP Annals - Manufacturing Technology*, vol. 45, pp. 381–384, 1996.
- [14] E. Schäfers, "Mechatronic modeling and analysis of machine tools," in *Proc. 2nd International Conference on High Performance Cutting (CIRP-HPC'06), Vancouver*, 2006.

- [15] R. Whalley, M. Ebrahimi, and A. Abdul-Ameer, "Machine tool axis dynamics," *Proceedings of the Institution of Mechanical Engineers, Part C: Journal of Mechanical Engineering Science*, vol. 220, pp. 403–419, 2006.
- [16] C. Pislaru, D. Ford, and G. Holroyd, "Hybrid modelling and simulation of a computer numerical control machine tool feed drive," *Proceedings of the Institution of Mechanical Engineers, Part I: Journal of Systems and Control Engineering*, vol. 218, pp. 111–120, 2004.
- [17] K. Varanasi and S. Nayfeh, "The dynamics of lead-screw drives: Low-order modeling and experiments," *TRANSACTIONS-AMERICAN SOCIETY OF MECHANICAL ENGINEERS JOURNAL OF DYNAMIC SYSTEMS MEASUREMENT AND CONTROL*, vol. 126, pp. 388–396, 2004.
- [18] K. Erkorkmaz and A. Kamalzadeh, "High bandwidth control of ball screw drives," *CIRP Annals - Manufacturing Technology*, vol. 55, pp. 393–398, 2006.
- [19] Y. Zhou, F. Peng, and J. Chen, "Torsion vibration analysis of lead-screw feed drives with changeable table position and work-piece mass," in *Proceeding of the International Conference on Mechatronics and Automation, 2007. ICMA 2007*, 2007, pp. 2194–2199.
- [20] A. Kamalzadeh and K. Erkorkmaz, "Compensation of axial vibrations in ball screw drives," *CIRP Annals - Manufacturing Technology*, vol. 56, pp. 373–378, 2007.
- [21] M. Zaeh, T. Oertli, and M. J., "Finite element modelling of ball screw feed drive systems," *CIRP Annals - Manufacturing Technology*, vol. 53, pp. 289–292, 2004.
- [22] C. Okwudire and Y. Altintas, "Hybrid modeling of ball screw drives with coupled axial, torsional, and lateral dynamics," *Journal of Mechanical Design*, vol. 131, pp. 0710021–0710029, 2009.

- [23] V. Moreno-Castaneda, C. Pislaru, J. Freeman, and D. Ford, “Modelling and simulation of a feed drive using the transmission line modelling technique,” in *Laser Metrology and Machine Performance VI*. WIT Press, 2003, pp. 193–202.
- [24] V. Moreno-Castaneda, C. Pislaru, and D. Ford, “Modelling and simulation of the dynamic behaviour of a ball screw system using transmission line modelling technique,” June 2005.
- [25] C. Pislaru, V. Moreno-Castaneda, and D. Ford, “Dynamic model of a non-linear servo control system using transmission line modelling technique,” in *Proceedings of IEE-UKACC International Conf. CONTROL*, 2004, pp. 65–70.
- [26] K. NG, “Modeling and control of feed drives,” Master’s thesis, The University of British Columbia, Canada, 2011.
- [27] L. Ljung, *System Identification: Theory for The User*, 2/E, T. Kailath, Ed. Prentice Hall, 1998.
- [28] Y. Altintas, *Manufacturing Automation - Metal Cutting Mechanics, Machine Tool Vibrations, and CNC Design*, 2nd ed. University of British Columbia: Cambridge University Press, 2012.
- [29] A. Casquero, R. Hecker, D. Vicente, and M. Flores, “Parameter identification of a feed drive for high speed machine tools,” *ABCM Symposium Series in Mechatronics*, vol. 4, pp. 546–552, 2010.
- [30] K. Erkorkmaz, “Optimal trajectory generation and precision tracking control for multi axis machines,” Ph.D. dissertation, The University of British Columbia, Canada, 2004.
- [31] M. Tomizuka, “Zero phase error tracking algorithm for digital control.” *J. DYN. SYST. MEAS. CONTROL.*, vol. 109, pp. 65–68, 1987.

- [32] E. Tung and M. Tomizuka, "Feedforward tracking controller design based on the identification of low frequency dynamics," *Journal of dynamic systems, measurement, and control*, vol. 115, pp. 348–356, 1993.
- [33] J. Yang, D. Zhang, and L. Zexiang, "Modeling and identification for high-speed milling machines," in *Proceeding of the IEEE International Conference on Automation Science and Engineering, 2007.*, 2007, pp. 346–351.
- [34] K. Erkorkmaz and Y. Altintas, "High speed CNC system design. part I: Jerk limited trajectory generation and quintic spline interpolation," *International Journal of Machine Tools and Manufacture*, vol. 41, pp. 1323–1345, 2001.
- [35] Y. Altintas and K. Erkorkmaz, "Feedrate optimization for spline interpolation in high speed machine tools," *CIRP Annals - Manufacturing Technology*, vol. 52, pp. 297–302, 2003.
- [36] N. Singer and W. Seering, "Preshaping command inputs to reduce system vibration," *ASME Journal of Dynamic Systems Measurement and Control*, vol. 112, pp. 76–82, 1988.
- [37] M. Rezaei Khosdarregi, "Vibration avoidance and contour error precompensation in high speed five-axis machine tools using command shaping techniques," Master's thesis, The University of British Columbia, Canada, 2012.
- [38] Y. Altintas and M. Rezaei Khosdarregi, "Contour error control of CNC machine tools with vibration avoidance," *CIRP Annals - Manufacturing Technology*, vol. 61, pp. 335–338, 2012.
- [39] B. Chung, S. Smith, and J. Tlusty, "Active damping of structural modes in high-speed machine tools," *Journal of Vibration and Control*, vol. 3, pp. 279–295, 1997.

- [40] R. Banavar and P. Dominic, "An lqg/h infinity controller for a flexible manipulator," *Control Systems Technology, IEEE Transactions on*, vol. 3, pp. 409–416, 1995.
- [41] W. Symens, H. Van Brussel, and J. Swevers, "Gain-scheduling control of machine tools with varying structural flexibility," *CIRP Annals - Manufacturing Technology*, vol. 53, pp. 321–324, 2004.
- [42] D. Verscheure, B. Paijmans, H. Van Brussel, and J. Swevers, "Vibration and motion control design and trade-off for high-performance mechatronic systems," in *Computer Aided Control System Design, 2006 IEEE International Conference on Control Applications, 2006 IEEE International Symposium on Intelligent Control, 2006 IEEE*, 2006, pp. 1115–1120.
- [43] I. Mahmood, S. Moheimani, and B. Bhikkaji, "Precise tip positioning of a flexible manipulator using resonant control," *Mechatronics, IEEE/ASME Transactions on*, vol. 13, pp. 180–186, 2008.
- [44] A. Dietmair and A. Verl, "Drive based vibration reduction for production machines," *Modern Machinery Science Journal*, vol. 3, pp. 129–133, 2009.
- [45] T. Chen and J. Tlustý, "Effect of low-friction guideways and lead-screw flexibility on dynamics of high-speed machines," *CIRP Annals - Manufacturing Technology*, vol. 44, pp. 353–356, 1995.
- [46] G. Pritschow, C. Eppler, and W. Lehner, "Ferraris sensor - the key for advanced dynamic drives," *CIRP Annals - Manufacturing Technology*, vol. 52, pp. 289–292, 2003.
- [47] Y. Altintas and C. Okwudire, "Dynamic stiffness enhancement of direct-driven machine tools using sliding mode control with disturbance recovery," *CIRP Annals - Manufacturing Technology*, vol. 58, pp. 335–338, 2009.

- [48] M. Hanifzadegan and R. Nagamune, “Switching gain-scheduled control design for flexible ball screw drives,” *In Press*.
- [49] A. Kamalzadeh, D. Gordon, and K. Erkorkmaz, “Robust compensation of elastic deformations in ball screw drives,” *International Journal of Machine Tools and Manufacture*, vol. 50, pp. 559–574, 2010.
- [50] D. Ewins, *Modal Testing: Theory, Practice And Application*. Research studies press Baldock, 2000, vol. 2.
- [51] M. Richardson and D. Formenti, “Parameter estimation from frequency response measurements using rational fraction polynomials,” in *Proceedings of the 1st International Modal Analysis Conference*, vol. 1, 1982, pp. 167–186.
- [52] R. E. D. Bishop and G. M. L. Gladwell, “An investigation into the theory of resonance testing,” *Philosophical Transactions of the Royal Society of London. Series A, Mathematical and Physical Sciences*, vol. 255, no. 1055, pp. 241–280, 1963.
- [53] J. W. Pendered, “Theoretical investigation into the effects of close natural frequencies in resonance testing,” *Journal of Mechanical Engineering Science*, vol. 7, no. 4, pp. 372–379, 1965.
- [54] K. Ege, X. Boutillon, and B. David, “High-resolution modal analysis,” *Journal of Sound and Vibration*, vol. 325, pp. 852–869, 2009.
- [55] W. G. Halvorsen and D. Brown, “Impulse technique for structural frequency response testing,” *Sound and Vibration*, vol. 11, pp. 8–21, 1977.
- [56] V. Lampaert, J. Swevers, and F. Al-Bender, “Impact of nonlinear friction on frequency response function measurements,” in *Proceedings of the International Seminar on Modal Analysis*, vol. 1, KU Leuven, 1998, pp. 443–450.

- [57] M. Law, Y. Altintas, and A. Phani, "Rapid evaluation and optimization of machine tools with position-dependent stability," *International Journal of Machine Tools and Manufacture*, vol. 68, pp. 81–90, 2013.
- [58] Y. Altintas, K. Erkorkmaz, and W. Zhu, "Sliding mode controller design for high speed feed drives," *CIRP Annals - Manufacturing Technology*, vol. 49, pp. 265–270, 2000.
- [59] M. Law, "Position-dependent dynamics and stability of machine tools," Ph.D. dissertation, The University of British Columbia, Canada, 2013.
- [60] G. F. Franklin, J. D. Powell, and M. L. Workman, *Digital Control of Dynamic Systems, Second Edition*. Addison - Wesley, 1990.

Appendix A

ZOH Equivalent of The T.F in Equation

4.6

According to equation (4.6) the state space representation of the transfer function obtained through rigid body modeling in continuous time domain is:

$$\begin{bmatrix} \dot{x}_t(t) \\ \dot{v}_t(t) \end{bmatrix} = \underbrace{\begin{bmatrix} 0 & 1 \\ 0 & Q_v \end{bmatrix}}_{A_c} \begin{bmatrix} x_t(t) \\ v_t(t) \end{bmatrix} + \underbrace{\begin{bmatrix} 0 & 0 \\ P_v & -P_v \end{bmatrix}}_{B_c} \begin{bmatrix} u(t) \\ d(t) \end{bmatrix} \quad (\text{A.1})$$

$$y(t) = \underbrace{\begin{bmatrix} 1 & 0 \end{bmatrix}}_{C_c} \begin{bmatrix} x_t(t) \\ v_t(t) \end{bmatrix} \quad (\text{A.2})$$

As presented in equation (4.7), the zero order hold equivalent of the above state-space representation can be obtained as follows:

$$\begin{bmatrix} x_t(k+1) \\ v_t(k+1) \end{bmatrix} = A_d \begin{bmatrix} x_t(k) \\ v_t(k) \end{bmatrix} + B_d \begin{bmatrix} u(k) \\ d(k) \end{bmatrix}$$

$$\text{where } A_d = e^{A_c T_s}, B_d = \int_0^{T_s} e^{A_c \lambda} d\lambda . B_c \quad (\text{A.3})$$

In the above equation, $A_c T_s = \begin{bmatrix} 0 & T_s \\ 0 & Q_v T_s \end{bmatrix}$. To find $e^{A_c T_s}$, first we need to calculate eigenvalues of $A_c T_s$. Therefore, we need to solve equation below:

$$\det(A_c T_s - \lambda I_{2 \times 2}) = 0 \Rightarrow \det \begin{bmatrix} -\lambda & T_s \\ 0 & Q_v T_s - \lambda \end{bmatrix} = 0 \quad (\text{A.4})$$

$$-\lambda (Q_v T_s - \lambda) = 0 \Rightarrow \lambda_1 = 0, \lambda_2 = Q_v T_s \quad (\text{A.5})$$

The next step is to find the eigenvectors associated with each eigenvalue. Therefore, for $\lambda_1 = 0$ we have:

$$A_c T_s \begin{bmatrix} a_1 \\ b_1 \end{bmatrix} = \lambda_1 \begin{bmatrix} a_1 \\ b_1 \end{bmatrix} = \begin{bmatrix} 0 \\ 0 \end{bmatrix} \Rightarrow \begin{bmatrix} 0 & T_s \\ 0 & Q_v T_s \end{bmatrix} \begin{bmatrix} a_1 \\ b_1 \end{bmatrix} = \begin{bmatrix} 0 \\ 0 \end{bmatrix} \quad (\text{A.6})$$

$$\Rightarrow \begin{cases} b_1 T_s = 0 \\ b_1 Q_v T_s = 0 \end{cases} \Rightarrow b_1 = 0 \quad (\text{A.7})$$

From equation (A.7) we notice that b_1 must be zero and a_1 can have any value. In this case we select $a_1 = 1$. Hence, the eigenvector associated with $\lambda_1 = 0$ is $v_1 = \begin{bmatrix} 1 \\ 0 \end{bmatrix}$. For $\lambda_2 = Q_v T_s$ we have:

$$A_c T_s \begin{bmatrix} a_2 \\ b_2 \end{bmatrix} = \lambda_2 \begin{bmatrix} a_2 \\ b_2 \end{bmatrix} = \begin{bmatrix} Q_v T_s a_2 \\ Q_v T_s b_2 \end{bmatrix} \Rightarrow \begin{bmatrix} 0 & T_s \\ 0 & Q_v T_s \end{bmatrix} \begin{bmatrix} a_2 \\ b_2 \end{bmatrix} = \begin{bmatrix} Q_v T_s a_2 \\ Q_v T_s b_2 \end{bmatrix} \quad (\text{A.8})$$

$$\Rightarrow \begin{cases} b_2 T_s = Q_v T_s a_2 \\ b_2 Q_v T_s = Q_v T_s b_2 \end{cases} \Rightarrow b_2 = Q_v a_2 \quad (\text{A.9})$$

If we choose $a_2 = 1$, the associated eigenvector for $\lambda_2 = Q_v T_s$ will be $v_2 = \begin{bmatrix} 1 \\ Q_v \end{bmatrix}$. Having eigen values and eigenvectors:

$$e^{A_c T_s} = \Psi^{-1} e^{D_{A_c T_s}} \Psi$$

where $\Psi = \begin{bmatrix} v_1 & v_2 \end{bmatrix}$, $D_{A_c T_s} = \begin{bmatrix} \lambda_1 & 0 \\ 0 & \lambda_2 \end{bmatrix}$, $e^{D_{A_c T_s}} = \begin{bmatrix} e^{\lambda_1} & 0 \\ 0 & e^{\lambda_2} \end{bmatrix}$ (A.10)

Following the procedures presented above, we have:

$$A_d = \begin{bmatrix} 1 & -e^{Q_v T_s} \\ 0 & e^{Q_v T_s} \end{bmatrix} \quad (A.11)$$

Having A_d , from equation (A.3), B_d can be obtained as follows:

$$B_d = \int_0^{T_s} e^{A_c \lambda} d\lambda . B_c = \begin{bmatrix} T_s & -\frac{1}{Q_v} (e^{Q_v T_s} - 1) \\ 0 & \frac{1}{Q_v} (e^{Q_v T_s} - 1) \end{bmatrix} \begin{bmatrix} 0 & 0 \\ P_v & -P_v \end{bmatrix}$$

$$\Rightarrow B_d = \begin{bmatrix} -\frac{P_v}{Q_v} (e^{Q_v T_s} - 1) & \frac{P_v}{Q_v} (e^{Q_v T_s} - 1) \\ \frac{P_v}{Q_v} (e^{Q_v T_s} - 1) & -\frac{P_v}{Q_v} (e^{Q_v T_s} - 1) \end{bmatrix} \quad (A.12)$$

Appendix B

Orthogonal Polynomials

B.1 Construction of Orthogonal Polynomials

The simplified Fossythe method presented by Richardson and Formenti [51] to construct the complex orthogonal polynomials ($\phi_{i,k}$ and $\theta_{i,k}$) used in modal parameter estimation through RFP method are summarized in Equations (B.1) to (B.5):

$$\theta_{i,k} = (j)^k R_{i,k} \quad (\text{B.1})$$

$$R_{i,-1} = 0; R_{i,0} = \frac{1}{D_0}; R_{i,k} = \frac{S_{i,k}}{D_k} \quad (\text{B.2})$$

$$S_{i,k} = \omega_i R_{i,k-1} - V_{k-1} R_{i,k-2}; k = 2, 3, \dots; i = -L, \dots, -1, 1, \dots, L \quad (\text{B.3})$$

$$V_0 = 0; V_{k-1} = \sum_{i=1}^L \omega_i R_{i,k-1} R_{i,k-2} q_i \quad (\text{B.4})$$

$$D_0 = \sqrt{\sum_{i=-L}^L q_i}; D_k = \sqrt{\sum_{i=-L}^L (s_{i,k})^2 q_i} \quad (\text{B.5})$$

q_i is the weighting function and equals to h_i for $\theta_{i,k}$. To obtain the orthogonal polynomials associated with the numerator ($\phi_{i,k}$), the weighting function (q_i) must be chosen equal to 1 for all frequencies in Equations (B.2) to (B.5).

B.2 Proof of Equation 4.51

The transfer function used in modal parameter estimation through RFP method which is expressed in terms of orthogonal polynomials in Equation 4.42 has the following characteristic equation:

$$\text{Ch.Eq: } \sum_{k=0}^n d_k \theta_{i,k} \quad (\text{B.6})$$

Replacing $\theta_{i,k}$ by $(j)^k R_{i,k}$ from Equation (B.1) and expanding Equation (B.6) we have:

$$\sum_{k=0}^n d_k \theta_{i,k} = d_0 \underbrace{(j)^0 R_{i,0}}_{P_0(j\omega_i)} + d_1 \underbrace{(j)^1 R_{i,1}}_{P_1(j\omega_i)} + \cdots + d_{n-1} \underbrace{(j)^{n-1} R_{i,n-1}}_{P_{n-1}(j\omega_i)} + d_n \underbrace{(j)^n R_{i,n}}_{P_n(j\omega_i)} \quad (\text{B.7})$$

where $P_n(j\omega)$ is the n^{th} order complex orthogonal polynomial. From Equation (B.7), b_k , which is the coefficient of s^k in ordinary expression of characteristic equation, can be expressed in terms of p_k^i which is the coefficient of s^k in the orthogonal polynomial of i^{th} order when it is considered in its ordinary form (written in terms of s, s^2, s^3, \dots, s^i) as:

$$\begin{aligned} b_n &= d_n p_n^n \\ b_{n-1} &= d_n p_{n-1}^n + d_{n-1} p_{n-1}^{n-1} \\ b_{n-2} &= d_n p_{n-2}^n + d_{n-1} p_{n-2}^{n-1} + d_{n-2} p_{n-2}^{n-2} \\ &\vdots \\ b_1 &= d_n p_1^n + d_{n-1} p_1^{n-1} + \cdots + d_2 p_1^2 + d_1 p_1^1 \\ b_0 &= d_n p_0^n + d_{n-1} p_0^{n-1} + \cdots + d_1 p_0^1 + d_0 p_0^0 \end{aligned} \quad (\text{B.8})$$

$$\implies b_k = \sum_{i=k}^m d_i p_k^i \quad (\text{B.9})$$

Considering Equations (B.7), (B.2), and (B.3), we have:

$$\begin{aligned}
 P_0(j\omega_i) &= (j)^0 R_{i,0} = \frac{1}{D_0} \\
 P_1(j\omega_i) &= (j)^1 R_{i,1} = (j)^1 \left[\frac{\omega_i R_{i,0}}{D_1} \right] = \frac{(j\omega_i)}{D_1} \left[(j)^0 R_{i,0} \right] = \frac{(j\omega_i)}{D_1} [P_0(j\omega_i)] \\
 P_2(j\omega_i) &= (j)^2 R_{i,2} = (j)^2 \left[\frac{\omega_i R_{i,1} - V_1 R_{i,0}}{D_2} \right] = \frac{(j\omega_i)}{D_2} \left[(j)^1 R_{i,1} + V_1 (j)^0 R_{i,0} \right] = \dots \\
 &\dots = \frac{(j\omega_i)}{D_2} [P_1(j\omega_i) + V_1 P_0(j\omega_i)] \\
 P_3(j\omega_i) &= (j)^3 R_{i,3} = (j)^3 \left[\frac{\omega_i R_{i,2} - V_2 R_{i,1}}{D_3} \right] = \frac{(j\omega_i)}{D_3} \left[(j)^2 R_{i,2} + V_2 (j)^1 R_{i,1} \right] = \dots \quad (\text{B.10}) \\
 &\dots = \frac{(j\omega_i)}{D_3} [P_2(j\omega_i) + V_2 P_1(j\omega_i)] \\
 &\vdots \\
 P_n(j\omega_i) &= (j)^n R_{i,n} = (j)^n \left[\frac{\omega_i R_{i,n-1} - V_{n-1} R_{i,n-2}}{D_n} \right] = \dots \\
 &\dots = \frac{(j\omega_i)}{D_n} \left[(j)^{n-1} R_{i,n-1} + V_{n-1} (j)^{n-2} R_{i,n-2} \right] = \frac{(j\omega_i)}{D_n} [P_{n-1}(j\omega_i) + V_{n-1} P_{n-2}(j\omega_i)]
 \end{aligned}$$

Replacing $(j\omega_i)$ with s , the complex orthogonal polynomials $(P_i(j\omega))$ are represented in terms of Laplace variable (s) as:

$$\begin{aligned}
 P_0(s) &= \frac{1}{D_0} \\
 P_i(s) &= \frac{1}{D_i} (sP_{i-1}(s) + V_{i-1}P_{i-2}(s)); i = 1, \dots, n \quad (\text{B.11})
 \end{aligned}$$

From Equation (B.11), the coefficient associated with s^k in the complex orthogonal polynomial of i^{th} order which is represented by p_k^i in Equation (B.9) can be expressed as:

$$p_k^i = \begin{cases} 0 & k < 0 \text{ or } k > i \\ \frac{1}{D_0} & i = k = 0 \\ \frac{1}{D_i} p_{k-1}^{i-1} + V_{i-1} p_k^{i-2} & 0 \leq k \leq i \end{cases} \quad (\text{B.12})$$